ROBUST ALGORITHMS FOR PENETRATION MECHANICS PROBLEMS

FINAL REPORT

R. C. BATRA

February 1998

U.S. ARMY RESEARCH OFFICE

GRANT NO. DAAH04-95-1-0042

VIRGINIA POLYTECHNIC INSTITUTE AND STATE UNIVERSITY
BLACKSBURG, VA 24061

APPROVED FOR PUBLIC RELEASE;
DISTRIBUTION UNLIMITED.

THE VIEWS, OPINIONS, AND/OR FINDINGS CONTAINED IN THIS REPORT ARE THOSE OF THE AUTHOR(S) AND SHOULD NOT BE CONSTRUED AS AN OFFICIAL DEPARTMENT OF THE ARMY POSITION, POLICY, OR DECISION, UNLESS SO DESIGNATED BY OTHER DOCUMENTATION.

DTIC QUALITY INSPECTED 2

19980520 055

SF 298 MASTER COPY KEEP THIS COPY FOR REPRODUCTION PURPOSES

REPORT DOCUMENTATION PAGE

Form Approved OMB NO. 0704-0188

Public reporting burden for this collection of information is estimated to average 1 hour per response, including the time for reviewing instructions, searching existing data sources, gathering and maintaining the data needed, and completing and reviewing the collection of information. Send comment regarding this burden estimates or any other aspect of this collection of information, including suggestions for reducing this burden, to Washington Headquarters Services, Directorate for information Operations and Reports, 1215 Jefferson Davis Highway, Suite 1204, Arlington, VA 22202-4302, and to the Office of Management and Budget, Paperwork Reduction Project (0704-0188), Washington, DC 20503.

1. AGENCY USE ONLY *(Leave blank)*	2. REPORT DATE	3. REPORT TYPE AND DATES COVERED
	February 1998	Final 12/94-12/97

4. TITLE AND SUBTITLE
Robust Algorithms for Penetration Mechanics Problems

5. FUNDING NUMBERS
DAAH04-95-1-0042

6. AUTHOR(S)
Romesh C. Batra

7. PERFORMING ORGANIZATION NAMES(S) AND ADDRESS(ES)
Department of Engineering Science & Mechanics
MC 0219
Virginia Polytechnic Institute and State University
Blacksburg, VA 24061

8. PERFORMING ORGANIZATION REPORT NUMBER

9. SPONSORING / MONITORING AGENCY NAME(S) AND ADDRESS(ES)
U.S. Army Research Office
P.O. Box 12211
Research Triangle Park, NC 27709-2211

10. SPONSORING / MONITORING AGENCY REPORT NUMBER
ARO 33866.19-EG

11. SUPPLEMENTARY NOTES
The views, opinions and/or findings contained in this report are those of the author(s) and should not be construed as an official Department of the Army position, policy or decision, unless so designated by other documentation.

12a. DISTRIBUTION / AVAILABILITY STATEMENT
Approved for public release; distribution unlimited.

12 b. DISTRIBUTION CODE

13. ABSTRACT *(Maximum 200 words)*

We have investigated the differences in the performance of identical depleted uranium (DU) and tungsten heavy alloy (WHA) rods when deformed in pure torsion, plane strain compression, and during impact at normal incidence onto a smooth rigid block or a deformable steel target. The thermomechanical response of the material has been modeled by the Johnson-Cook relation that accounts for strain and strain-rate hardening of the material and its thermal softening. The effect of modeling the thermal softening by a power law rather than the affine function has also been delineated. It is found that shear bands form at a lower value of the nominal strain in the WHA rod as compared to that in the DU rod during torsion, plane strain compression and the Taylor impact test. However, in the penetration test, a propensity of shear bands form in the DU penetrator in the region abutting the target/penetrator interface and also in the ejecta where the penetrator particles turn to flow backwards. Fewer shear bands form in the WHA rod and they are smeared out resulting in a uniformly deformed zone of intense plastic deformation.

Numerical simulation of a ceramic rod impacting a WHA plate showed that at high speeds a ceramic rod will perforate a WHA plate.

14. SUBJECT TERMS
Uranium and tungsten penetrators, shear bands, thermoviscoplasticity, ceramic penetrators.

15. NUMBER IF PAGES
77

16. PRICE CODE

17. SECURITY CLASSIFICATION OR REPORT	18. SECURITY CLASSIFICATION OF THIS PAGE	19. SECURITY CLASSIFICATION OF ABSTRACT	20. LIMITATION OF ABSTRACT
UNCLASSIFIED	UNCLASSIFIED	UNCLASSIFIED	UL

TABLE OF CONTENTS

1. STATEMENT OF THE PROBLEM STUDIED 1
2. SUMMARY OF PRINCIPAL RESEARCH FINDINGS 4
3. BIBLIOGRAPHY 10
4. PUBLICATIONS 24
5. SCIENTIFIC PERSONNEL SUPPORTED 27
6. DEGREES AWARDED 27
7. HONORS & AWARDS 27
8. APPENDIX 28

STATEMENT OF THE PROBLEM

The fundamental problem in penetration mechanics may be stated as (Wright and Frank[1]): Given a projectile, a target, and details of their initial geometry, kinematics, and materials; determine whether or not the target will be perforated upon impact. If perforated, find the residual characteristics of the projectile and the target, and if not, ascertain the shape and depth of the hole. Of the three approaches, namely, simple data correlation, engineering models, and numerical simulation used to analyze a penetration problem, we have concentrated on the third approach and developed robust and efficient algorithms capable of analyzing details of thermomechanical deformations of the penetrator and the target.

Factors that play a significant role during the penetration of metal targets by projectiles include material properties, impact velocity, projectile shape, target support position, and relative dimensions of the target and the projectile. Recently, emphasis has been placed on kinetic energy penetrators, which for terminal ballistic purposes may be considered as long metal rods traveling at high speeds. For impact velocities in the range of 2 to 10 km/sec, compressible hydrodynamic flow equations can be used to describe adequately the impact and penetration phenomena, because large stresses occurring in hypervelocity impact permit one to neglect the rigidity and compressibility of the striking bodies. Models, which require the use of the Bernoulli equation or its modification to describe this hypervelocity impact, have been proposed by Birkhoff *et al.*[2] and Pack and Evans.[3] At ordnance velocities (0.5 to 2 km/sec), material strength becomes an important parameter. Allen and Rogers[4] modified the Pack and Evans[3] flow model by representing the strength as a resistive pressure. This idea was taken further by Alekseevskii[5] and Tate,[6,7] who considered separate resistive pressures for the penetrator and the target. These resistive pressures are empirically determined quantities, and the predicted results depend strongly upon the assumed values of these pressures. As described lucidly by Wright[8] in his survey article on long rod penetrators, Tate's model is difficult to use for quantitative purposes, because the strength parameters depend upon the velocity of impact and the particular combination of materials involved.

The one-dimensional theories ignore the lateral motion, plastic flow, and the detailed dynamic effects. The paper by Backman and Goldsmith[9] is an authoritative review of the open literature on ballistic penetration, containing 278 reference citations from the 1800's to 1977. They describe different physical mechanisms involved in the penetration and perforation processes, and also discuss a number of engineering models. Jonas and Zukas[10] reviewed various analytical methods for the study of kinetic energy projectile-armor interaction at ordnance velocities and placed particular emphasis on three-dimensional numerical simulation of perforation. Anderson and Bodner[11] have recently reviewed engineering models for penetration and some of the major advances in hydrocode modeling of penetration problems. Three books,[12-14] published during the past few years, include extensive discussions of the engineering models, experimental techniques, and analytical modeling of ballistic perforation.

Manganello and Abbot,[15] Wingrove and Wulf,[16] and Recht[17] observed that the penetration resistance of some armor materials is reduced, even though these materials exhibit increased static mechanical strength. During penetration of such targets the formation of adiabatic shear bands leads to a sharp drop in shear yield stress after the formation of a plug,

and the penetration resistance of the target is severely reduced. It has been suggested[23,24] that the material in the shear band melts. Woodward[20] has proposed a model for adiabatic shear plugging failure of targets. He considered the penetration of ductile metal targets impinged upon by a sharp conical projectile and assumed that the penetration is achieved by radial expansion of a hole in the plate from zero to the penetrator radius. Wingrove's[21] experiments show that sharp corners of flat-ended projectiles cause deformation in a narrow zone of the target, and hemispherical and ogive nose shapes progressively broaden the deformation pattern. Because of the formation of the thermal-softened shear zone and the difference in fracture behavior for breakout, flat-ended projectiles penetrate materials susceptible to adiabatic shear with greater ease than do radiused projectiles.

Awerbuch,[22] Awerbuch and Bodner,[23] Ravid and Bodner,[24] and Ravid, Bodner and Holcman[25] have developed models with which to analyze the normal perforation of metallic plates by projectiles. The penetration process is presumed to occur in several interconnected stages, with plug formation and ejection being the principal mechanism of plate perforation. They presumed a kinematically admissible flow field and found the unknown parameters by minimizing the plastic dissipation. They characterized the procedure as being "a modification of the upper bound theorem of plasticity to include dynamic effects". Even if such a theorem were valid, it is hard to tell how close such a bound might be to the solution of the problem. These authors have included the dependence of the yield stress upon the strain rate and studied a purely mechanical problem.

Recht[26] has adapted the Taylor[27] model of mushrooming to the situation in which the penetrator is allowed to move into the target, and both erosion and shear mass loss are allowed in the penetrator. The principal difficulty is the specification of velocities for the plastic waves in the projectile and the target in order to obtain a unique solution for the rate of interface movement. Brooks[28] and Brooks and Erickson[29] have demonstrated transitions in behavior such that, at increased velocities, it is possible to observe a reduced depth of penetration over a range of velocities. The transition is related to the degree of radial constraint offered by the surrounding target material and its ability to restrict projectile deformation. The transition velocity depends strongly upon the projectile tip geometry. Above the transition velocity, the deformation is described as "jetting" to illustrate a similarity in behavior to shaped charge jets. Forestall *et al.*[30] have used the cavity expansion model to predict the penetration depths for relatively rigid projectiles striking deformable semi-infinite targets.

Whereas most of the engineering models described above have considered one-dimensional deformations of the rod and target, the numerical studies have analyzed two- or three-dimensional deformations. Harlow and Pracht[31] used the particle-in-cell scheme to analyze the high-velocity (15 km/sec), shaped-charge, jet penetration in which they ignored the effect of material strength. More recently, finite difference codes have been developed that model elastic and plastic effects. Published results of long rod impact include those of Sedgwick *et al.*,[32] who used the HELP code, Wilkins,[33] who used the HEMP code, and Pidsley,[4] who employed the HELP code. These codes solve the equations of continuum mechanics formulated in either Lagrangian (HEMP) or Eulerian (HELP) coordinates. In the HEMP code, the finite difference operators are centered in space and time to give second order accuracy. The von Mises yield criterion and the incremental theory of plasticity are used to derive the incremental stress-strain relations. The material model employed in the HELP code includes the Tillotson equation of state modified to give a smooth transition between

condensed and expanded states, the von Mises yield criterion with yield strength taken to increase with hydrostatic pressure and decrease linearly with the increase in the temperature, and a failure criterion based upon either a minimum value of the mass density or a critical value of the principal stress in tension.

Batra and Chen[35] recently developed a simple technique with which to analyze approximately the axisymmetric steady state deformations of a rigid/viscoplastic target being penetrated by a long rigid cylindrical rod with a hemispherical nose. They assume a kinematically admissible velocity field that satisfies the balance of mass, all of the essential boundary conditions, and traction boundary conditions on the axis of symmetry and on the target/penetrator interface, and they evaluate various parameters in the presumed velocity field by minimizing the error in the satisfaction of the balance of linear momentum. The computed results reveal that the leading term in the proposed velocity field gives a good solution that is reasonably close to the previously computed finite element solution of the problem. Batra and Gobinath[36] analyzed the steady state axisymmetric penetration problem for a deformable penetrator and target, and modeled the material for each as thermally softening, but strain and strain-rate hardening. They found that the bottom part of the target/penetrator interface is ellipsoidal rather than hemispherical. The peak pressures in the penetrator near the stagnation point approach $4.58\sigma_{op}$ and that in the target $14\sigma_{ot}$ when $\sigma_{op}/\sigma_{ot} = 3.06$. Here σ_{op} and σ_{ot} equal, respectively, the yield stress in a quasistatic simple compression test for the penetrator and target materials. The axial resisting force on the penetrator equaled 8.91 F, 11.52 F, and 14.51 F ($F = \pi r_o^2 \sigma_{op}$) for stagnation point speeds of 450 m/s, 500 m/s, and 550 m/s, respectively. A significant contribution to the resisting force is made by the consideration of strain-rate hardening effects. When the penetrator and target materials are modeled as rigid/perfectly plastic, Gobinath and Batra[37] found that the resistive pressure terms in the modified Bernoulli's equation depend upon the ratio of the mass densities of the target and the penetrator as well as on the penetration speed.

The analysis of the steady state axisymmetric deformations of an elastic/perfectly plastic target being penetrated by a fast moving rigid cylindrical rod by Jayachandran and Batra[38] has revealed that the consideration of elastic effects reduces the value of the peak hydrostatic pressure acting at the stagnation point, the axial resisting force experienced by the penetrator, and the target resistance parameter appearing in the modified Bernoulli equation nearly 28%, 25%, and 25% , respectively. Batra and Jayachandran[39] modeled the thermoviscoplastic response of the target material by flow rules due to Litonski-Batra, Bodner-Partom,[40] and Brown, Kim, and Anand.[41] They calibrated the three flow rules against a hypothetical plane strain compression test performed at a nominal strain-rate of 3,300 sec^{-1} and then studied the axisymmetric penetration problem. They found that the three constitutive relations gave nearly the same value of the resisting force acting on the penetrator, temperature rise of material particles in the vicinity of the target/penetrator interface, and other macroscopic measures of deformation, such as the effective stress and logarithmic strain-rate. Batra and Adam[42] obtained quite different results with the Litonski-Batra and Bodner-Partom flow rules when they calibrated them against a simple shear test. They[43] also showed that the transverse isotropy of the target material affected significantly its deformations and the resisting force it exerts on the penetrator.

Because of the possibility of several penetration mechanisms, experimental observations usually precede and guide engineering models. However, penetration mechanics experiments

are expensive and require rather sophisticated set-up and instruments to capture finer details of the deformation fields. Our ultimate goal is to incorporate the current state-of-the-art understanding of the material behavior under high hydrostatic pressures, strain and strain-rates, elevated homologous temperatures, plastic spin, and material failure under dynamic loading in the numerical apparatus already built up using an adaptive mesh refinement technique to resolve finer details of deformation fields, and model crack initiation and propagation.

Recent penetration tests of Magness and Farrand[44] involving identical depleted uranium (DU) and tungsten heavy alloy (WHA) rods impacting steel targets at normal incidence have revealed the following. Depleted uranium rods penetrate deeper than WHA rods, the tunnel diameter is smaller for a DU rod than that for a WHA rod and the tunnel surface is rough for DU penetrators but smooth for WHA penetrators. They explained these differences by postualting that shear bands develop continuously in the DU rod causing fractures and hence sharper nose shapes. The major focus of this work, contrary to what the title suggests, has been to understand the differences in the susceptibilitiy to adiabatic shear banding between DU and WHA.

SUMMARY OF PRINCIPAL RESEARCH FINDINGS

In an attempt to understand the differences between the initiation and development of adiabatic shear bands in depleted uranium (DU) and tungsten heavy alloys (WHA), we numerically simulated their behavior in simple torsion, plane strain compression, Taylor impact test, and the normal penetration of identical DU and WHA rods into steel targets. A principal result for each of these simulations is given below.

Batra et al.[45] investigated the initiation of adiabatic shear bands in thin-walled tubes deformed in torsion. They used the Johnson-Cook relation to model the thermoviscoplastic response of the material, values of material parameters included in Rajendran's report,[46] and the finite element code DYNA3D[47] to analyse the transient thermomechanical deformations. The initial thickness of the tube was taken to vary in the axial direction so that it was thinnest at the center and thickest at the edges. Figures 1a and 1b exhibit the time history of the torque required to deform the tube and of the effective plastic strain at the center of the tube. Note that the nondimensional time equals the nominal shear strain. It is clear from these results that the value of the average strain at which a shear band initiates in WHA is lower than that in the DU.

Batra and Peng[48] have scrutinized the development of adiabatic shear bands in plane strain compression of identical DU and WHA blocks with the thermomechanical response of each material modeled by the Johnson-Cook relation. The rectangular cross-section with height to width ratio of 2 was assumed to have upto 300 randomly distributed weak elements for which the flow stress was taken to be 5% lower than that for the rest of the body. Four different random distributions of weak elements were considered. In each case more than one shear band formed, and the average strain at which a band initiated, as signified by the drop in the load required to deform the block varied a little. However, the load required to deform the block prior to the initiation of the shear band was found to be independent of

the distribution of weak elements. The load dropped more rapidly for the uranium block as compared to that for the tungsten block. Also, the average strain at which a shear band initiated in tungsten was lower than that in uranium. This should be obvious from Fig. 2 which exhibits the deformed meshes for the two materials. The dominant shear band, defined as the one with the maximum value of the effective plastic strain, is inclined at 42.5° counterclockwise from the horizontal axis for uranium and 135° for tungsten. However, when either the shear modulus for the tungsten block was artificially changed to that for the uranium block, or the defects in both were modeled as 95% weak elements (essentially voids), the angle of inclination of the dominant shear band in each material was found to be approximately 42.5° counterclockwise from the horizontal axis. The size of the dead zone, defined as the material region whose particles are essentially at rest, was found to be larger for the tungsten block than that for the uranium block.

Batra and Stevens[49] analysed the Taylor impact test for the DU and WHA rods. They first modeled the thermomechanical response of each material by the Johnson-Cook relation, and then changed only the thermal softening function to that proposed by Zhou et al.[50] We note that the shear modulus for WHA equals 2.76 times that for DU. Since their mass densities are the same, the speed of the shear wave in WHA will equal 1.66 times that in DU. Figure 3 depicts the effective stress vs. the effective plastic strain curves for axisymmetric compression of a homogeneous cylinder deformed at a nominal strain-rate of 5,000/s. We have also included these curves for the Zhou et al. thermal softening function with $\beta = 2.4$ and $\alpha = 0.2$ and 0.3. It is clear that for both DU and WHA, the Zhou et al. expression exhibits enhanced softening of the material. That is, for same values of the effective plastic strain and the effective plastic strain-rate, the flow stress is lower with the Zhou et al. softening than that with the Johnson-Cook relation.

The finite element mesh had 40 uniform elements in the radial direction and 250 elements in the axial direction as described below. The rod length was divided into three segments: $0 \leq z \leq 10$ mm, $10 \leq z \leq 25$ mm, and $25 \leq z \leq 60$ mm. The first portion was divided into 80 uniform elements and the second and third segments were each divided into 85 nonuniform elements whose height increased as one moved away from the impact face. The mesh is fine near the impact surface and should sufficiently capture the intense deformations of the rod in the mushroomed region. Computed results for a trial problem indicated that the height of the mushroomed region was approximately 5mm. The contact condition is satisfied by nullifying the axial velocity of nodes about to penetrate the target.

The contours of the effective plastic strain exhibited in Fig. 4 for the DU and WHA rods at $t = 10$ and 50 μs suggest that rod particles outside of the mushroomed region do not undergo much plastic deformation. At $t = 10$ μs the maximum effective plastic strain equals 0.41 and 0.49 in the DU and WHA rods and occurs at a point near the periphery of the impact face in DU but near the centroidal axis in WHA. This point where the maximumn effective plastic strain occurs gradually moves towards the stagnation point. At $t = 50$ μs, the maximum effective plastic strain equals 1.4 in DU and 2.2 in WHA and, in each rod, occurs at a point of the impact face that is close to the centroidal axis. The severely deformed region with the effective plastic strain exceeding 1.0 extends, on the impact face to nearly 6.8 mm for the WHA rod and 5.00 mm for the DU rod; its thickness equals approximately 0.8 mm for both materials.

In Fig. 5 we have plotted the time history of the effective plastic strain at several points on the impact face of the DU rod; similar results were obtained for the WHA rod and also for points on the centroidal axial line and the mantle of each rod. It is evident that the effective plastic strain increases monotonically at these points and the material at points close to the centroidal axial line is intensely deformed. The plots of the effective stress vs. effective plastic strain at these points, not included herein, reveal that the effective stress drops essentially monotonically and gradually except when the gap occurs between the impact face and the anvil. At a point near the center of the DU rod, it drops from 1.2 GPa at $t = 10$ μs to 0.45 GPa at $t = 60$ μs and its rate of drop slowly decreases. At numerous points on the impact face, centroidal axial line and the mantle of the rods where we plotted the time histories of the effective plastic strain and the effective stress, we saw neither a catastrophic drop in the effective stress nor a dramatic rise in the rate of growth of the effective plastic strain; these two phenomena were observed at the initiation of a shear band in a thermoviscoplastic body deformed either in simple shear or plane strain compression. This could be due to the different state of stress at a point in the axisymmetric Taylor impact test from that in either simple shear or plane strain compression. Also, the constraint of axisymmetric deformations forces the points to move only in the radial and axial directions. Batra and Kim[51] and Deltort[52] have postulated that a shear band initiates at a point when the effective stress there drops to 90% and 80%, respectively, of its peak value. According to this definition, a shear band has initiated in both the DU and WHA rods at a point close to $r = 0$, $z = 0$, and also at several other points. At $t = 80$ μs, the temperature at the point $r = z = 0$ equals 1250 K for both DU and WHA rods.

Keeping values of the material and geometric parameters unchanged, we computed results for the DU and WHA rods with $\beta = 2.4$, $\alpha = 0.2$ and 0.3. Zhou et al.[50] found that $\alpha = 0.2$ and $\beta = 2.4$ provided a good fit to the test data for the WHA they used. Here we have considered the same values of α for DU because of the lack of data. Thus the differences, if any, in their deformation patterns will be due to the variation in the values of the shear modulus, bulk modulus, and parameters A, B, C and n in the Johnson-Cook relation. The higher value of α is considered to delineate the effects of enhanced thermal softening.

Figures 6a, 6b and 6c depict the shapes of the mushroomed region for the DU and WHA rods for the three softening functions (Johnson-Cook, Zhou et al. with $\alpha = 0.2$ and 0.3). As expected, the softening function strongly influences the shape of the mushroomed region. In each case, the outer radius of the deformed impacted face is greater in the WHA rod than that in the DU rod. For the Johnson-Cook thermal softening, the inflection point in the shape of the mantle is closer to the impacted end for the DU rod as compared to that for the WHA rod. For $\alpha = 0.3$ in the Zhou et al. thermal softening, the curve describing the mantle has a cusp for each material signifying severe deformations there. The height of the mushroomed region is smaller for $\alpha = 0.3$ and it forms sooner in each rod than that for $\alpha = 0.2$. The shapes of the mushroomed regions suggest that severe deformations and hence a shear band may initiate at one or more of the following three locations: adjacent to the stagnation point, near the periphery of the impacted end, and close to the inflection point in the curve describing the mantle of the deformed rod; points selected in these areas for further study of deformations are marked in Figs. 6a-c as P, Q and R respectively. For comparison purposes, we have also investigated histories of various deformation measures at a point close to the centroidal axis and about 2.5 mm above the impact face; this point is

referred to as S. Time histories of the effective plastic strain and the effective stress at these four points for the two rods are plotted in Figs. 7 through 10. Results for the Johnson-Cook model are shown for comparison purposes. It is clear that for both DU and WHA rods and the three thermal softening functions considered, the effective plastic strain at point S is much lower than that at the other three points. We recall that during plane strain compression and simple shearing deformations of a thermoviscoplastic block, the initiation of a shear band is indicated by a rapid growth of the effective plastic strain accompanied by a sharp drop in the effective stress. For the DU and WHA rods, these two conditions are fulfilled at points P and R for $\alpha = 0.3$, thus shear bands initiate there and propagate into the mushroomed head of the rod. For $\alpha = 0.2$ and 0.3 the effective plastic strain at each one of the four points considered grows less rapidly in the DU rod than that in the WHA rod. For $\alpha = 0.2$, the aforestated conditions for the initiation of a shear band are satisfied at point R for the WHA rod and the distortions in the deformed mesh confirm a shear band there. However, for the DU rod, even though the effective plastic strain at point R grows rapidly first, its rate of growth tapers off. The deformed meshes suggest that no shear band initiates from point R in the DU rod with $\alpha = 0.2$ since the mesh is regular in the neighborhood of R. For each thermal softening considered, the mesh around point P is severely deformed. Also, the effective stress there drops to less than 80% of its peak value. Thus, according to the definition of the drop in the effective stress, a shear band initiates at point P for each thermal softening studied. We have plotted, for $\alpha = 0.2$ and 0.3, contours of the effective plastic strain in Fig. 11 for the two rods. It is clear that for both values of α a shear band has developed near the cusp in the mantle for the WHA rod but only for $\alpha = 0.3$ in the DU rod. We recall that Dick et al.[53]observed a shear band passing through the transition region in their reverse ballistic tests on the WHA rod, and a sharp cusp developed where the band intersected the mantle. The mesh used herein is not fine enough to capture the dimensions of this cusp or of the band.

Stevens and Batra[54] further analysed the development of shear bands in a WHA rod impacting at normal incidence a smooth rigid target. The rod's material was modeled either as a mixture of Fe-Ni-W particles interspread randomly among the W-particles or as a homogeneous alloy. It was found that shear bands formed near the transition between the mushroomed region and the relatively undeformed portion of the rod when its material was either a mixture of Fe-Ni-W and W particles or a homogeneous alloy but no such bands formed in either pure W or Fe-Ni-W rods. They attributed these differences to the different initial softening rates of the materials.

Batra and Stevens[49] have analysed the normal impact of 7.69-mm diameter and 76.9-mm long DU and WHA rods moving at 843 m/s on a 60-mm diameter and 70-mm deep steel target. Each material was modeled by the Johnson-Cook relation. The penetrator region was divided into uniform 0.16 mm $\times$ 0.171 mm elements near the impact face with properly graded larger elements away from it. The mesh in the target region was also graded with 0.16 mm $\times$ 0.171 mm elements in the region adjoining the impact face and larger elements elsewhere; Fig. 21 of Stevens's thesis[55] depicts the finite element discretization of the region adjoining the target/penetrator interface. We used the automatic contact option for the first 18.5 μs for DU and 15 μs for WHA penetrator. Subsequently, the noninterpenetration conditions were satisfied by using the slideline type 4 (kinetic with sliding, separation and friction).

Figures 12 and 13 depict at $t = 10$ and 25 μs fringes of the effective plastic strain in the deformed region adjoining the target/penetrator interface. Similar plots and a movie (available at the URL www.sv.vt.edu/research/batra-stevens/pent.html) showing the distribution of the effective plastic strain in the deformed regions indicate that a propensity of narrow regions of intense plastic deformation form in the DU penetrator in the region abutting the target/penetrator interface and also in the ejecta where the penetrator particles turn to flow backwards. Fewer of these narrow regions occur in the WHA rod and they are smeared out resulting in a rather uniformly deformed zone of intense plastic deformation. Also, the ejecta consists of intensely deformed material, separated by shear banded material for the DU rod but continuously deformed material for the WHA rod. The deformed meshes indicated the occurrence of narrow severely deformed regions in the DU penetrator passing through the points where the flow reverses but none in the WHA penetrator. The deforming region was remeshed at $t = 14$ μs and subsequently at every instant when the time step required to integrate the governing equations decreased to one-hundredth of the starting value, or when the mesh distorted so severely as to cause kinks in the boundary. Every attempt was made to remesh identically the deforming penetrator and target regions in the two cases. Figure 25 of Stevens's thesis[55] shows the remeshed region at $t = 20$ μs for the DU penetrator and the steel target. The fluid-like material at the head of the ejecta had to be removed in order for the computations to continue at a reasonable pace; such deletions were kept to a minimum and no fluid-like material was removed till $t = 15$ μs. Values of velocities, mass density, temperature and other variables at the newly created nodes were computed from the previous solution so that the total linear momentum and energy were conserved. Such mappings smoothen out the fields and may retard the growth of shear bands.

Figure 14 illustrates the deformed mesh at $t = 22.5$ μs for the DU penetrator in the region where the flow is turning around, and the distribution of the effective plastic strain on line AB shown in the Figure. It is clear that three shear bands have formed on this line. The deformed mesh for the WHA penetrator at $t = 22.5$ μs is illustrated in Fig. 15; it does not exhibit any narrow intensely deformed regions. For each penetrator, the effective stress within a thin layer adjoining the target/penetrator interface is reduced to almost zero at $t = 30$ μs indicating that the material has essentially lost its strength and behaves like an ideal compressible fluid. The time step has now become too small to continue the computations at a desirable pace.

The time histories of the axial velocity of the tail end of the two penetrators and also of the axial point on the penetrator/target interface were very close to each other (cf. Fig. 28 of [55]). This suggests that differences in the occurrence of shear bands in the ejectas of the two penetrators can not be discerned by examining either the penetration speed or the speed of the tail end of the rod.

Batra and Wilson[56] analysed plane strain deformations of a Tungsten heavy alloy and investigated the effect of the volume of Iron-Nickel-Tungsten (Fe-Ni-W) particles dispersed randomly among the tungsten particles and considered cases when the former equaled 10, 8, 6, 4, 2, 0.2, 0.1, 0.02 and 0.01% of the total volume. For each one of the first five cases, seven different random distributions of Fe-Ni-W particles were analysed with the objectives of finding statistically the average strain at the initiation of a shear band and the standard deviation in this value. The computed results revealed that the initial distribution of Fe-Ni-W particles, provided it exceeded 0.1% had a negligible effect on the time-history of the

compressive load required to deform the body till the time a shear band initiated and also on the instant when a shear band initiated. For the problem studied, it was not easy to decipher when a shear band initiated since it was difficult to formulate an objective criterion. The load required to deform the body dropped noticeably much after (about 2 or 3 microseconds out of a total of 30 microseconds) the mesh had severely deformed; the mesh began to deform intensely before that time. However, the number of bands, their locations and the general pattern of the deformed mesh depended upon the volume percentage and the distribution of Fe-Ni-W particles. Shear bands also formed in pure tungsten and the load history in this case was quite different from that when there were Fe-Ni-W particles distributed randomly in tungsten particles. After one or more shear bands had developed in the block, dead zones with essentially zero strain rates and separated by these bands developed.

Nechitailo and Batra[57] studied the axisymmetric penetration of the ceramic rod into aluminum, steel and tungsten plates. The ceramic was modeled as an elastic-plastic material with different properties in compression and tension, and a material point was assumed to fail when the hydrostatic pressure there was tensile and exceeded the spall strength of the material. The plate material was modeled as an isotropic elastic/plastic with linear strain hardening and a material point was assumed to fail when the effective plastic strain there attained a critical value. Failed elements were deleted from further analysis.

Plates made of aluminum, steel and tungsten were found to be perforated by the ceramic rod; (e.g. see Fig. 16). However, deformations of the ceramic penetrator and the shape of the hole formed depended strongly upon the impact speed. For aluminum plates, the hole was found to be smooth cylindrical for small values of the failure strain and rough hemispherical for large values of the failure strain. For the steel and tungsten plates, the nose shape was initially deformed from flat to conical, and the conical part failed giving rise to a smaller flat-nosed rod. Subsequently, the rod material near its axis of symmetry and the front end failed resulting in a cutter edge. Multiple impacts between the rod and the crater formed in the plate eventually perforated the plate. The residual length of the rod after perforation was found to be more at higher impact speeds.

BIBLIOGRAPHY

1. T. W. Wright and K. Frank, Approaches to Penetration Mechanics, in Impact: Effects of Fast Transient Loading (W. J. Ammann, W. K. Liu, J. A. Studer, and T. Zimmerman, Eds.), A. A. Balkema, Rotterdam, 1988.
2. G. Birkhoff, D. P. McDougall, E. M. Pugh, and G. Taylor, *Proc. Phys. Soc. Lond.*, **57** 147 (1945).
3. D. C. Pack and W. M. Evans, *Proc. Phys. Soc. Lond.* **B64** 298 (1951).
4. W. A. Allen and J. W. Rogers, *J. Franklin Ins.*, **272** 275 (1961).
5. V. P. Alekseevskii, *Combst. Explo. Shock Waves*, **2** 63 (1966).
6. A. Tate, *J. Mech. Phys. Sol.*, **15** 387 (1967).
7. A. Tate, *J. Mech. Phys. Sol.*, **17** 141 (1969).
8. T. W. Wright, A Survey of Penetration Mechanics for Long Rods, in Lecture Notes in Engineering, v. 3, Computational Aspects of Penetration Mechanics, J. Chandra and J. Flaherty, eds., Springer-Verlag, New York, 1984.
9. M. E. Backman and W. Goldsmith, *Int. J. Eng. Sci.*, **16** 1 (1978).
10. G. H. Jonas and J. A. Zukas, *Int. J. Eng. Sci.*, **16** 879 (1978).
11. C. E. Anderson and S. R. Bodner, The Status of Ballistic Impact Modeling, Proc. 3rd TACOM Armor Coordinating Conf., Feb. 17-19, 1987, Monterey, CA.
12. J. A. Zukas (ed.), High Velocity Impact Dynamics, John Wiley & Sons, Inc., New York, 1990.
13. E. W. Billington and A. Tate, The Physics of Deformation and Flow, McGraw-Hill, New York (1981).
14. J. A. Zukas, T. Nicholas, H. F. Swift, L. B. Greszczuk, and D. R. Curran, Impact Dynamics, John Wiley, New York (1982).
15. S. J. Manganello and K. H. Abbott, *J. Mats.*, **7** 231 (1972).
16. A. L. Wingrove and G. L. Wulf, *J. Aust. Inst. Met.*, **18** 167 (1973).
17. R. F. Recht, I. Mech. E., 3rd Int. Conf. on High Pressure, Scotland (May 1970).
18. T. A. C. Stock and K. R. L. Thompson, *Met. Trans.*, **1** 219 (1970).
19. A. J. Bedford, A. L. Wingrove, and K. R. L. Thompson, *J. Aust. Inst. Met.*, **19** 61 (1974).
20. R. L. Woodward, *Int. J. Mech. Sci.*, **20** 599 (1978).
21. A. L. Wingrove, *Met. Trans.*, **4** 1829 (1973).
22. J. Awerbuch, Technion-Israel Institute of Technology, MED Report No. 28 (1970).

23. J. Awerbuch and S. R. Bodner, *Int. J. Solids Structures*, **10** 671 (1974).

24. M. Ravid and S. R. Bodner, *Int. J. Eng. Sci.*, **21** 577 (1983).

25. M. Ravid, S. R. Bodner, and I. Holcman, *Int. J. Eng. Sci.*, **25** 473 (1987).

26. R. F. Recht, *Int. J. Eng. Sci.*, **16** 809 (1978).

27. G. I. Taylor, *Proc. R. Soc.*, **A194** 289 (1948).

28. P. N. Brooks, Defense Research Establishment, Valcartier, Canada, Rept. DREV R-4001/74 (Oct. 1974).

29. P. N. Brooks and W. N. Erickson, Defense Research Establishment, Valcartier Canada, Rept. DREV R-643/72 (Nov. 1971).

30. M. J. Forrestal, K. Okajima, and V. K. Luk, Penetration of 6061-T651 Aluminum Targets with Rigid Long Rods, Proc. 1st Joint SES/ASME-AMD Conf., Univ. of California at Berkeley, June 1988.

31. F. H. Harlow and W. E. Pracht, *Physics Fluids*, **9** 1951 (1966).

32. R. T. Sedgwick, L. J. Hageman, R. G. Herrmann, and J. L. Waddell, *Int. J. Eng. Sci.*, **16** 859 (1978).

33. M. L. Wilkins, *Int. J. Eng. Sci.*, **16** 793 (1978).

34. P. H. Pidsley, *J. Mech. Phys. Sol.*, **32** 315 (1984).

35. R. C. Batra and X. Chen, *Int. J. Engng. Sci.*, **28** 1347 (1990).

36. R. C. Batra and T. Gobinath, *Int. J. Impact Engng.*, **11** 1 (1991).

37. T. Gobinath and R. C. Batra, *Int. J. Engng. Sci.*, **29** 1315 (1991).

38. R. Jayachandran and R. C. Batra, *Acta Mechanica*, **92** 9 (1992).

39. R. C. Batra and R. Jayachandra, *Int. J. Impact Engng.*, **12** 209 (1992).

40. S. R. Bodner and Y. Partom, *J. Appl. Mech.*, **42** 385 (1975).

41. S. B. Brown, K. H. Kim and L. Anand, *Int. J. Plasticity*, **5** 95 (1989).

42. R. C. Batra and A. Adam, *Int. J. Engng. Sci.*, **29** 1391 (1991).

43. R. C. Batra and A. Adam, *Computers and Structures*, **42** 489 (1992).

44. L. S. Magness and T. Farrand, Deformation Behavior and Its Relationship to the Penetration Performance of High-Density KE Penetrator materials, *Proc. Army Science Conf.*, West Point, NY, 1990.

45. R. C. Batra, X. Zhang and T. W. Wright, *J. Appl. Mechs.*, **62**, 252 (1997).

46. A. M. Rajendran, High Strain Rate Behavior of Metals, Ceramics, and Concrete, Report #WL-TR-92-4006, Wright Patterson Air Force Base (1992).

47. R. G. Whirley and J. O. Hallquist, DYNA3D User's Manual (A Nonlinear, Explicit, Three-Dimensional Finite Element Code for Solid and Structural Mechanics, UCRL-MA-107254, Univ. of California, Lawrence Livermore national Lab., 1991.

48. R. C. Batra and Z. Peng, Development of Shear Bands in Dynamic Plane Strain Compression of Depleted Uranium and Tungsten Blocks, *Int. J. Impact Engng.*, **16**, 375 (1995).

49. R. C. Batra and J. B. Stevens, *Computer Methods in Appl. Mechs. & Engng*, **151**, 325 (1998).

50. M. Zhou, A. Needleman and R. J. Clifton, *J. Mech. Phys. Solids*, **42**, 423-458 (1994).

51. R. C. Batra and C. H. Kim, *Int. J. Plasticity*, **8**, 75-89 (1992).

52. B. Deltort, *J. de Physique*, Colloque C8 4, 447-452 (1994).

53. R. D. Dick, W. Ramachandran, J. D. Williams, R. W. Armstrong, W. H. Holt and W. Mock, Jr., Dynamic Deformation of W7Ni3Fe Alloy via Reverse-Ballistic Impact, in *Tungsten and Tungsten Alloys-Recent Advances*, (A. Crowson and E. S. Chen, eds.), The Minerals, Metals & Materials Society, 1991, pp. 269-276.

54. J. B. Stevens and R. C. Batra, Adiabatic Shear Bands in the Taylor Impact Test for a WHA Rod, *Int. J. Plasticity* (in press).

55. J. B. Stevens, Finite Element Analysis of Adiabatic Shear Banding in Impact and Penetration Problems, M.S. Thesis, Virginia Polytechnic Institute and State University, Blacksburg, 1996.

56. R. C. Batra and N. M. Wilson, Adiabatic Shear Bands in Plane Strain Deformations of a WHA, *Int. J. Plasticity*, 1998 (to appear).

57. N. V. Nechitailo and R. C. Batra, Penetration/Perforation of Aluminum, Steel and Tungsten Plates by Ceramic Rods, *Computers & Structures*, 1998 (to appear).

MASTER COPY: PLEASE KEEP THIS "MEMORANDUM OF TRANSMITTAL" BLANK FOR REPRODUCTION PURPOSES. WHEN REPORTS ARE GENERATED UNDER THE ARO SPONSORSHIP, FORWARD A COMPLETED COPY OF THIS FORM WITH EACH REPORT SHIPMENT TO THE ARO. THIS WILL ASSURE PROPER IDENTIFICATION. NOT TO BE USED FOR INTERIM PROGRESS REPORTS; SEE PAGE 1 FOR INTERIM PROGRESS REPORT INSTRUCTIONS.

MEMORANDUM OF TRANSMITTAL

March 3, 1998

U.S. Army Research Office
ATTN: AMXRO-ICA-L (Hall)
P.O. Box 12211
Research Triangle Park, NC 27709-2211

____ Reprint (Orig + 2 copies)

____ Technical Report (Orig + 2 copies)

____ Manuscript (1 copy)

__X__ Final Progress Report (Orig + 2 copies)

____ Related Material (1 copy)

CONTRACT/GRANT NUMBER: DAAH04-95-1-0042

TITLE: Robust Algorithms for Penetration Mechanics Problems

is forwarded for your information.

SUBMITTED FOR PUBLICATION TO (applicable only if report is manuscript):

Sincerely,

RCBatra

R. C. Batra 33866EG
Department of Engineering Science & Mechanics
Virginia Polytechnic Institute and State University
Blacksburg, VA 24061

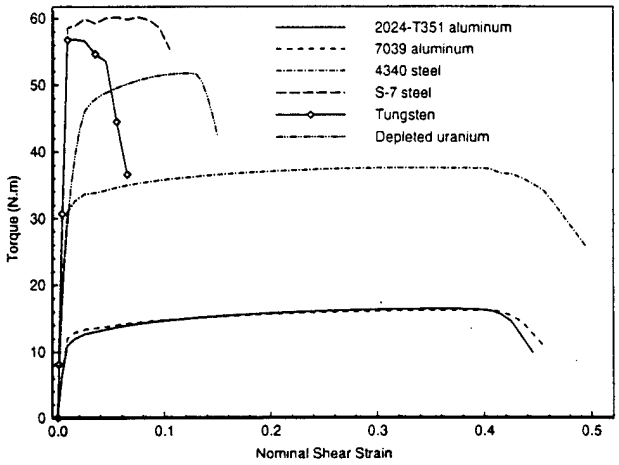

Fig. 1a. The torque required to deform the tube versus the nominal shear strain

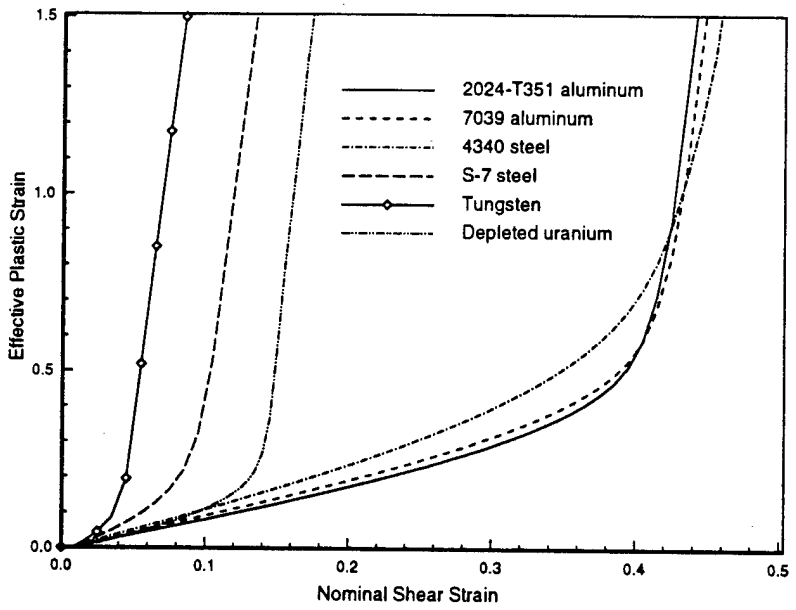

Fig. 1b. The effective plastic strain at the band center versus the nominal shear strain

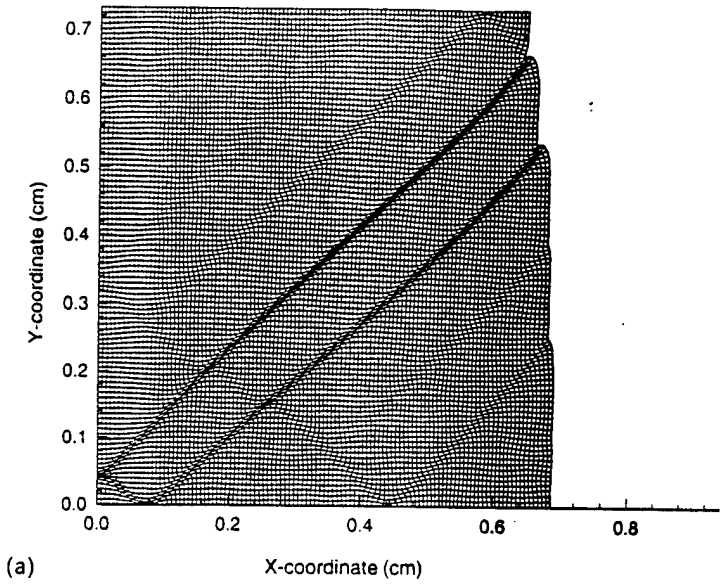

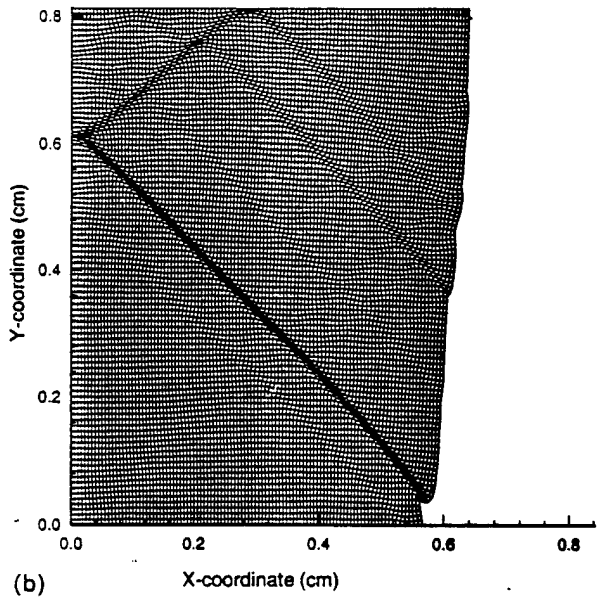

Fig. 2. Deformed meshes revealing the localization of deformation into shear bands; 300 weak elements were distributed randomly in the block:
(a) for uranium block at an average strain of 0.28, and
(b) for tungsten block at an average strain of 0.2.

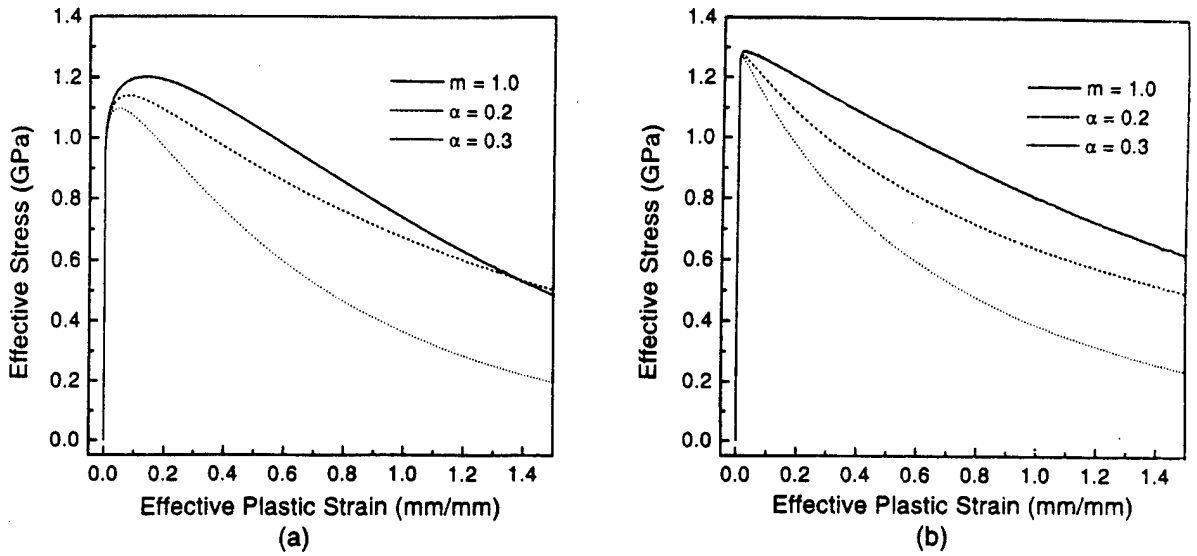

Fig. 3. Effective stress vs. effective strain during axisymmetric compression of homogeneous WHA and DU cylinders deformed at a nominal strain-rate of 5000/s.

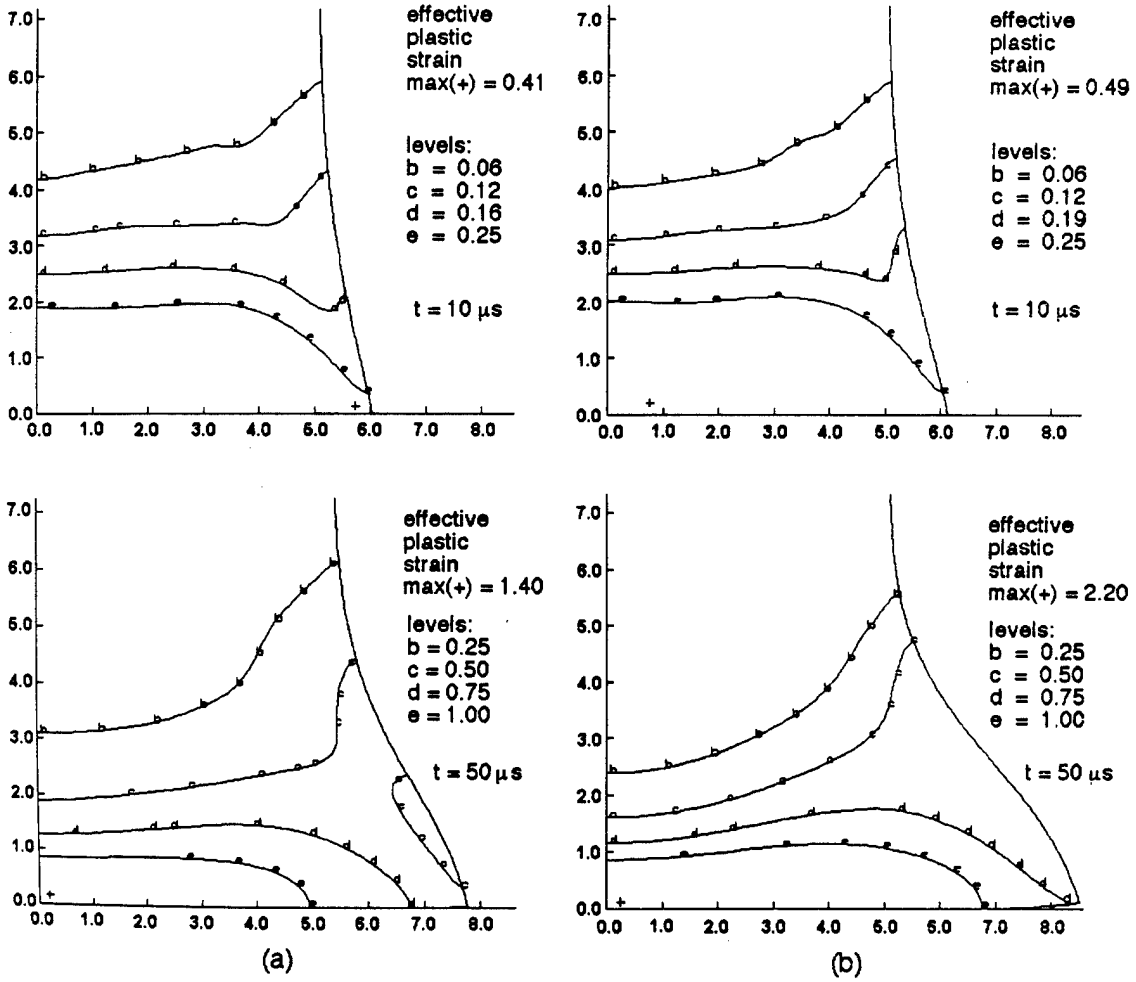

Fig. 4. Contours of the effective plastic strain at $t = 10$ μs and $t = 50$ μs in (a) the DU rod: (b) the WHA rod.

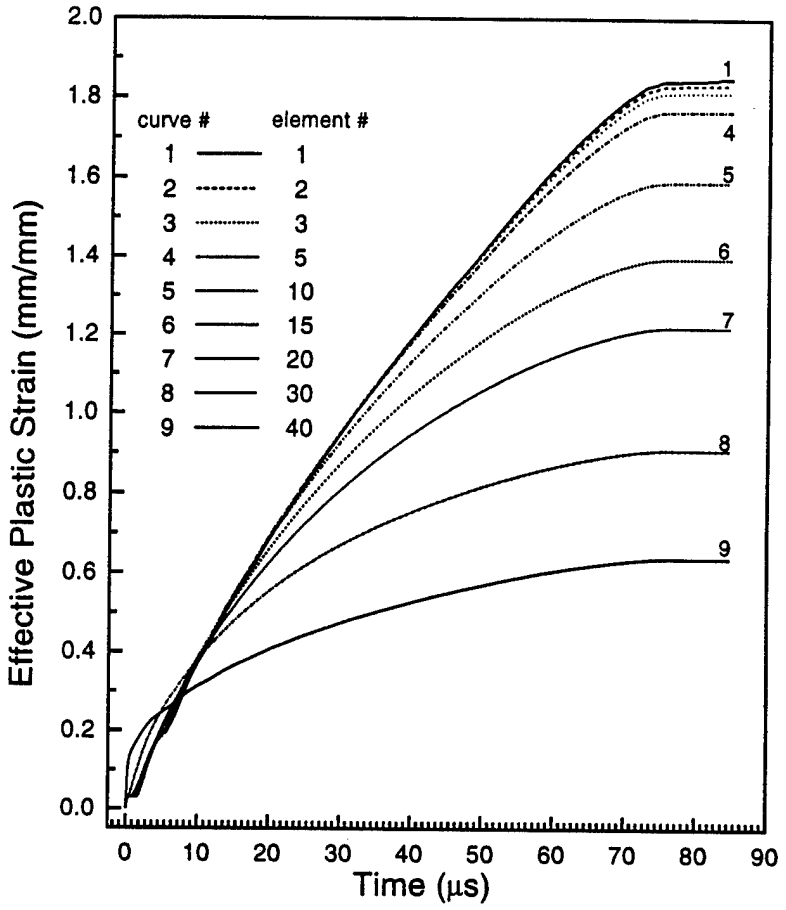

Fig. 5. Time history of the effective plastic strain at the centroids of several elements on a radial line in the impact face of the DU rod; elements are uniform and element 1 abuts the centroidal axis and 40 the mantle of the rod.

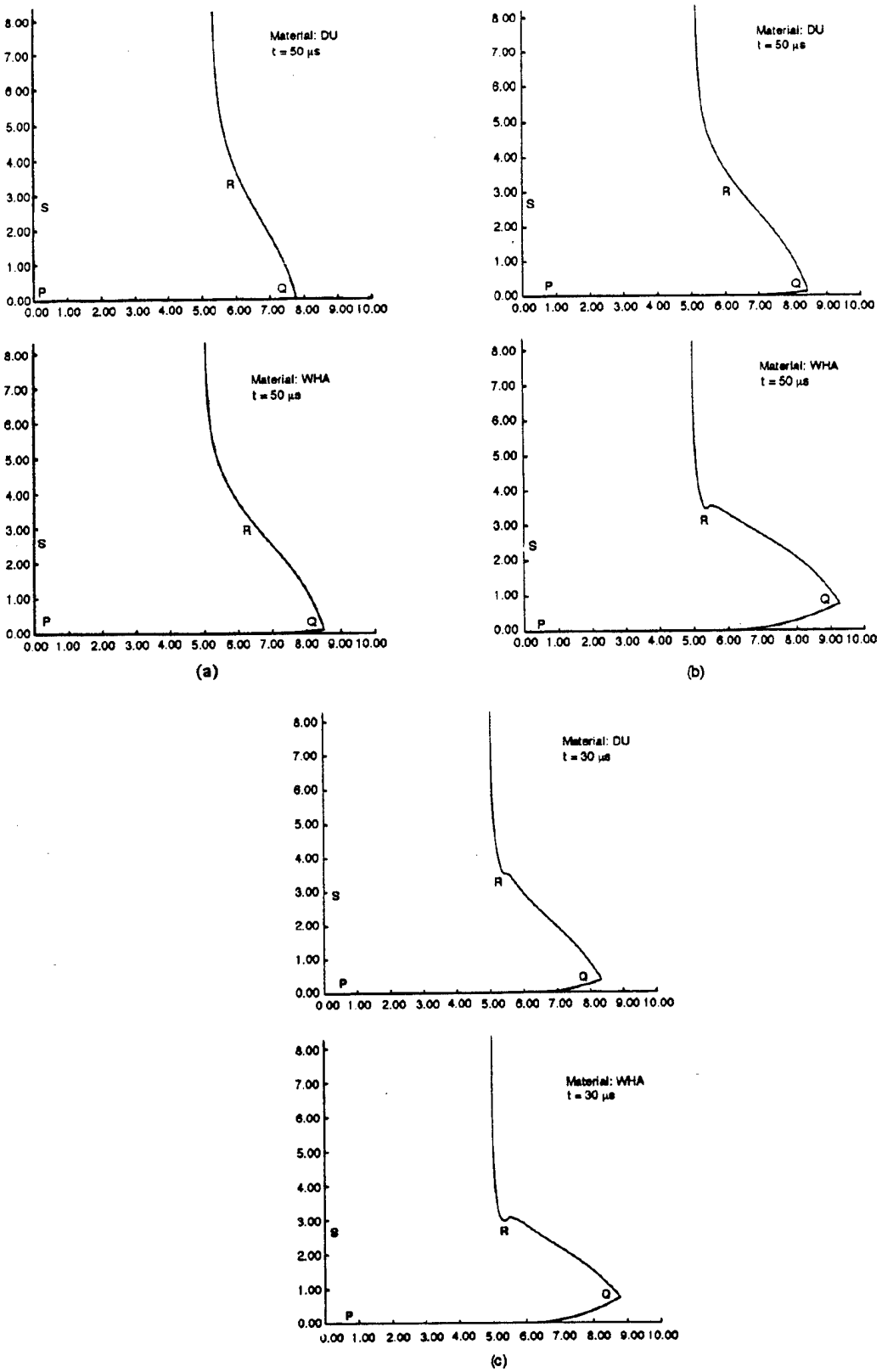

Fig. 6. Deformed shapes of the mushroomed regions for the DU and WHA rods; (a) Johnson-Cook thermal softening, $m = 1.0$; (b) Zhou et al. thermal softening, $\alpha = 0.2$; (c) Zhou et al. thermal softening, $\alpha = 0.3$.

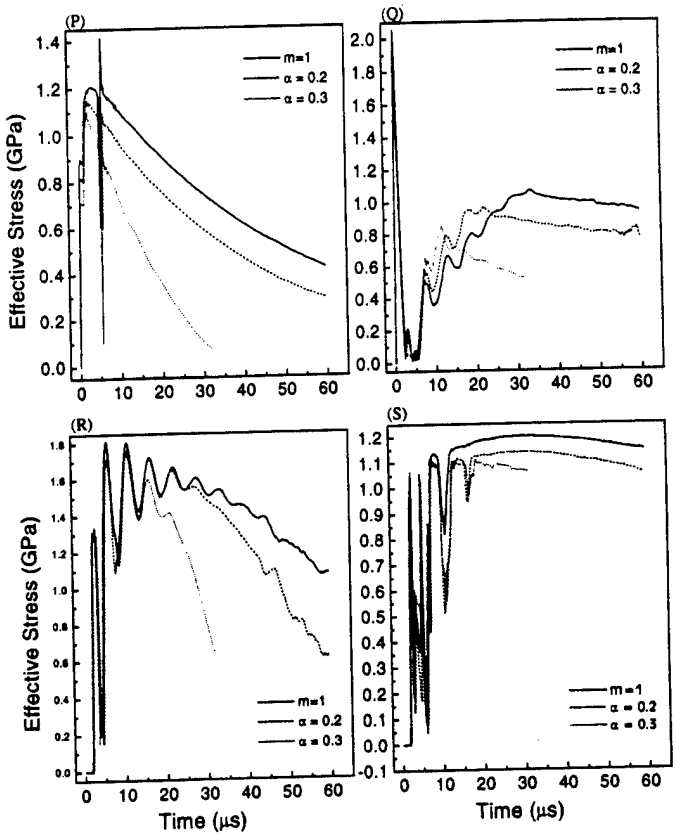

Fig. 7. Time history of the effective stress in elements in the DU rod located at point P, Q, R and S.

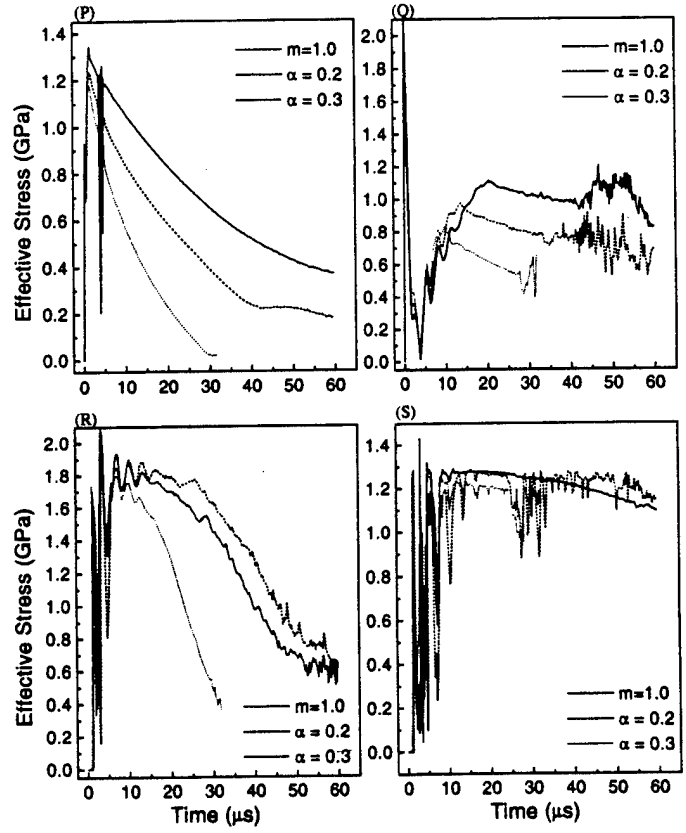

Fig. 8. Time history of the effective stress in elements in the WHA rod located at points P, Q. R and S.

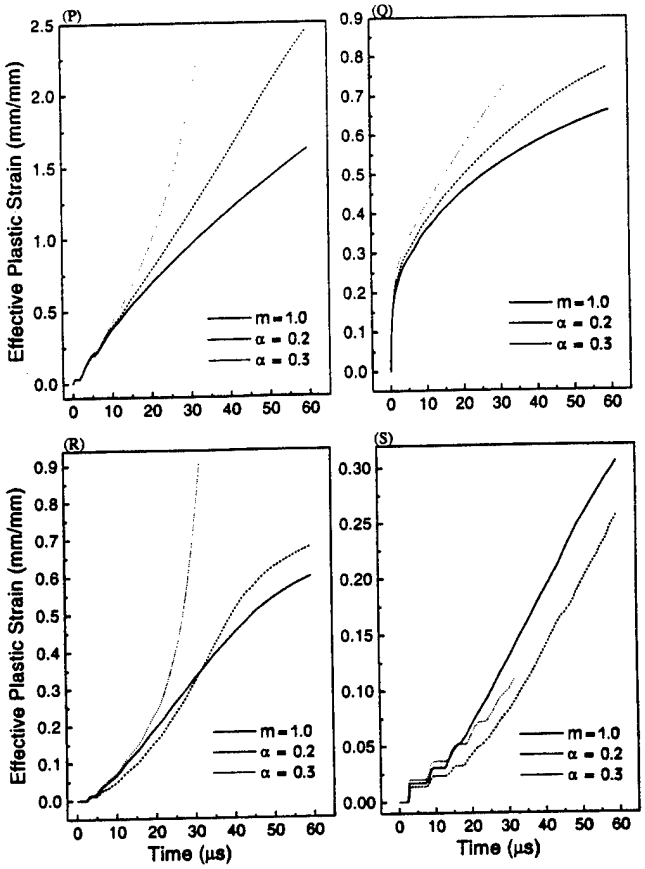

Fig. 9. Time history of the effective plastic strain in elements in the DU rod located at points P, Q, R and S.

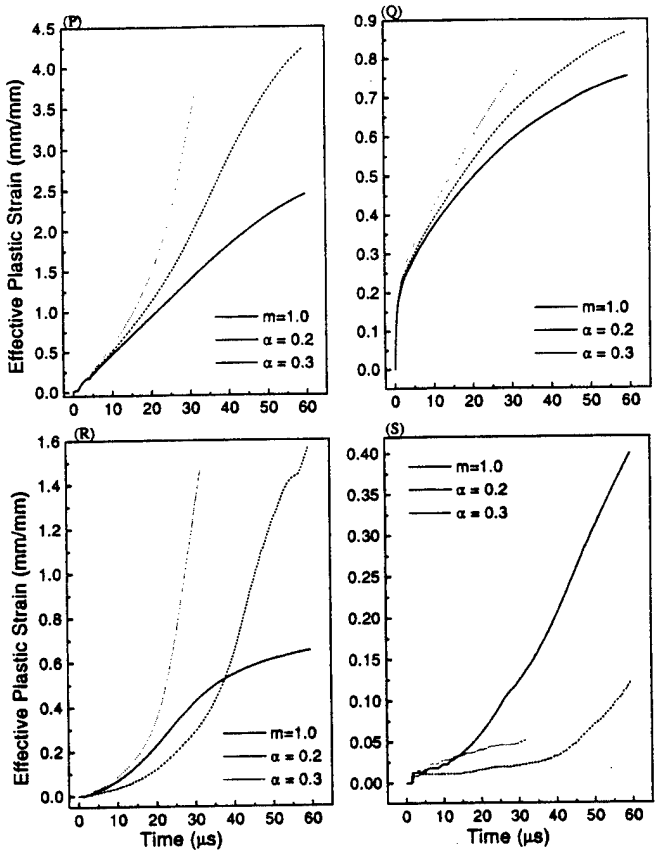

Fig. 10. Time history of effective plastic strain in elements in the WHA rod located at points p, Q, R and S.

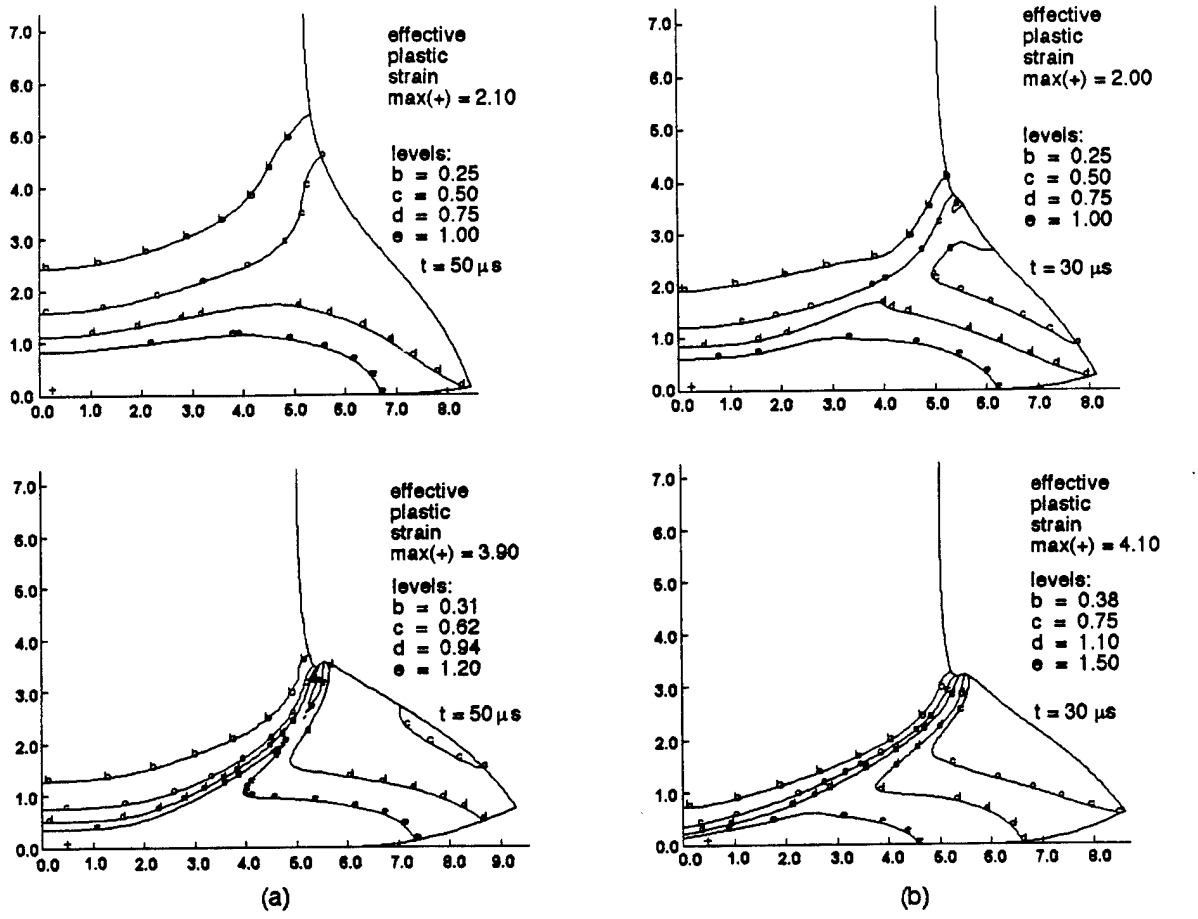

Fig. 11. Contours of the effective plastic strain in the deformed DU and WHA rods using the Zhou et al. thermal softening function with (a) $\alpha = 0.2$, at time, $t = 50$ μs and (b) $\alpha = 0.3$, at time, $t = 32$ μs.

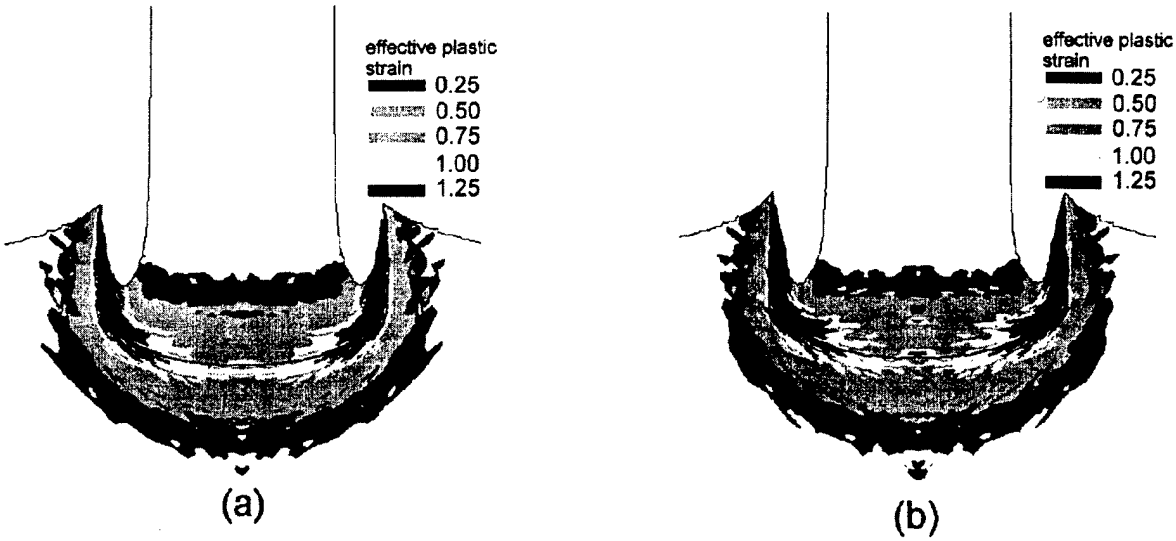

Fig. 12. Fringes of effetive plastic strain at time, $t = 10$ μs for (a) DU; (b) WHA penetrator.

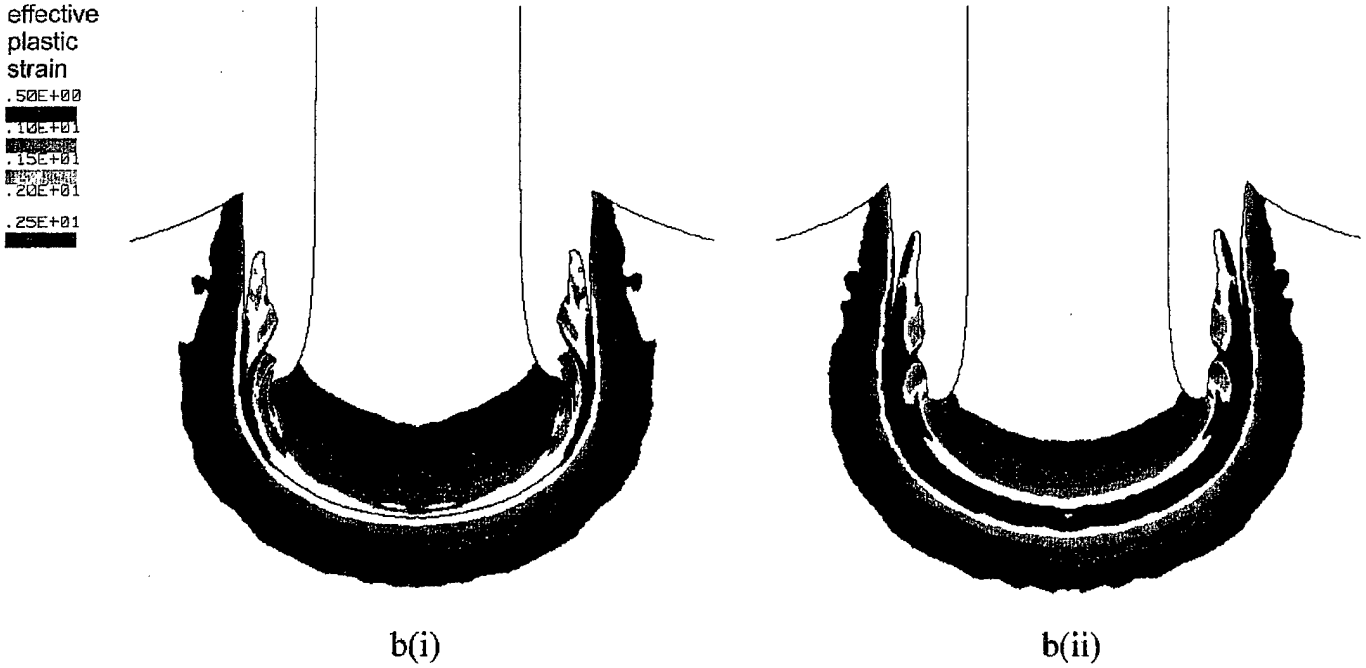

Fig. 13. Fringes of effective plastic strain at time, $t = 25$ μs for (a) DU, (b) WHA penetrator.

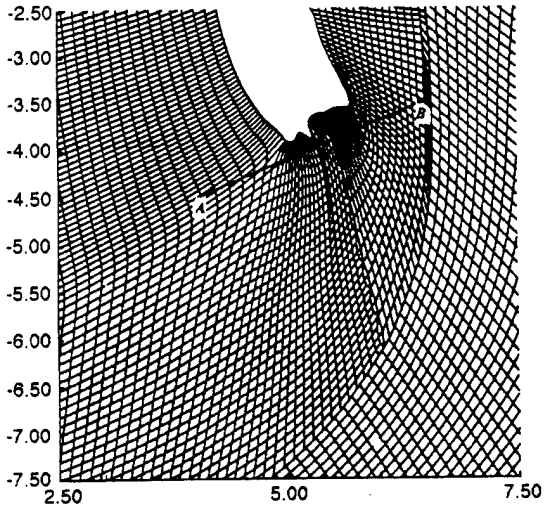

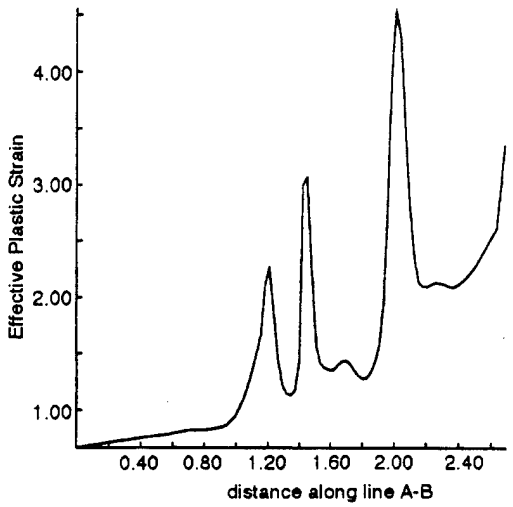

Fig. 14a. Deformed mesh of the ejecta of the DU rod at $t = 22.5$ μs, and the location of line AB on which the effective plastic strain is plotted in Fig. 14b.

Fig. 14b. Distribution of the effective plastic strain on line AB shown in Fig. 14a.

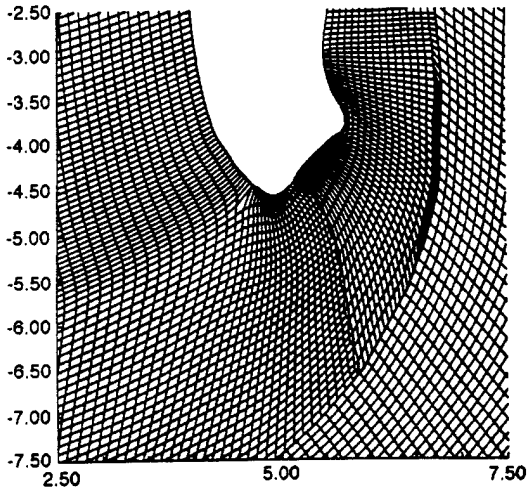

Fig. 15. Deformed mesh of the ejecta of the WHA rod at $t = 22.5$ μs.

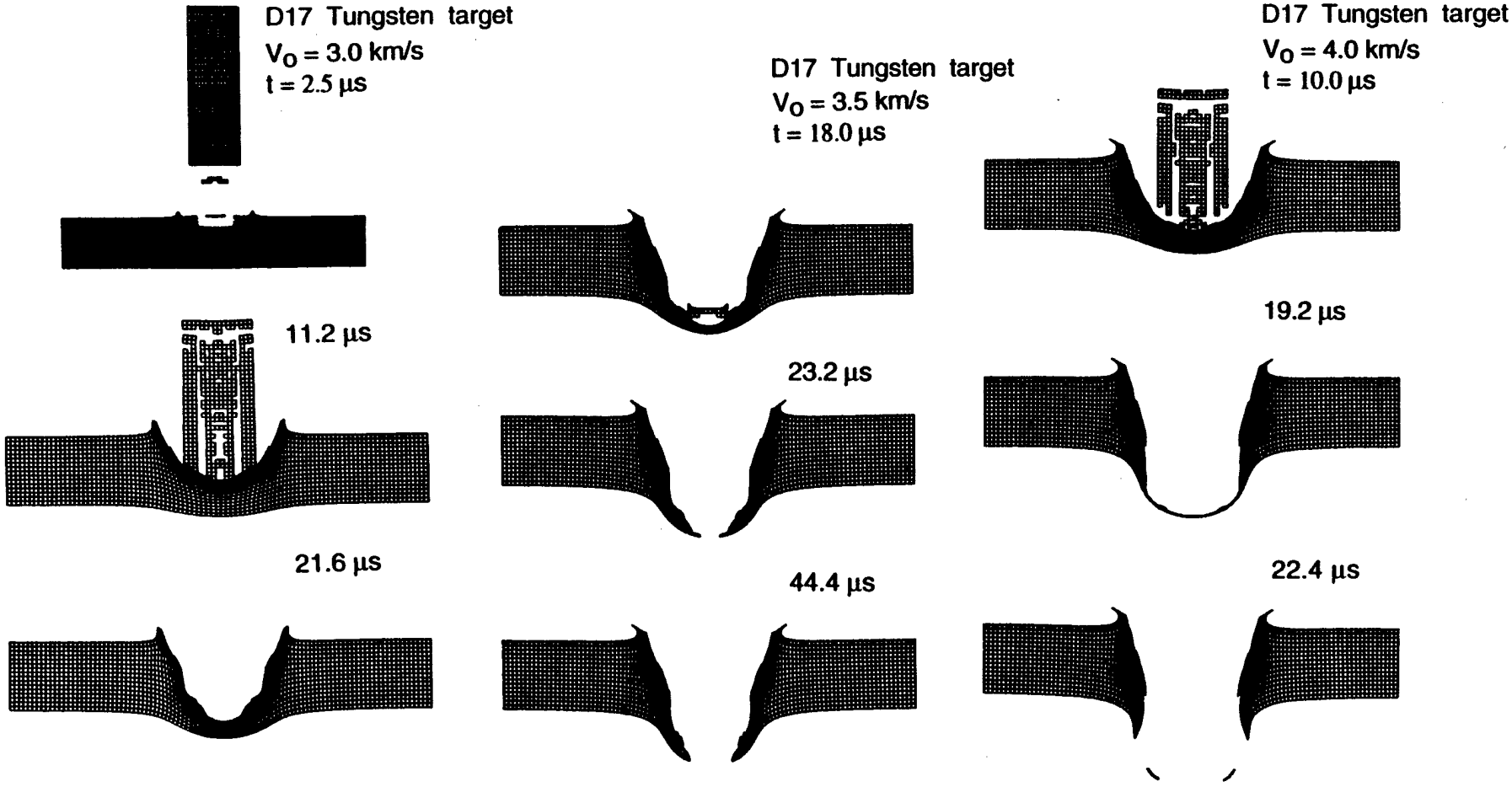

Fig. 16 Deformed configurations of the ceramic penetrator and the tungsten plate at different times and at impact speeds of 3 km/s, 3.5 km/s and 4 km/s.

PUBLICATIONS

a. Refereed Journals

1. R. C. Batra, C. Adulla and T. W. Wright, Effect of Defect Shape and Size on the Initiation of Adiabatic Shear Bands, *Acta Mechanica*, **116**, 239-243, 1996.
2. R. C. Batra, C. Adulla and T. W. Wright, A Comparison of 1-D and 3-D Simulations of the Twisting of a Thermoviscoplastic Tube, *Int. J. Plasticity*, **12**, 29-34, 1996.
3. R. C. Batra and Z. Peng, Development of Shear Bands in Dynamic Plane Strain Compression of Depleted Uranium and Tungsten Blocks, *Int. J. Impact Eng'g*, **16**, 375-395, 1995.
4. Y. Wu and R. C. Batra, An Engineering Penetration/Perforation Model of Hemispherical Nosed Rigid Cylindrical Rods into Strain- Hardening Targets, *Computers & Structures*, **58**, 51-58, 1996.
5. R. C. Batra and Z. Peng, Development of Shear Bands during the Perforation of a Steel Plate, *Computational Mechs.*, **17**, 326-334, 1996.
6. Xingju Chen and R. C. Batra, Deep Penetration of Thick Thermoviscoplastic Targets by Long Rigid Rods, *Computers & Structures*, **54**, 655-670, 1995.
7. R. C. Batra and J. B. Stevens, Adiabatic Shear Bands in Axisymmetric Impact and Penetration Problems, *Computer Methods in Appl. Mechs. and Eng'g*, **151**, 325-342, 1998.
8. J. B. Stevens and R. C. Batra, Adiabatic Shear Bands in the Taylor Impact Test for a WHA Rod, *Int. J. Plasticity* (accepted).
9. R. C. Batra and N. M. Wilson, Adiabatic Shear Bands in Plane Strain Deformations of a WHA, *Int. J. Plasticity* (in press).
10. N. V. Nechitailo and R. C. Batra, Penetration/Perforation of Aluminum, Steel and Tungsten Plates by Ceramic Rods, *Computers & Structures*, (in press)

b. Chapter in a Book

11 R. C. Batra, Numerical Solution of Initial-Boundary-Value Problems with Shear Strain Localization, *in Localization and Fracture Phenomenon in Inelastic Solids* (P. Perzyna, ed.), Springer-Verlag, 1998, (in press).

c. Conference Proceedings

12 R. C. Batra and Y. Wu, Axisymmetric Penetration of Steel Targets by Hollow Cylindrical Tubes, in *Metallurgical and Materials Applications of Shock-Wave and High-Strain-Rate Phenomena*, L. E. Murr, Ed., Elsevier, 337-344, 1995.

13 R. C. Batra, The Speed of Propagation of Adiabatic Shear Bands in Thermoviscoplastic Materials, in *AEPA '96 Proceedings of the 3rd Symp. on Advances in Engineering Plasticity and its Applications*, T. Abe and T. Tsuta, eds., Pergamon Press, 105-110, 1996.

14 Z. Peng and R. C. Batra, Propagation of Shear Bands in Thick-Walled RHA Steel Tubes, *Computational Mechs* '95, S. N. Atluri, Y. Yagawa and T. A. Cruse, Eds., Springer-Verlag, 2034-2039, 1995.

15 F. Flocker and R. C. Batra, Axisymmetric Penetration of Ceramic Plates by Tungsten Rods, in Impact, Waves, and Fracture, (R. C. Batra, A. K. Mal and G. P. MacSithigh, eds.), ASME, 89-99, 1995.

16 N. V. Nechitailo and R. C. Batra, Axisymmetric Penetration of Steel Circular Plates by Ceramic Rods, in *Metallurgical and Materials Applications of Shock-Wave and High-Strain-Rate Phenomena*, L. E. Murr, Ed., Elsevier, 543-550, 1995.

17 J. B. Stevens and R. C. Batra, Axisymmetric Deformations of DU and WHA Rods Impacting a Rigid Target, in *Plasticity and Impact Mechanics*, N. K. Gupta, ed., New Age Int. Ltd., Publishers, New Delhi, India, 449-465, 1996.

18 R. C. Batra and J. B. Stevens, On the L/D Effect in the Taylor Impact Test, *Advances in Computational Eng'g Sci.* (S. N. Atluri and G. Yagawa, eds.) Tech. Sci. Press, Forsyth, Georgia, 1134-1139, 1997.

19 R. C. Batra and J. B. Stevens, Adiabatic Shear Bands in Taylor Impact Tests and Axisymmetric Penetration Problems, *Proc. U.S. Army Symp. on Solid Mechs.* (K. Iyer and S. Chou, eds.) Battele Press, Columbus, 241-251, 1997.

d. Presentations

20 R. C. Batra and J. B. Stevens, On the L/D Effect in the Taylor Impact Test, *Int. Conf. on Computational Engineering Sci.*, San Jose, Costa Rica, May 4-9, 1997.

21 J. B. Stevens and R. C. Batra, Axisymmetric Deformations of DU and WHA Rods Impacting a Rigid Target, *Int. Symp. on Plasticity and Impact Mechanics*, I.I.T., Delhi, December 11-14, 1996.

22 R. C. Batra and J. B. Stevens, Adiabatic Shear Bands in Taylor Impact Tests and Axisymmetric Penetration Problems, *14th U.S. Army Symp. on Solid Mechs.*, Myrtle Beach, October 1996.

23 R. C. Batra, The Speed of Propagation of an Adiabatic Shear Band in Thermoviscoplastic Materials, *2nd Asia-Pacific Symp. on Advances in Eng'g Plasticity and Its Applications*, Hiroshima, Japan, Aug. 1996.

24 R. C. Batra, Analysis of Adiabatic Shear Bands and Penetration Problems by Adaptively Refined Meshes, *Army Workshop on Recent Advances in Computational Structural Dynamics and High-Performance Computing*, Vicksburg, MS, April 24-26, 1996.

25 R. C. Batra, Analysis of Adiabatic Shear Bands and Penetration Problems, Seminar, Army Research Lab., Aberdeen, MD, June 1996.

26 R. C. Batra, Analysis of Adiabatic Shear Bands in Thermoviscoplastic Materials, *33rd Annual Technical Meeting of the Society of Eng'g. Science*, Arizona State Univ., Tempe, AZ, October 1996.

27 R. C. Batra and Z. Peng, Development of Shear Bands in Dynamic Plane Strain Compression of Depleted Uranium and Tungsten Blocks, *ASME Winter Annual Meeting*, Chicago, IL, Nov. 1994.

28 R. C. Batra, A Comparison of the Dynamic Response of Tungsten and Depleted Uranium, *Recent Developments in Tungsten and Tungsten Alloys for Anti-Armor Applications*, Picatinny Arsenal, NJ, 11-12 September 1995.

29 F. W. Flocker and R. C. Batra, Axisymmetric Penetration of Ceramic Plates by Tungsten Rods, *ASME Mechanics and Materials Conf.*, The Univ. of California, Los Angeles, June 1995.

30 R. C. Batra and Z. Peng, Analysis of Localization of Deformation in High Speed Punching of a Steel Plate by Using Adaptively Refined Meshes, *3rd U.S. National Congress on Computational Mechanics*, Dallas, June 1995.

31 N. V. Nechitailo and R. C. Batra, Penetration of Steel Plates by Long Ceramic Rods, *Explomet '95*, Univ. of Texas at El Paso, August 1995.

e. Technology Transfer

1. Dr. T. W. Wright of the ARL, Aberdeen, MD visited with the PI and also gave a Departmental Seminar in February, 1995. He and the PI co-organized a symposium "Finite Deformation Viscoplasticity" in conjunction with the ASME Winter Annual Meeting, San Francisco; the proceedings of the symposium have been published by the Materials Division as Vol. 69-1 (1995). The two also initiated research work resulting in two journal publications (see section a) and some additional work is in progress.

2. The PI and Dr. A. M. Rajendran of the ARL, Aberdeen, MD organized a symposium "Constitutive Laws: Theory and Applications" in conjunction with the 1995 Int. Conf. on Comp. Meth. in Engineering, Hawaii. The papers presented at the Symposium have been published in a book (edited by A. M. Rajendran and R. C. Batra) by the CIMNE, Barcelona, Spain.

3. The PI co-organized a symposium and coedited the book "Impact, Waves and Fracture" published by the ASME Press.

4. The PI and Dr. A. M. Rajendran of the ARL, Aberdeen, MD co-organized a symposium on Penetration and Impact Mechanics in conjunction with the 5th Int. Symposium on Plasticity and its Applications, 14-18 July 1997, Juneau, Alaska, July 1997.

5. The PI visited the ARL Laboratory on June 16, 1996, gave a seminar outlining his ARO supported work on Penetration Mechanics, and interacted with Drs. Lee Magness, Kent Kimsey, M. Raftenberg, J. Walter, M. Scheidler and T. W. Wright.

6. The PI participated in the ARO Symposium on Solid Mechanics held in Myrtle Beach, South Carolina, and in the Army Workshop on Recent Advances in Computational Structural Dynamics and High-Performance Computing held at the Vicksburg Waterways Station.

7. The PI and Dr. A. M. Rajendran are coorganizing a symposium on Contitutive Relations for High Strain Rate Deformations at the forthcoming Int. Mechanical Engineering Congress & Exposition, Anaheim, CA, Nov. 1998.

8. Drs. Mike Scheideler, A. M. Rajendran and Scott Schoenfeld of the ARL visited with the PI in 1997 and 1998, discussed the ongoing ARO supported work, and gave seminars in the ESM Department.

9. The PI and Dr. A. M. Rajendran organized a Symposium on Penetration and Impact Problems for the International Congress on Computational Engineering Science, San Jose, Costa Rica, May 1997.

10. The PI gave a series of 7 lectures on Numerical Solution of Initial-Boundary-Value Problems Involving Adiabatic Shear Bands at the Int. Center of Mechanical Sciences, Udine, Italy in October 1997. These lectures will be published by Springer-Verlag.

SCIENTIFIC PERSONNEL SUPPORTED

R. C. Batra
N. V. Nechitailo, M.S. degree completed Dec. 1995.
J. B. Stevens, M.S. degree completed Dec. 1996.
M. V. S. Ravisankar, Ph.D. degree in progress.
N. Jaber, Ph.D. degree in progress.
J. Xiang, Ph.D. degree in progress.
A. Ionita, Ph.D. degree in progress.
J. Zhang, Ph.D. degree in progress.

DEGREES AWARDED

N. V. Nechitailo, M.S., Dec. 1995
J. B. Stevens, M.S., Dec. 1997

HONORS & AWARDS

Lecturer in a short course on Localization and Fracture Phenomenon in Inelastic Solids, Int. Center for Mech'l Sciences, Udine, Italy, Oct. 1997.

Associate Technical Editor, *ASME J. of Engineering Materials and Technology*

Member - National Research Council Panel on Armors and Armaments (1996-98)

Managing Editor - Computational Mechanics

Listed in Who's Who in America

1997 Virginia Tech, Dean of Eng'g Award for Excellence in Research

Elected Fellow of the Society of Engineering Science, Inc.

APPENDIX

Out of the ten publications in refereed journals, a copy of the following three papers is included.

1. R. C. Batra and J. B. Stevens, Adiabatic Shear Bands in Axisymmetric Impact and Penetration Problems, *Computer Meth. in Appl. Mechs. and Eng'g*, **151**, 325-342, 1998.
2. R. C. Batra and N. M. Wilson, Adiabatic Shear Bands in Plane Strain Deformations of a WHA, *Int. J. Plasticity*, 1998 (to appear).
3. N. V. Nechitailo and R. C. Batra, Penetration/Perforation of Aluminum, Steel and Tungsten Plates by Ceramic Rods, *Computers & Structures*, 1998 (to appear).

ELSEVIER

Comput. Methods Appl. Mech. Engrg. 151 (1998) 325–342

Computer methods in applied mechanics and engineering

Adiabatic shear bands in axisymmetric impact and penetration problems

R.C. Batra*, J.B. Stevens

Department of Engineering Science and Mechanics, Virginia Polytechnic Institute and State University, Blacksburg, VA 24061-0219, USA

This paper is dedicated with deep respect to Professor J. Tinsley Oden on his 60th birthday

Received 17 January 1997

Abstract

We study axisymmetric deformations of depleted uranium (DU) and tungsten heavy alloy (WHA) rods impacting at normal incidence either a flat rigid or a thick steel target. Each deformable material is modeled as elastic thermoviscoplastic; its flow stress increases with an increase in the effective plastic strain and effective plastic strain-rate but decreases with a rise in the temperature. An objective of this work is to ascertain when and where a shear band, defined as a narrow region of rapid, intense plastic deformation, forms in each material. The Taylor impact simulations show that shear bands form earlier in WHA than in DU for material parameters used. In the penetration simulations, shear bands form continuously in the ejecta of the DU penetrator but only one shear band occurs in the WHA ejecta followed by its more uniform deformations.

1. Introduction

Magness and Farrand [1] have conducted penetration tests involving identical cylindrical rods made of depleted uranium (DU) and tungsten heavy alloy (WHA) impacting steel targets at normal incidence. They observed that DU rods penetrate deeper than WHA rods, the tunnel diameter is smaller for a DU rod than that for a WHA rod and the tunnel surface is rough for DU penetrators, while essentially smooth for WHA penetrators. They explained these differences by postulating that shear bands develop continuously in the DU rod, causing fractures and hence sharper nose shapes. However, in the WHA rod, shear bands develop later and probably do not cause as many fractures as in the DU rod. Consequently, the nose shape remains blunted for longer durations. In their numerical simulation of torsional deformations of thin-walled cylindrical tubes of DU and WHA, Batra et al. [2] found that shear bands, indicated by the sharp drop in the torque required to deform the tube, developed sooner in WHA than in DU. Batra and Peng [3] obtained a similar result during their numerical study of thermomechanical deformations of DU and WHA rectangular blocks containing randomly distributed weak elements and deformed in plane strain compression. In each case the material's flow strength was assumed to depend upon the effective plastic strain, effective plastic strain-rate and temperature through the Johnson–Cook relation. Of course, the stress-state at points close to the penetrator nose is quite different from that occurring either in a simple shear test or in plane strain compression test. Batra and Ko [4] found that shear bands initiate much later in a steel specimen deformed in axisymmetric compression as compared to that in

* Corresponding author.

0045-7825/98/$19.00 © 1998 Elsevier Science S.A. All rights reserved
PII S0045-7825(97)00156-4

plane strain compression. Their computed results with and without frictional forces at the contact surfaces revealed that the cylindrical specimens barrelled in the former case and reverse barrelling ensued in the latter case. They used a rather high value of the thermal softening coefficient to accelerate the development of a shear band. Subsequent unpublished work has shown that values of thermal softening coefficients for steels listed in Rajendran's report [5] for use in the Johnson–Cook relation do not result in the initiation of adiabatic shear bands in axisymmetric compression to a nominal strain of 0.5.

Here, we study axisymmetric thermomechanical deformations of identical DU and WHA rods impacting at normal incidence the flat surface of either a massive rigid target; or a thick steel target; the former test is known as the Taylor Impact Test. Taylor [6] analysed this impact configuration by assuming that when the flow stress is exceeded in the impacting projectile cylinder, a mushroomed region forms near the impacted end. The mushroomed region can be regarded as stationary and separate from the undeformed material which continues to move in the direction of impact. Taylor assumed a constant flow stress of the material and related it to the final dimensions of the deformed projectile. Jones et al. [7,8] improved upon Taylor's analysis of the problem by dividing it into two phases. The first high strain-rate phase ends with the attenuation of shock waves initiated by the impact. It is followed by a period of lower strain-rate plastic deformations characterized by plastic waves propagating at a uniform speed. These analyses are essentially one-dimensional and cannot predict details of the deformed configuration of the projectile. Extensive experimental studies have shown that the Taylor model yields very approximate values of the dynamic yield strength [9–11] of the rod material. Wilkins and Guinan [12] have shown that the two-dimensional finite difference method provides acceptable predictions of the mushroom profiles. These methods require a priori knowledge of the dependence of the flow stress upon the effective plastic strain, the effective plastic strain-rate and the temperature. If necessary, such dependences can be determined iteratively.

The foregoing studies have not reported any information on the occurrence of adiabatic shear bands in the mushroomed region. Dick et al. [13] conducted reverse ballistic impact tests (a.k.a. Taylor Impact) on WHA rods with ellipsoidal tungsten particles in an Fe–Ni matrix and also examined the deformed rods for fracture. At an impact speed of 173 m/s, the mushroomed end had a slight ellipticity which they attributed to radial cracks distributed in the body. At the higher impact speed of 228 m/s, the deformation was found to be more localized along a curved path extending from the transition between the mushroomed region and the undeformed rod toward the impact face. Diametrically opposite to this section, they observed ductile fracture along a similar path. Apparently, fracturing of WHA rods followed shear bands that had propagated to the mantle of the rod. Some tungsten particles were also deposited on the steel target.

In our simulations of the penetration problem and the Taylor impact test, the flow stress of each deformable material is assumed to increase with the effective plastic strain and effective plastic strain-rate but decrease with a rise in the temperature. Once a material point has melted, it is assumed to behave like an ideal fluid. We consider the effect of inertia forces but neglect the effect of heat conduction.

2. Formulation of the problem

We use the Lagrangian or referential description of motion to describe dynamic, thermomechanical and axisymmetric deformations of a cylindrical rod impacting at normal incidence a target. Their deformations are governed by the following balance laws of mass, linear momentum, moment of momentum and internal energy; details of these laws may be found in [14].

$$(\rho J)^{\cdot} = 0\,, \tag{1}$$

$$\rho_0 \dot{\boldsymbol{v}} = \mathrm{Div}\,\boldsymbol{T}\,, \tag{2}$$

$$\boldsymbol{T}\boldsymbol{F}^{\mathrm{T}} = \boldsymbol{F}\boldsymbol{T}^{\mathrm{T}}\,, \tag{3}$$

$$\rho_0 \dot{e} = \mathrm{tr}(\boldsymbol{T}\dot{\boldsymbol{F}}^{\mathrm{T}})\,, \tag{4}$$

$$\boldsymbol{F} = \mathrm{Grad}\,\boldsymbol{x}\,. \tag{5}$$

Here, $\boldsymbol{x}$ gives the present position of the material particle that occupied place $\boldsymbol{X}$ in the reference configuration, ρ is its present mass density, ρ_0 its mass density in the reference configuration, $\boldsymbol{v}$ its velocity, $\boldsymbol{T}$ the first

Piola–Kirchhoff stress tensor, $\boldsymbol{F}$ the deformation gradient, $J = \det \boldsymbol{F}$, e the specific internal energy, $\boldsymbol{F}^{\mathrm{T}}$ the transpose of $\boldsymbol{F}$, and a superimposed dot indicates the material time derivative. The operators Div and Grad signify, respectively, the divergence and gradient operators with respect to referential coordinates and tr denotes the trace operator. In Eq. (4) the effect of heat conduction has been neglected. This is justified since we are interested in the short term response of the impacting bodies during which time the effects of heat conduction are likely to be negligible. This assumption facilitates the computation of the temperature rise from the incremental plastic work done without numerical integration of the balance of internal energy. Eqs. (1)–(5) are supplemented with the following constitutive relations.

$$\boldsymbol{T} = J\boldsymbol{\sigma}(\boldsymbol{F}^{-1})^{\mathrm{T}}, \qquad \boldsymbol{\sigma} = -p\mathbf{1} + \boldsymbol{S}, \qquad p = K(\rho/\rho_0 - 1), \tag{6}$$

$$\overset{\nabla}{\boldsymbol{S}} = 2\mu(\overline{\boldsymbol{D}} - \overline{\boldsymbol{D}}^{\mathrm{p}}), \qquad \overset{\nabla}{\boldsymbol{S}} = \dot{\boldsymbol{S}} + \boldsymbol{S}\boldsymbol{W} - \boldsymbol{W}\boldsymbol{S}, \tag{7}$$

$$\boldsymbol{D} = \frac{1}{2}(\operatorname{grad}\boldsymbol{v} + (\operatorname{grad}\boldsymbol{v})^{\mathrm{T}}), \qquad \boldsymbol{W} = \frac{1}{2}(\operatorname{grad}\boldsymbol{v} - (\operatorname{grad}\boldsymbol{v})^{\mathrm{T}}), \tag{8}$$

$$\overline{\boldsymbol{D}} = \boldsymbol{D} - \frac{1}{3}(\operatorname{tr}\boldsymbol{D})\mathbf{1}, \qquad \operatorname{tr}\boldsymbol{D}^{\mathrm{p}} = 0, \qquad \boldsymbol{D}^{\mathrm{p}} = \Lambda\boldsymbol{S}, \qquad S_e^2 \equiv \frac{3}{2}\operatorname{tr}(\boldsymbol{S}\boldsymbol{S}^{\mathrm{T}}), \tag{9}$$

$$\dot{e} = c\dot{\theta} + \operatorname{tr}(\boldsymbol{\sigma}\boldsymbol{D}^{\mathrm{e}}), \qquad \sigma_y = (A + B(\epsilon^{\mathrm{p}})^n)(1 + C\ln(\dot{\epsilon}^{\mathrm{p}}/\dot{\epsilon}_0))(1 - T^m), \tag{10}$$

$$T = (\theta - \theta_0)/(\theta_m - \theta_0), \qquad (\dot{\epsilon}^{\mathrm{p}})^2 = \frac{2}{3}\operatorname{tr}(\boldsymbol{D}^{\mathrm{p}}\boldsymbol{D}^{\mathrm{p}}). \tag{11}$$

Here, $\boldsymbol{\sigma}$ is the Cauchy stress tensor, $\boldsymbol{S}$ its deviatoric part, p the hydrostatic pressure taken to be positive in compression, K the bulk modulus, μ the shear modulus, $\overset{\nabla}{\boldsymbol{S}}$ the Jaumann derivative of $\boldsymbol{S}$, $\overline{\boldsymbol{D}}$ the deviatoric strain-rate, $\boldsymbol{D}^{\mathrm{p}}$ the plastic strain-rate, $\boldsymbol{D}^{\mathrm{e}}$ the elastic strain-rate, $\boldsymbol{D} = \boldsymbol{D}^{\mathrm{e}} + \boldsymbol{D}^{\mathrm{p}}$ the strain-rate tensor, $\boldsymbol{W}$ the spin tensor, c the specific heat, θ the temperature of a material particle, θ_m its melting temperature, θ_0 the room temperature, T the homologous temperature, S_e the effective stress, and ϵ^{p} the effective plastic strain. Eq. $(6)_3$ implies that the volumetric response of the material is elastic. Eq. $(6)_1$ is the constitutive relation in terms of deviatoric stresses for a linear, isotropic hypoelastic material, grad $\boldsymbol{v}$ equals the gradient of the velocity field with respect to coordinates in the present configuration, Eq. $(9)_4$ signifies the von Mises yield criterion with isotropic hardening, and Eq. $(10)_2$ is the Johnson–Cook [15] relation. The flow stress, σ_y, increases with an increase in the effective plastic strain and the effective plastic strain rate but decreases with an increase in the temperature of a material particle. Truesdell and Noll [14] have pointed out that Eq. $(7)_1$ is not invariant with respect to the choice of different objective (or material frame indifferent) time derivatives of the stress tensor. In Eq. $(10)_2$ parameters B and n characterize the strain hardening of the material, C and $\dot{\epsilon}_0$ its strain-rate hardening and $(1 - T^m)$ its thermal softening. Eq. $(9)_3$ signifies that the plastic strain-rate is along the normal to the yield surface $(9)_4$, and the factor of proportionality Λ is given by

$$\Lambda = 0 \quad \text{when either } S_e < \sigma_y, \quad \text{or} \quad S_e = \sigma_y \quad \text{and} \quad \operatorname{tr}(\overset{\nabla}{\boldsymbol{S}}\boldsymbol{S}) < 0; \tag{12}$$

otherwise it is a solution of

$$S_e = (A + B(\epsilon^{\mathrm{p}})^n)\left(1 + C\ln\left(\frac{2}{3}\Lambda S_e/\dot{\epsilon}_0\right)\right)(1 - T^m). \tag{13}$$

Once $\theta = \theta_m$ at a material point, the flow stress, σ_y, for the material point is set equal to zero. It then behaves like a compressible, nonviscous fluid. In physical experiments, fracture in the form of a crack will ensue from the point much before it is heated up to its melting temperature. Here, we have not incorporated any fracture criterion into the problem formulation. Because a Lagrangian formulation is used and a perfect fluid cannot support shear stresses, once a material point melts, the mesh will be distorted quickly and the computations must be stopped.

Zhou et al. [16] found that the thermal softening of the WHA they tested is better described by $(1 - \beta(-1 + (\theta/\theta_0)^{\alpha}))$ where α and β are material parameters and for their WHA, $\beta = 2.4$ and $\alpha = 0.2$. We will investigate the effect of replacing $(1 - T^m)$ in Eq. $(10)_2$ by Zhou et al.'s expression.

Initially, the cylindrical rod is stress free, at room temperature θ_0 and is moving with a uniform speed V_0 in a direction normal to the plane surface of the target, and strikes it at time $t = 0$. All bounding surfaces of the rod

except that contacting the target are taken to be traction free. Because of the assumption of locally adiabatic deformations, no thermal boundary conditions are needed.

In the Taylor Impact test, the target is taken as rigid and stationary, and the contact surfaces smooth. The deformable steel target is initially at rest, at room temperature θ_0 and is stress free. It is unconstrained and all of its bounding surfaces except the one contacting the penetrator are taken to be traction free. On the target/penetrator interface, the normal component of relative velocity between the target and penetrator vanishes, and

$$f_t = -|f_n|(\mu_s + (\mu_k - \mu_s)\,e^{-\gamma|\bar{v}|})\bar{v}/|\bar{v}|\,. \tag{14}$$

In Eq. (14), f_t is the tangential traction, $\bar{v}$ the relative velocity between the target and the penetrator, f_n the normal traction at a point on the target/penetrator interface, μ_s and μ_k the static and kinetic coefficients of friction, respectively, and γ describes the dependence of the coefficient of friction upon the relative speed of sliding between the two contacting surfaces.

The aforestated problem requires solving a system of coupled nonlinear partial differential equations. Since it is nearly impossible to solve the problem analytically, we seek its approximate solution by the finite element method and employ a large scale explicit code DYNA2D [17] to do so. It uses 4-noded quadrilateral elements, with one-point integration rule and an hour-glass control to suppress the spurious modes. The time step is adjusted adaptively and equals a fraction of the time taken for an elastic wave to travel through the smallest element in the mesh. As the bodies deform, elements near the target/penetrator interface become distorted severely and the time step size drops drastically. The time step is also affected by the restoring force to be applied to the interpenetrating nodes at the target/penetrator interface. In the symmetric penalty method used to enforce the continuity of velocity components normal to the interface, this force is proportional to the depth of interpenetration, the bulk modulus of the penetrated element, that element's dimensions and a user defined scale factor. Once the time step size has become too small, the deforming region needs to be rezoned for computations to continue at a reasonable pace.

3. Computation and discussion of results

3.1. Results for the Taylor impact test

3.1.1. Results for the Johnson–Cook thermal softening function

We assigned the following values to various material and geometric parameters.

Rod length = 60 mm, Rod diameter = 10 mm, $V_0 = 150$ m/s, $\theta_0 = 293$ K.

Depleted Uranium (DU):

$$\begin{aligned} &A = 1079\ \text{MPa},\quad B = 1120\ \text{MPa},\quad C = 0.007,\quad n = 0.25,\quad m = 1.0,\quad \dot{\epsilon}_0 = 1/\text{s},\\ &\rho = 18\,600\ \text{kg/m}^3,\quad \mu = 58\ \text{GPa},\quad K = 119\ \text{GPa},\quad c = 117\ \text{J/kg°C},\quad \theta_m = 1473\ \text{K}. \end{aligned} \tag{15}$$

Tungsten Heavy Alloy (WHA):

$$\begin{aligned} &A = 1506\ \text{MPa},\quad B = 177\ \text{MPa},\quad C = 0.016,\quad n = 0.12,\quad m = 1.0,\quad \dot{\epsilon}_0 = 1/\text{s},\\ &\rho = 18\,600\ \text{kg/m}^3,\quad \mu = 160\ \text{GPa},\quad K = 328\ \text{GPa},\quad c = 134\ \text{J/kg°C},\quad \theta_m = 1723\ \text{K}. \end{aligned}$$

The values of A, B, C, θ_m, m, $\dot{\epsilon}_0$ and n for both materials are taken from Rajendran's report [5]; those of other material parameters are taken from a handbook. We note that the shear modulus for WHA equals 2.76 times that for DU. Since their mass densities are the same, the speed of the shear wave in WHA will equal 1.66 times that in DU. Fig. 1 depicts the effective stress vs. the effective strain curves for axisymmetric compression of a homogeneous cylinder deformed at a nominal strain-rate of 5000/s. We have also included these curves for the Zhou et al. thermal softening function with $\beta = 2.4$ and $\alpha = 0.2$ and 0.3. It is clear that for both DU and WHA, the Zhou et al. expression exhibits enhanced softening of the material. That is, for same values of ϵ^p and $\dot{\epsilon}^p$, the flow stress is lower with the Zhou et al. softening than that with the Johnson–Cook relation.

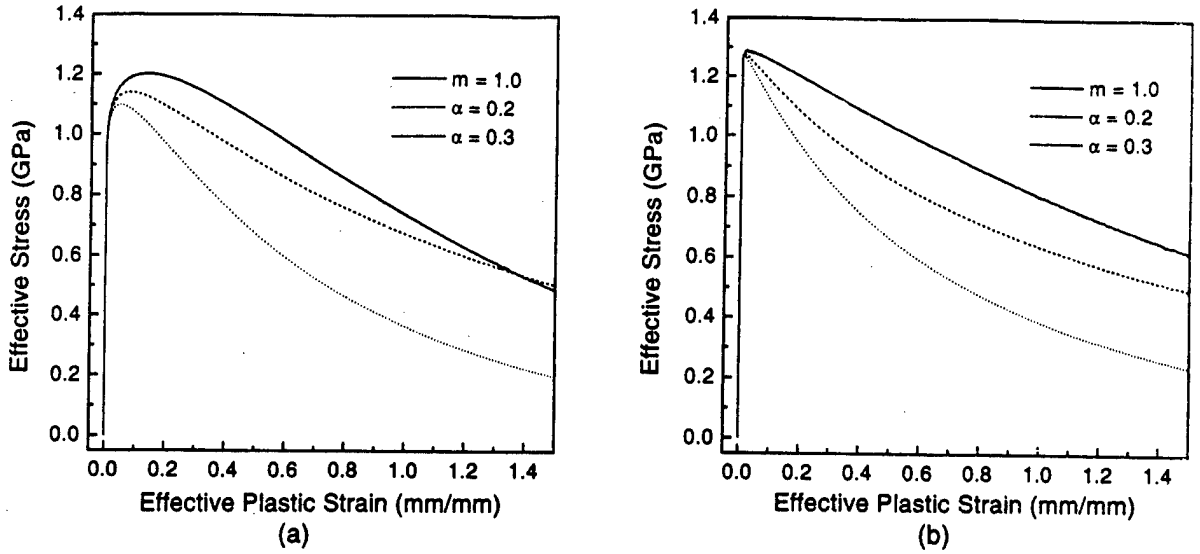

Fig. 1. Effective stress vs. effective strain during axisymmetric compression of homogeneous WHA and DU cylinders deformed at a nonimal strain-rate of 5000/s.

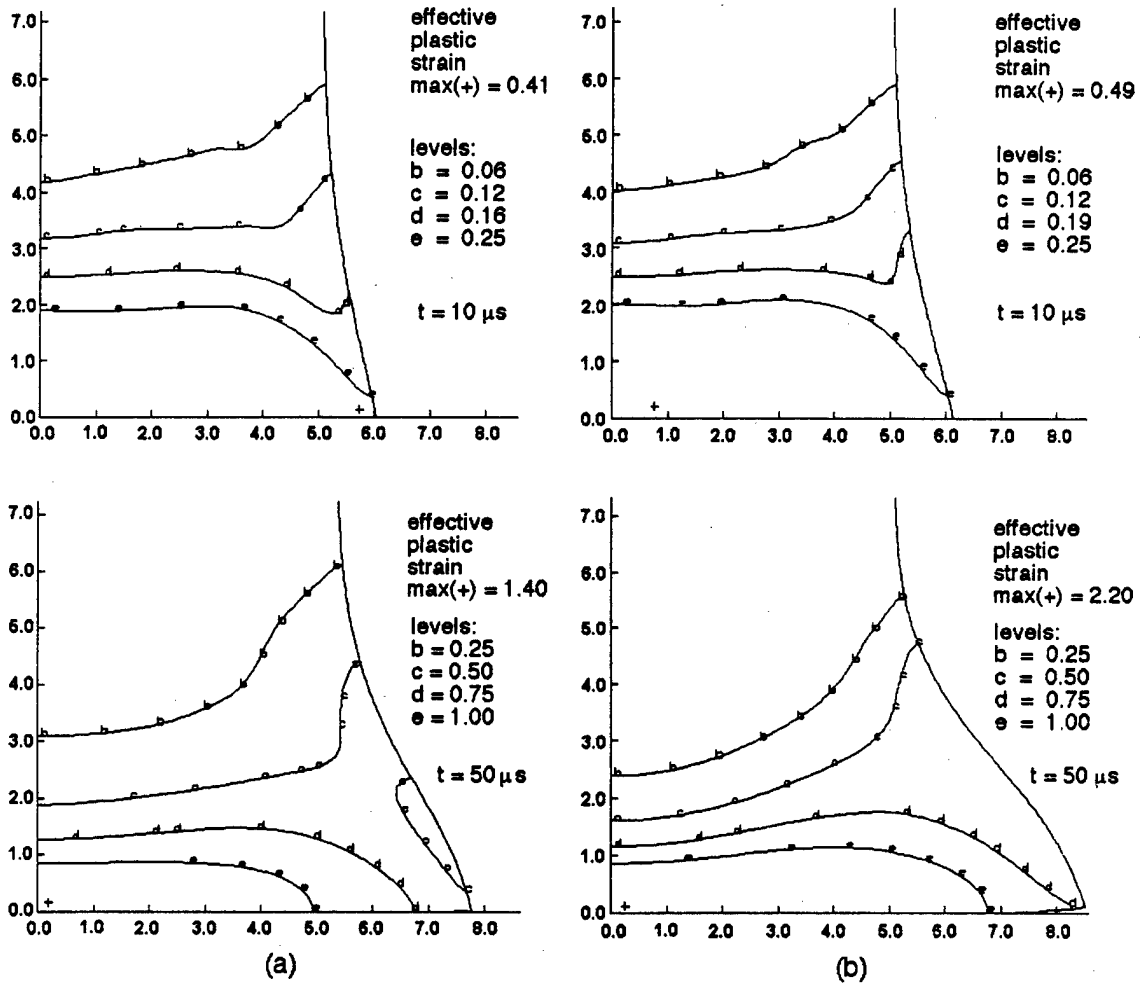

Fig. 2. Contours of the effective plastic strain at $t = 10\,\mu s$ and $t = 50\,\mu s$ in (a) the DU rod; (b) the WHA rod.

The finite element mesh had 40 uniform elements in the radial direction and 250 elements in the axial direction as described below. The rod length was divided into three segments: $0 \leq z \leq 10$ mm, $10 \leq z \leq 25$ mm and $25 \leq z \leq 60$ mm. The first portion was divided into 80 uniform elements and the second and third segments were each divided into 85 nonuniform elements whose height increased as one moved away from the impact face. The mesh is fine near the impact surface and should sufficiently capture the intense deformations of the rod in the mushroomed region. Computed results for a trial problem indicated that the height of the mushroomed region was approximately 5 mm. The contact condition is satisfied by nullifying the axial velocity of nodes about to penetrate the target.

The contours of the effective plastic strain exhibited in Fig. 2 for the DU and WHA rods at $t = 10$ and 50 μs suggest that rod particles outside of the mushroomed region do not undergo much plastic deformation. At $t = 10$ μs the maximum effective plastic strain equals 0.41 and 0.49 in the DU and WHA rods and occurs at a point near the periphery of the impact face in DU but near the centroidal axis in WHA. This point where the maximum effective plastic strain occurs gradually moves towards the stagnation point. At $t = 50$ μs, the maximum effective plastic strain equals 1.4 in DU and 2.2 in WHA and, in each rod, occurs at a point of the impact face that is close to the centroidal axis. The severely deformed region with the effective plastic strain exceeding 1.0 extends, on the impact face to nearly 6.8 mm for the WHA rod and 5.00 mm for the DU rod; its thickness equals approximately 0.8 mm for both materials.

We have plotted in Fig. 3 for the two rods the variation of the effective plastic strain, in their deformed

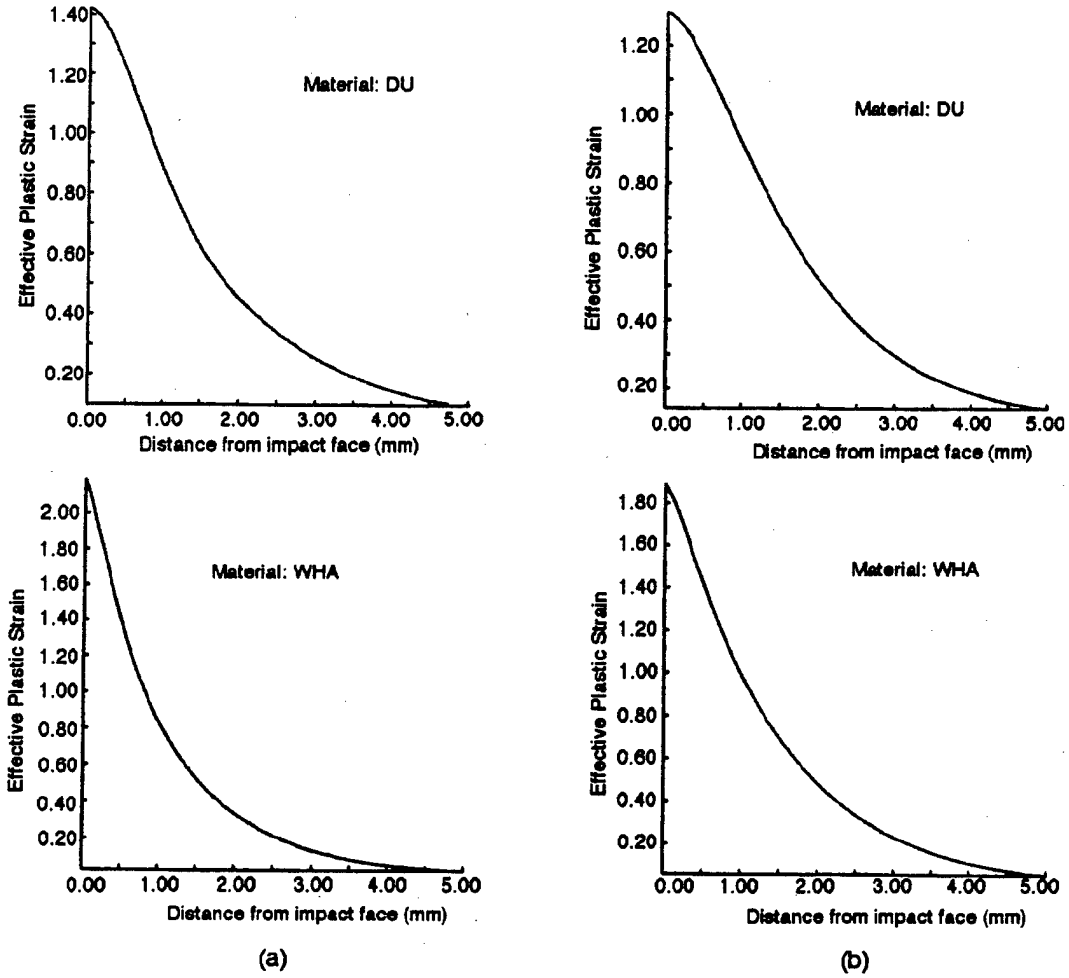

Fig. 3. Distribution of the effective plastic strain at $t = 80$ μs on a verticle line passing through (a) (0.25, 0.0) mm; (b) (2.5, 0.0) mm; (c) (5.0, 0.0) mm.

configurations at $t = 80$ μs, on three vertical lines situated 0.25, 2.5 and 5.00 mm from the centroidal axis. For each rod, the effective plastic strain drops off rapidly on vertical lines through (0.25, 0) mm and (2.5, 0) mm but rather gradually on the line through (5, 0) mm. The peak effective plastic strain at points on these lines equals 1.42, 1.30, 0.98 and 2.20, 1.88, 1.36, respectively, for the DU and WHA rods. The effective plastic strain drops off a little more gradually for the DU rod as compared to that for the WHA rod. These plots suggest that the thickness of the intensely deformed region equals about 0.8 mm which exceeds considerably the usual width of a shear band. It is very likely that a material point near $r = z = 0$ will fail first for each rod at $t < 80$ μs; the ensuing crack will result in traction free surfaces and may significantly affect the solution of the problem for subsequent times. As stated earlier, no such failure criterion is incorporated into our work.

In Fig. 4 we have plotted the time history of the effective plastic strain at several points on the impact face of the DU rod; similar results were obtained for the WHA rod and also for points on the centroidal axial line and the mantle of each rod. It is evident that the effective plastic strain increases monotonically at these points and the material at points close to the centroidal axial line is intensely deformed. The plots of the effective stress vs. effective plastic strain at these points, not included herein, reveal that the effective stress drops essentially monotonically and gradually except when the gap occurs between the impact face and the anvil. At a point near the center of the DU rod, it drops from 1.2 GPa at $t = 10$ μs to 0.45 GPa at $t = 60$ μs and its rate of drop slowly decreases. At numerous points on the impact face, centroidal axial line and the mantle of the rods where we plotted the time histories of the effective plastic strain and the effective stress, we saw neither a catastrophic drop in the effective stress nor a dramatic rise in the rate of growth of the effective plastic strain; these two phenomena were observed at the initiation of a shear band in a thermoviscoplastic body deformed either in simple shear or plane strain compression. This could be due to the different state of stress at a point in the axisymmetric Taylor impact test from that in either simple shear or plane strain compression. Batra and Kim [18] and Deltort [19] have postulated that a shear band initiates at a point when the effective stress there drops to 90% and 80%, respectively, of its peak value. According to this definition, a shear band has initiated in both the DU and WHA rods at a point close to $r = 0$, $z = 0$, and also at several other points. At $t = 80$ μs, the temperature at the point $r = z = 0$ equals 1250 K for both DU and WHA rods.

We also simulated plane strain deformations of DU and WHA blocks striking at normal incidence a flat rigid anvil. For each material, a propensity of thin narrow regions of intense plastic deformation were observed. This

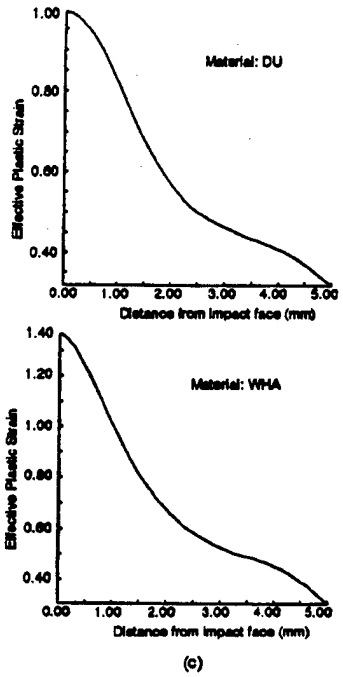

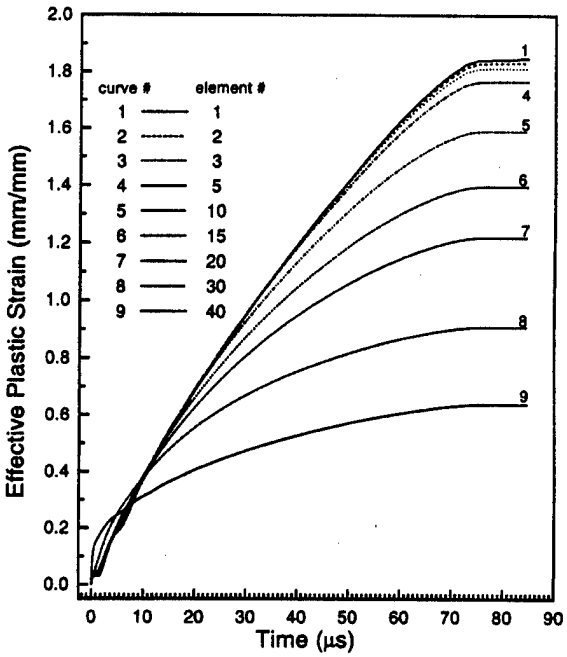

Fig. 3. (continued).

Fig. 4. Time history of the effective plastic strain at the centroids of several elements on a radial line in the impact face of the DU rod; elements are uniform and element 1 abuts the centroidal axis and 40 the mantle of the rod.

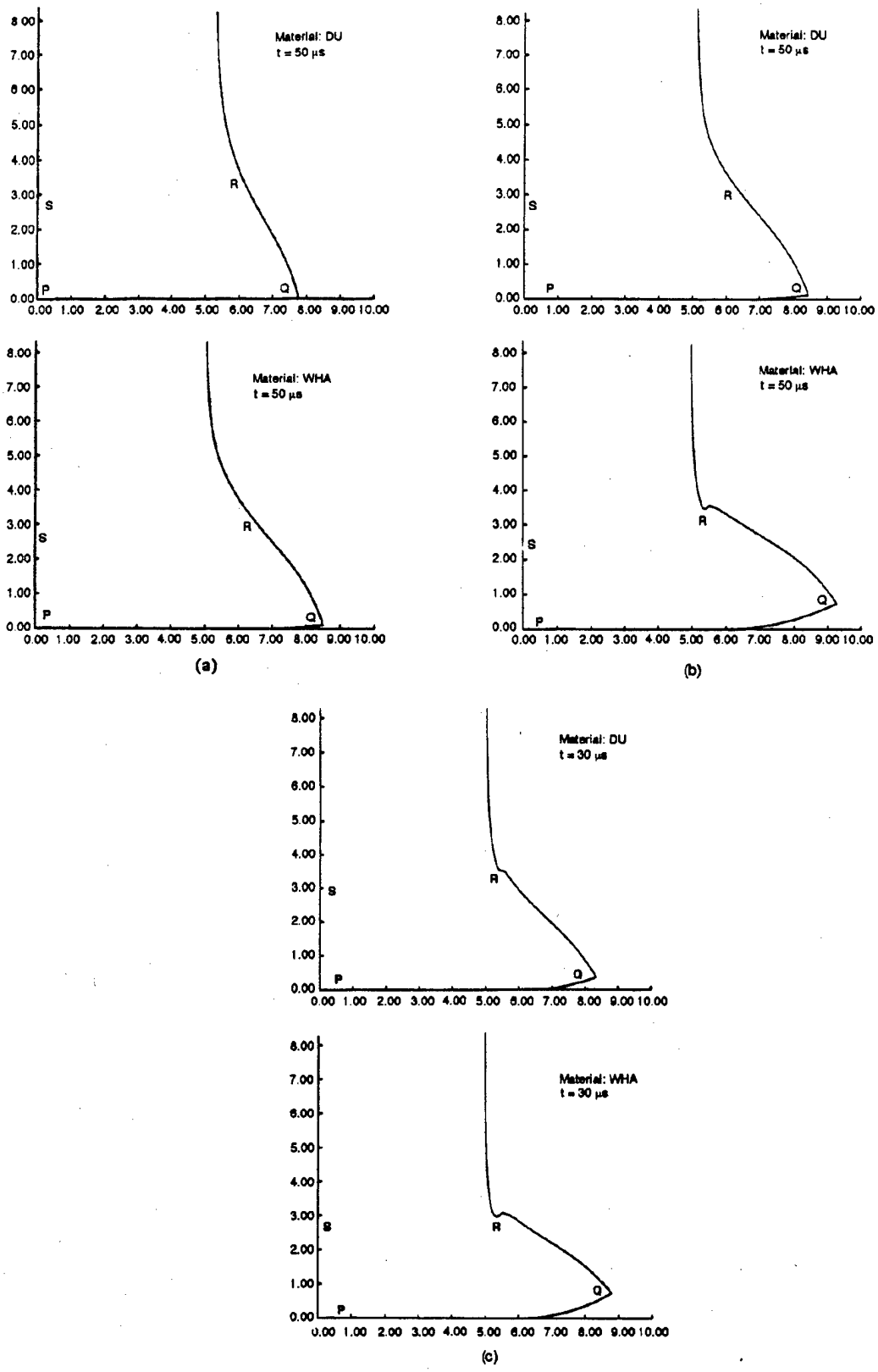

Fig. 5. Deformed shapes of the mushroomed regions for the DU and WHA rods; (a) Johnson–Cook thermal softening, $m = 1.0$; (b) Zhou et al. thermal softening, $\alpha = 0.2$; (c) Zhou et al. thermal softening, $\alpha = 0.3$.

is consistent with the earlier observation [4] that shear bands form more readily in plane strain simulations than axisymmetric ones.

3.1.2. Results for the Zhou et al. thermal softening function

Keeping values of the material and geometric parameters given above, we computed results for the DU and WHA rods with $\beta = 2.4$, $\alpha = 0.2$ and 0.3. Zhou et al. [16] found that $\alpha = 0.2$ and $\beta = 2.4$ provided a good fit to the test data for the WHA they used. Here, we have considered the same values of α for DU because of the lack of data. Thus, the differences, if any, in their deformation patterns will be due to the variation in the values of the shear modulus, bulk modulus, and parameters A, B, C and n in Eq. $(10)_2$. The higher value of α is considered to delineate the effects of enhanced thermal softening.

Figs. 5(a–c) depict the shapes of the mushroomed region for the DU and WHA rods for the three softening functions (Johnson–Cook, Zhou et al. with $\alpha = 0.2$ and 0.3). As expected, the softening function strongly influences the shape of the mushroomed region. In each case, the outer radius of the deformed impacted face is greater in the WHA rod than in the DU rod. For the Johnson–Cook thermal softening, the inflection point in the shape of the mantle is closer to the impacted end for the DU rod as compared to that for the WHA rod. For $\alpha = 0.3$ in the Zhou et al. thermal softening, the curve describing the mantle has a cusp for each material signifying severe deformations there. The height of the mushroomed region is smaller for $\alpha = 0.3$ and it forms sooner in each rod than that for $\alpha = 0.2$. The shapes of the mushroomed regions suggest that severe deformations and hence a shear band may initiate at one or more of the following three locations: adjacent to the stagnation point, near the periphery of the impacted end, and close to the inflection point in the curve describing the mantle of the deformed rod; points selected in these areas for further study of deformations are marked in Fig. 5(a–c) as P, Q and R, respectively. For comparison purposes, we have also investigated histories of various deformation measures at a point close to the centroidal axis and about 2.5 mm above the impact face; this point

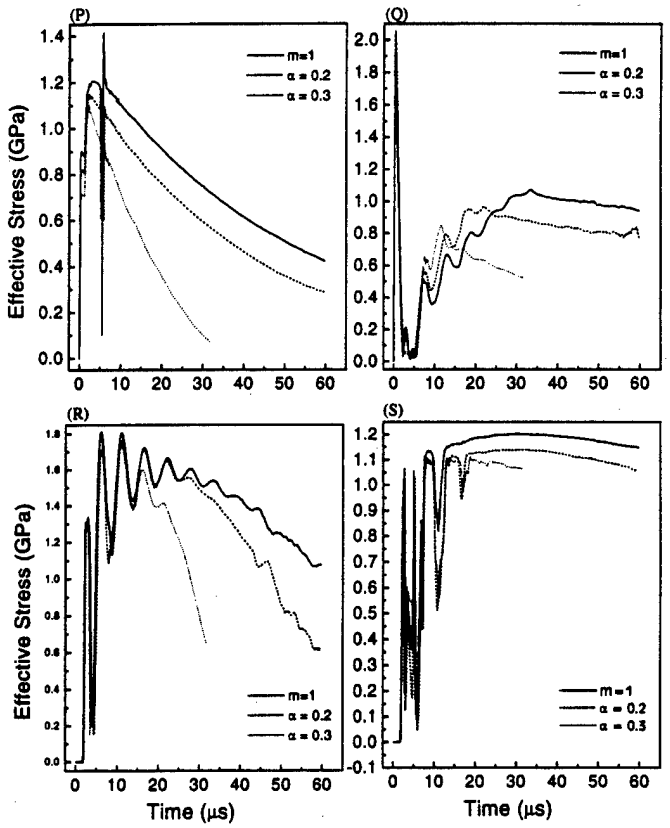

Fig. 6. Time history of the effective stress in elements in the DU rod located at point P, Q, R and S.

is referred to as S. Time histories of the effective plastic strain and the effective stress at these four points for the two rods are plotted in Figs. 6–9. Results for the Johnson–Cook model, discussed in the previous section, are shown for comparison purposes. It is clear that for both DU and WHA rods and the three thermal softening functions considered, the effective plastic strain at point S is much lower than that at the other three points. We recall that during plane strain compression and simple shearing deformations of a thermoviscoplastic block, the initiation of a shear band is indicated by a rapid growth of the effective plastic strain accompanied by a sharp drop in the effective stress. For the DU and WHA rods, these two conditions are fulfilled at points P and R for $\alpha = 0.3$, thus shear bands initiate there and propagate into the mushroomed head of the rod. For $\alpha = 0.2$ and 0.3 the effective plastic strain at each one of the four points considered grows less rapidly in the DU rod than that in the WHA rod. For $\alpha = 0.2$, the aforestated conditions for the initiation of a shear band are satisfied at point R for the WHA rod and the distortions in the deformed mesh confirm a shear band there. However, for the DU rod, even though the effective plastic strain at point R grows rapidly first, its rate of growth tapers off. The deformed meshes shown in Fig. 10 suggest that no shear band initiates from point R in the DU rod with $\alpha = 0.2$ since the mesh is regular in the neighborhood of R. For each thermal softening considered, the mesh around point P is severely deformed. Also, the effective stress there drops to less than 80% of its peak value. Thus, according to the definition of the drop in the effective stress, a shear band initiates at point P for each thermal softening studied. We have plotted, for $\alpha = 0.2$ and 0.3, contours of the effective plastic strain in Fig. 11 for the two rods. It is clear that for both values of α a shear band has developed near the cusp in the mantle for the WHA rod but only for $\alpha = 0.3$ in the DU rod. We recall that Dick et al. [13] observed a shear band passing through the transition region in their reverse ballistic tests on the WHA rod, and a sharp cusp developed where the band intersected the mantle. The mesh used herein is not fine enough to capture the dimensions of this cusp or of the band. Fig. 12 illustrates for $\alpha = 0.3$ the distribution of the effective plastic strain on lines nearly perpendicular to the shear band; the lines were determined visually. These plots show that the bands are narrower for the WHA rod than those for the DU rod.

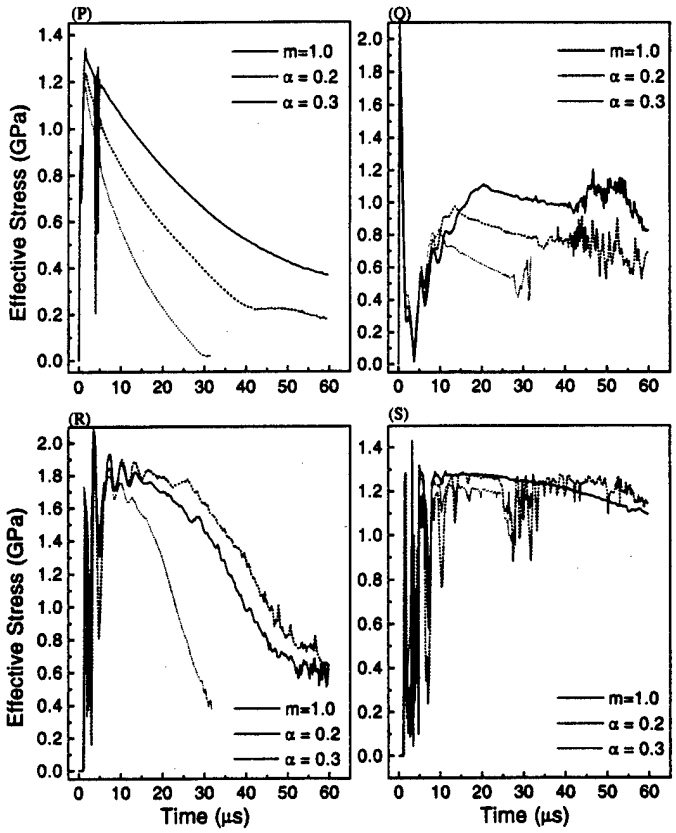

Fig. 7. Time history of the effective stress in elements in the WHA rod located at points P, Q, R and S.

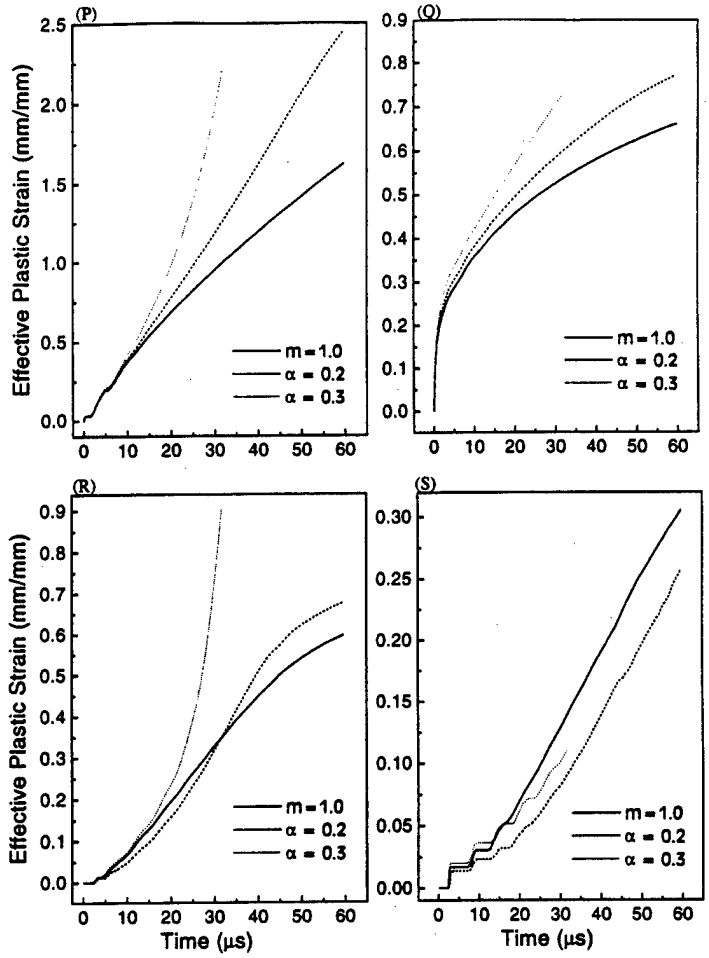

Fig. 8. Time history of the effective plastic strain in elements in the DU rod located at points *P*, *Q*, *R* and *S*.

3.2. Results for the penetration problem

We have analysed the normal impact of 7.69-mm diameter and 76.9-mm long DU and WHA rods moving at 843 m/s on a 60-mm diameter and 70-mm deep steel target. Each material was modeled by the Johnson–Cook relation and for the steel we took

$$A = 792.2\ \text{MPa},\quad B = 509.5\ \text{MPa},\quad C = 0.014,\quad n = 0.26,\quad m = 1.03,\quad T_m = 1793\ \text{K},$$

$$\rho = 7840\ \text{kg/m}^3,\quad c = 477\ \text{J/kg°C},\quad \mu = 76\ \text{GPa},\quad K = 147\ \text{GPa}$$

Parameters in the friction law (14) at the target/penetrator interface were assigned the following values.

$$\mu_s = 0.78,\qquad \mu_k = 0.06,\qquad \gamma = 0.0055$$

The penetrator region was divided into uniform 0.16 mm × 0.171 mm elements near the impact face with properly graded larger elements away from it. The mesh in the target region was also graded with 0.16 mm × 0.171 mm elements in the region adjoining the impact face and larger elements elsewhere; Fig. 21 of Stevens's thesis [20] depicts the finite element discretization of the region adjoining the target/penetrator interface. We used the automatic contact option for the first 18.5 μs for DU and 15 μs for WHA penetrator. Subsequently, the noninterpenetration conditions were satisfied by using the slideline type 4 (kinetic with sliding, separation and friction).

Figs. 13 and 14 depict at $t = 10$ and 20 μs fringes of the effective plastic strain in the deformed region

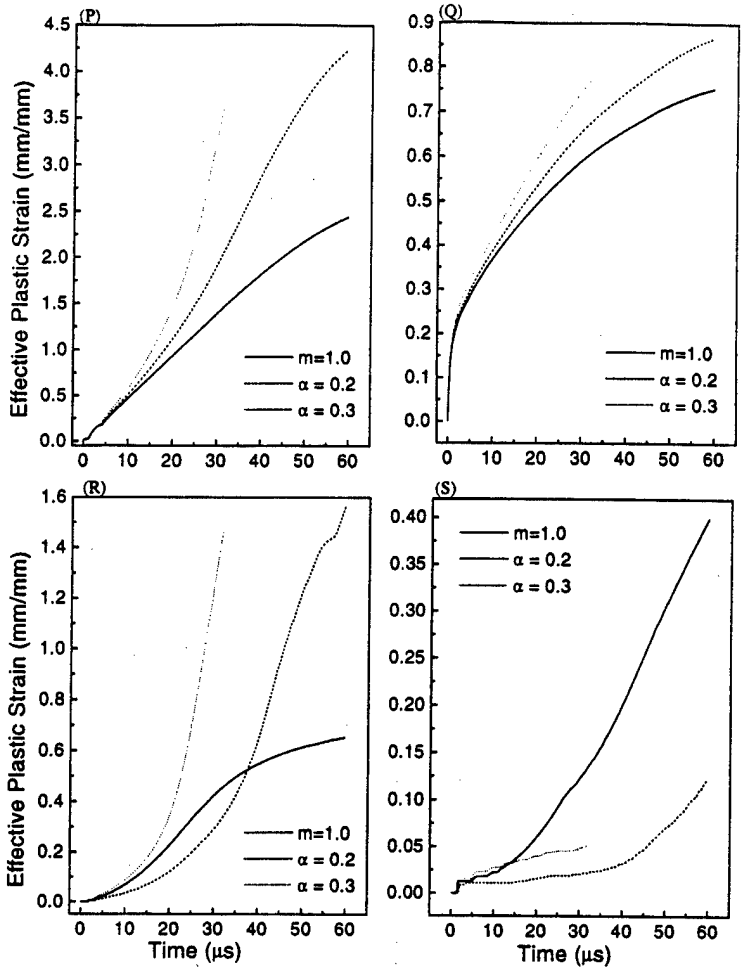

Fig. 9. Time history of effective plastic strain in elements in the WHA rod located at points *P*, *Q*, *R* and *S*.

adjoining the target/penetrator interface. Similar plots and a movie (available at the URL www.sv.vt.edu/research/batra-stevens/pent.html) showing the distribution of the effective plastic strain in the deformed regions indicate that a propensity of narrow regions of intense plastic deformation form in the DU penetrator in the region abutting the target/penetrator interface and also in the ejecta where the penetrator particles turn to flow backwards. Fewer of these narrow regions occur in the WHA rod and they are smeared out resulting in a rather uniformly deformed zone of intense plastic deformation. Also, the ejecta consists of intensely deformed material, separated by shear banded material for the DU rod but continuously deformed material for the WHA rod. The deformed meshes indicated the occurrence of narrow severely deformed regions in the DU penetrator passing through the points where the flow reverses but none in the WHA penetrator. The deforming region was remeshed at $t = 14$ μs and subsequently at every instant when the time step required to integrate the governing equations decreased to one-hundredth of the starting value, or when the mesh distorted so severely as to cause kinks in the boundary. Every attempt was made to remesh identically the deforming penetrator and target regions in the two cases. Fig. 25 of Stevens's thesis [20] shows the remeshed region at $t = 20$ μs for the DU penetrator and the steel target. The fluid-like material at the head of the ejecta had to be removed in order for the computations to continue at a reasonable pace; such deletions were kept to a minimum and no fluid-like material was removed till $t = 15$ μs. Values of velocities, mass density, temperature and other variables at the newly created nodes were computed from the previous solution so that the total linear momentum and energy were conserved. Such mappings smoothen out the fields and may retard the growth of shear bands.

Fig. 15 illustrates the deformed mesh at $t = 22.5$ μs for the DU penetrator in the region where the flow is

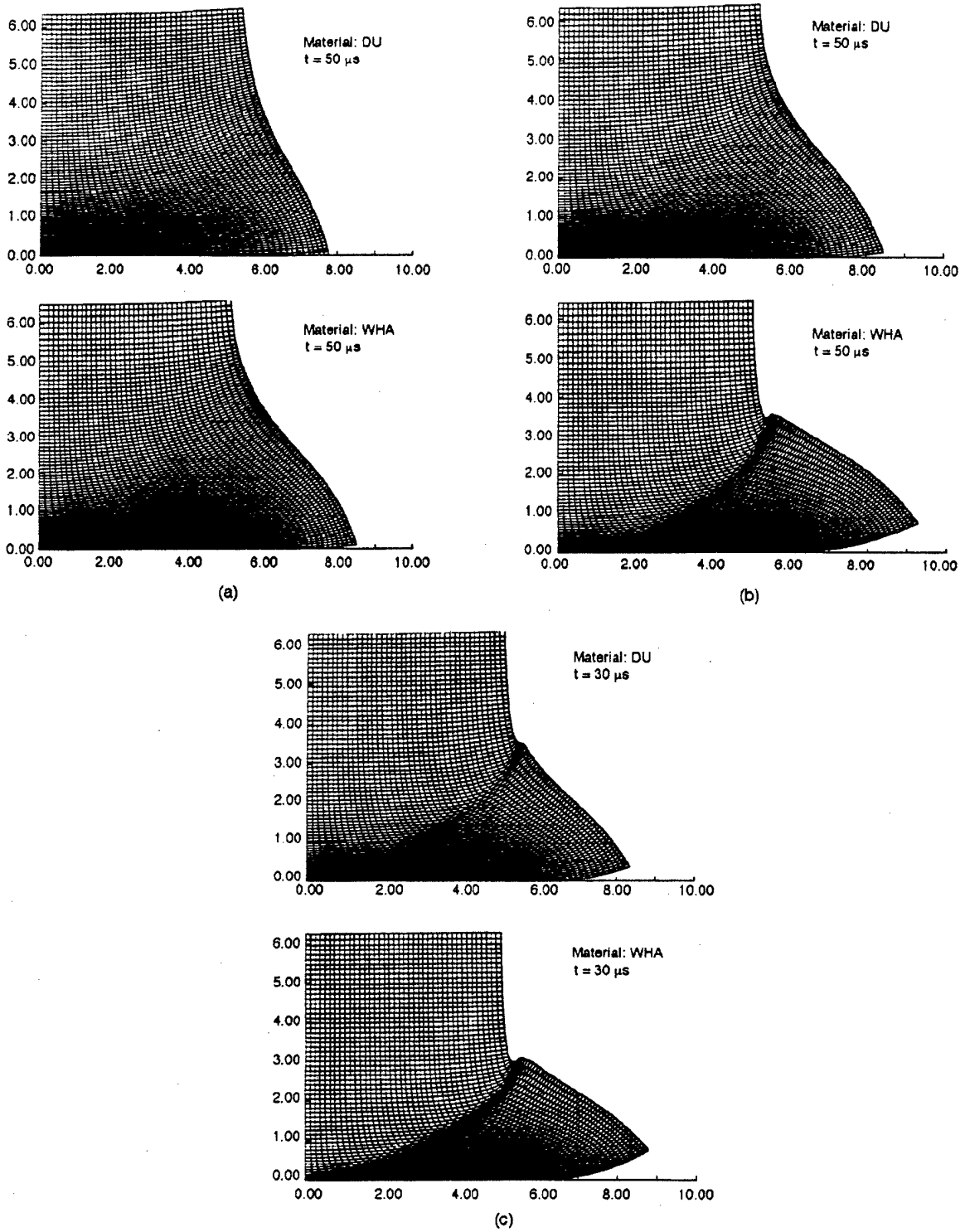

Fig. 10. Deformed meshes near the impacted ends of the DU and WHA rods; (a) Johnson–Cook thermal softening, $m = 1.0$; (b) the Zhou et al. thermal softening, $\alpha = 0.2$; (c) the Zhou et al. thermal softening, $\alpha = 0.3$.

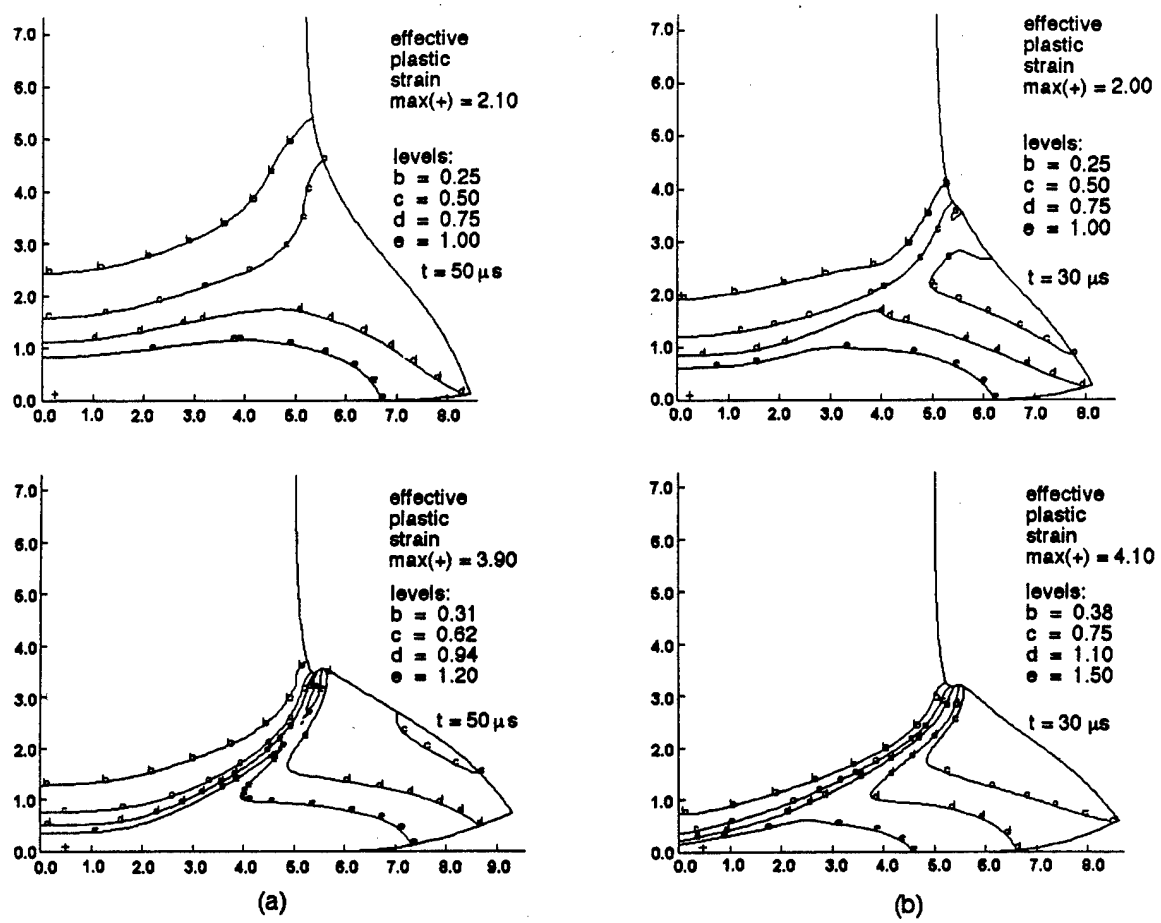

Fig. 11. Contours of the effective plastic strain in the deformed DU and WHA rods using the Zhou et al. thermal softening function with (a) $\alpha = 0.2$, at time, $t = 50$ μs and (b) $\alpha = 0.3$, at time, $t = 32$ μs.

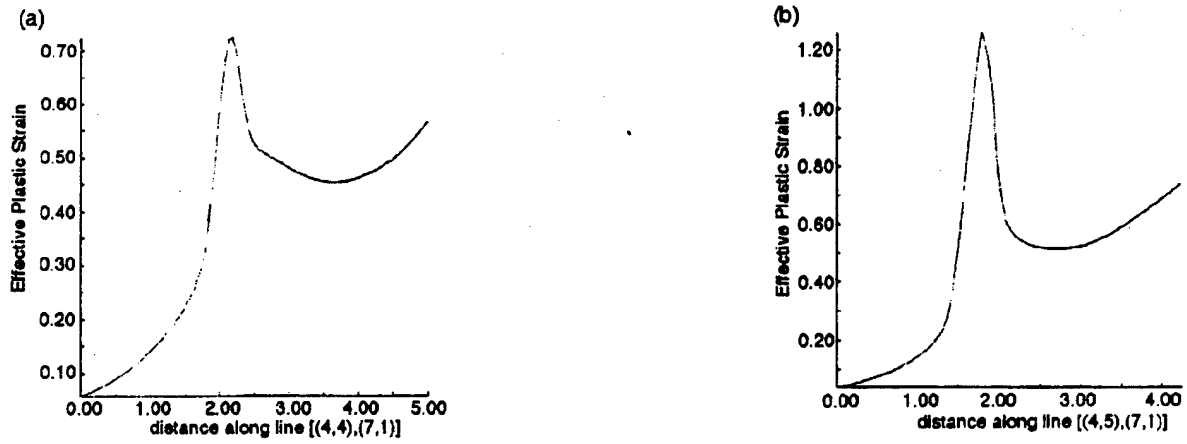

Fig. 12. Distribution of the effective plastic strain on a line approximately perpendicular to the shear band formed near the mantle of (a) the DU rod; (b) the WHA rod using the Zhou et al. thermal softening with $\alpha = 0.3$.

turning around, and in Fig. 16 we have plotted the distribution of the effective plastic strain on line AB shown in Fig. 15. It is clear that three shear bands have formed on this line. The deformed mesh for the WHA penetrator at $t = 22.5$ μs is illustrated in Fig. 17; it does not exhibit any narrow intensely deformed regions. For each

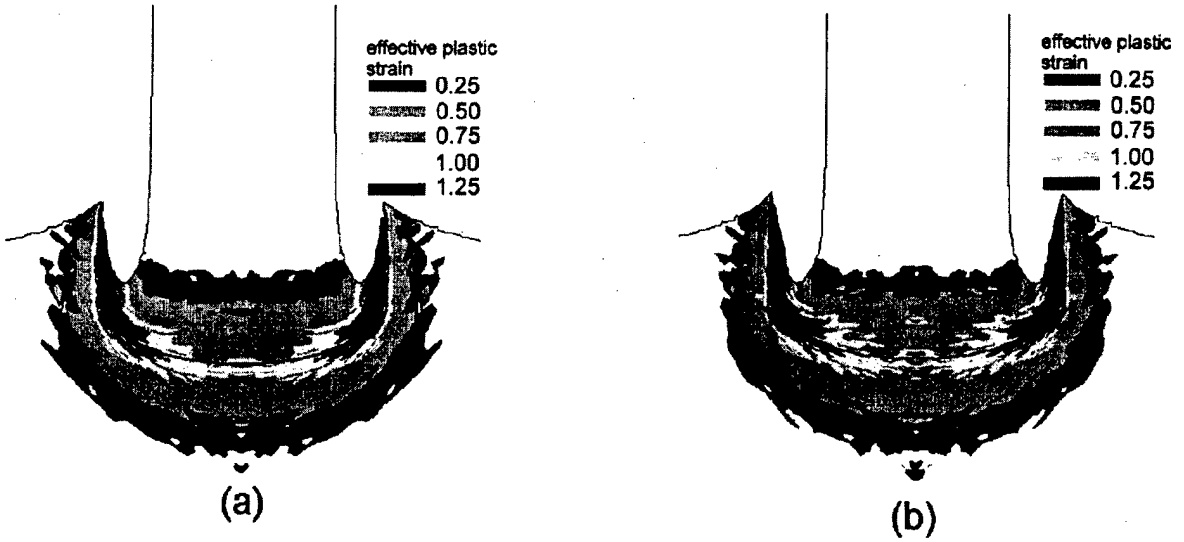

Fig. 13. Fringes of effective plastic strain at time, $t = 10\ \mu s$ for (a) DU; (b) WHA penetrator.

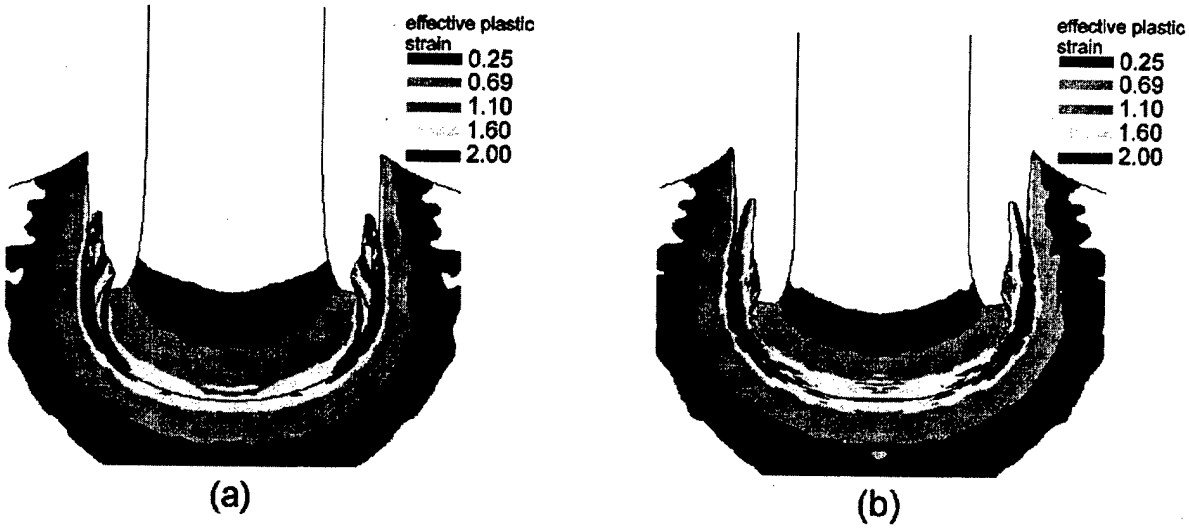

Fig. 14. Fringes of effective plastic strain at time, $t = 20\ \mu s$ for (a) DU, (b) WHA penetrator.

penetrator, the effective stress within a thin layer adjoining the target/penetrator interface is reduced to almost zero at $t = 30\ \mu s$ indicating that the material has essentially lost its strength and behaves like an ideal compressible fluid. The time step has now become too small to continue the computations at a desirable pace.

The time histories of the axial velocity of the tail end of the two penetrators and also of the axial point on the penetrator/target interface were very close to each other (cf. Fig. 28 of [20]). This suggests that differences in the occurrence of shear bands in the ejectas of the two penetrators cannot be discerned by examining either the penetration speed or the speed of the tail end of the rod.

The time histories of the effective plastic strain, effective stress, the temperature and the stress-strain curve for a penetrator particle initially located near the stagnation point are exhibited in Fig. 18. Even though the effective plastic strain has nearly the same value for the DU and WHA rods, the temperature rise is more for the DU because of its greater strain hardening. The initial rate of drop of the effective stress is same for the two materials, and the effective stress begins to drop a little earlier for the WHA. This suggests that during the early stages of impact, the WHA particle shear bands sooner than the corresponding DU particle; a trend consistent

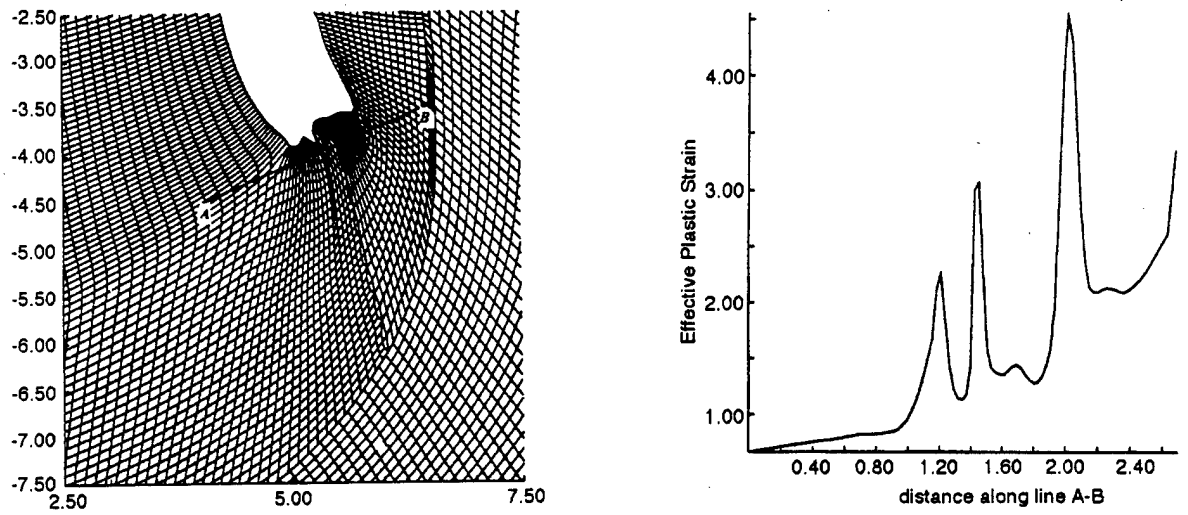

Fig. 15. Deformed mesh of the ejecta of the DU rod at $t = 22.5$ μs, and the location of line AB on which the effective plastic strain is plotted in Fig. 16.

Fig. 16. Distribution of the effective plastic strain on line AB shown in Fig. 15.

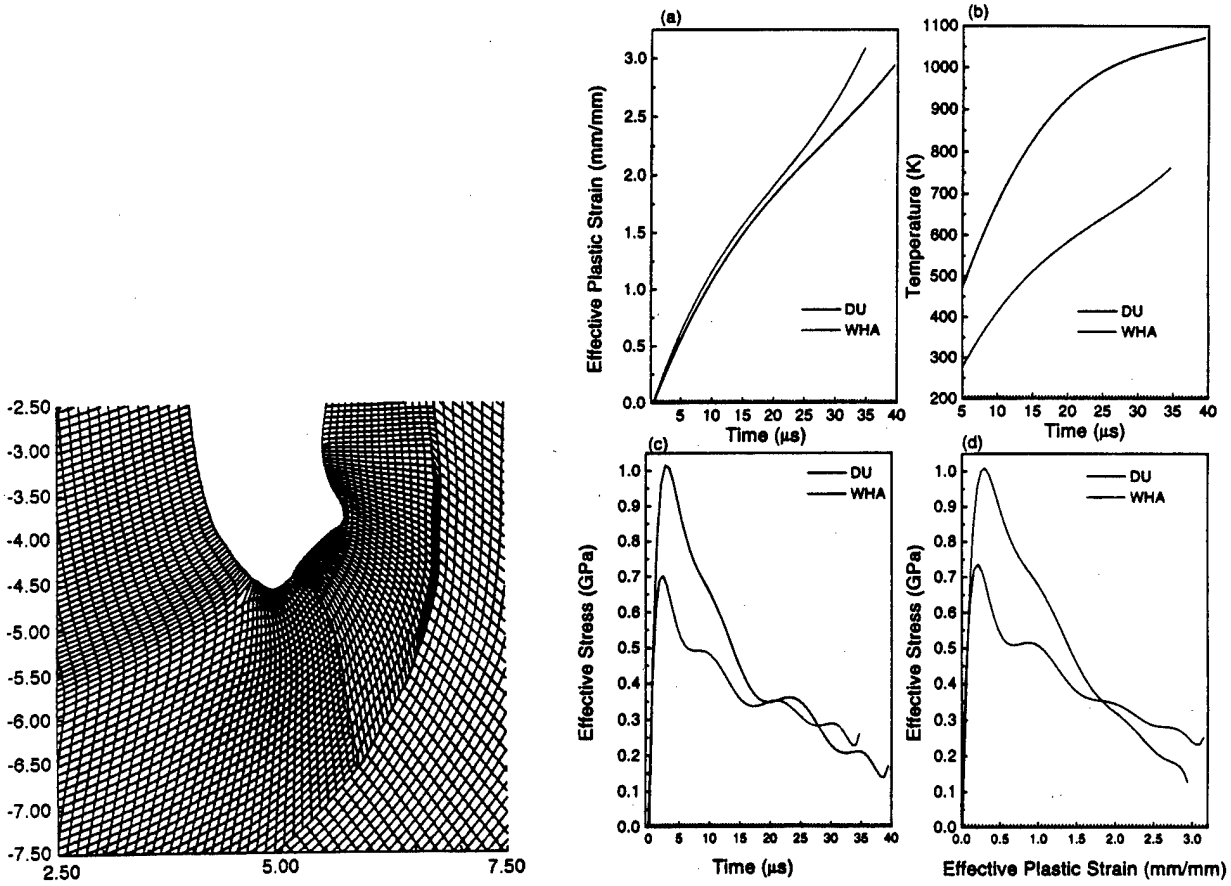

Fig. 17. Deformed mesh of the ejecta of the WHA rod at $t = 22.5$ μs.

Fig. 18. (a)–(c) Time history, for an element near the stagnation point, of the effective plastic strain, temperature and effective stress; (d) effective stress vs. effective plastic strain for the element.

with that observed in simulations of simple shear, plane strain compression and the Taylor impact test. However, as the ejecta grows, the deformation gradients in the WHA penetrator get smeared out while the DU ejecta experiences periodic localizations.

4. Conclusions

We have analysed the localization of deformation in cylindrical DU and WHA rods impacting at normal incidence either a flat rigid target or a thick steel target. The thermal softening in DU and WHA is modeled by either the Johnson–Cook relation or that proposed by Zhou et al. For the Johnson–Cook relation, the Taylor impact simulations yield no clear localization in either the DU or WHA rods. However, if one adopts the criterion that a shear band initiates when the effective stress has dropped to 80% or 90% of its peak value, then a shear band initiates at several points on and near the impact face of each rod. These bands do not propagate far into the rod. For the Zhou et al. thermal softening, shear bands form in both DU and WHA rods when $\alpha = 0.3$, but only in the WHA rod when $\alpha = 0.2$. The shear band initiates on the mantle near the point of transition between the mushroomed region and the relatively undeformed rod, and a cusp forms there. These features qualitatively match with those observed by Dick et al. in their reverse ballistic tests on WHA rods.

The Johnson–Cook relation was used to model the axisymmetric, elastic, thermoviscoplastic deformations of the penetrator and the target. These simulations show that during the early stages of penetration, as in the Taylor impact test, shear bands form more readily in WHA than they do in DU. However, as the deformed penetrator material turns around and forms the ejecta, the WHA rod is relatively uniformly deformed, while the deformations periodically localize into narrow bands in the DU ejecta. The development of shear bands during the early stages of penetration was also influenced by the method used to enforce the noninterpenetration of one material into the other across the target/penetrator interface. We recall that no failure or fracture criterion was included in our work.

These studies illustrate the need for more realistic values of material parameters for simulating dynamic deformations of DU and WHA rods.

Acknowledgments

This work was supported by the U.S. Army Research Office grants DAAH04-95-1-0042 and DAAH04-95-1-0043 to Virginia Polytechnic Institute and State University with Dr. K. Iyer as the program manager, and the NSF grant CMS-9411383.

References

[1] L.S. Magness and T. Farrand, Deformation behavior and its relationship to the penetration performance of high-density KE penetrator materials, Proc. Army Science Conf., West Point, NY, 1990.

[2] R.C. Batra, X.T. Zhang and T.W. Wright, Critical strain ranking of twelve materials in deformations involving adiabatic shear bands, J. Appl. Mech. 62 (1995) 252–255.

[3] R.C. Batra and Z. Peng, Development of shear bands in dynamic plane strain compression of depleted uranium and tungsten blocks, Int. J. Impact Engrg. 16 (1995) 375–395.

[4] R.C. Batra and K.I. Ko, Analysis of shear bands in dynamic axisymmetric compression of a thermoviscoplastic cylinder, Int. J. Engrg. Sci. 31 (1993) 529–547.

[5] A.M. Rajendran, High strain rate behavior of metals, ceramics and concrete, Report #WL-TR-92-4006, Wright Patterson Air Force Base, 1992.

[6] G.I. Taylor, The use of flat-ended projectiles for determining dynamic yield stress 1. Theoretical considerations, Proc. Roy. Soc. A194 (1948) 289–299.

[7] S.E. Jones, P.P. Gillis, J.C. Foster, Jr. and L.L. Wilson, A one-dimensional, two-phase flow model for Taylor impact specimens, J. Engrg. Mat. Tech. 113 (1991) 228.

[8] S.E. Jones, P.J. Maudlin, P.P. Gillis and J.C. Foster, Jr., Material behavior during early time plastic deformation in the Taylor impact test, Computers in Engineering, Vol. 2 (ASME Press, New York, 1992) 173–179.

[9] W. Johnson, Impact Strength of Materials (Arnold, London, 1972) 229–247.
[10] I.M. Hutchings, The behaviour of metals under ballistic impact at sub-ordnance velocities, in: J. Mescall and V. Weiss, eds., Materials Behaviour Under High Stress and Ultrahigh Loading Rates, 29th Sagamore Army Materials Research Conference (Plenum, New York and London, 1983) 161–196.
[11] R.P. Papirno, J.F. Mescall and A.M. Hansen, Beyond the Taylor test to fracture, in: Proc. of the Army Symp. on Solid Mechanics, 1980—Designing for Extreme Environments, Loading and Structural Behaviour, Army Materials and Mechanics Research Center, Watertown, MA (1980) 367–385.
[12] M.L. Wilkins and M.W. Guinan, Impact of cylinders on a rigid boundary, J. Appl. Phys. 44 (1973) 1200–1213.
[13] R.D. Dick, V. Ramachandran, J.D. Willians, R.W. Armstrong, W.H. Holt and W. Mock, Jr., Dynamic deformation of W7Ni3Fe alloy via reverse-ballistic impact, in: A. Crowson and E.S. Chen, eds., Tungsten and Tungsten Alloys—Recent Advances (The Minerals, Metals & Materials Society, 1991) 269–276.
[14] C.A. Truesdell and W. Noll, The nonlinear field theories of mechanics, in: S. Flügge, ed.: Handbuch der Physik, Vol. III/s (Springer-Verlag, Berlin, 1965).
[15] G.R. Johnson and W.H. Cook, A constitutive model and data for metals subjected to large strains, high strain rate, and high temperatures, Proc. 7th Int. Symp. Ballistics, The Hague, The Netherlands (1983) 541–548.
[16] M. Zhou, A. Needleman and R.J. Clifton, Finite element simulations of plate impact, J. Mech. Phys. Solids 42 (1994) 423–458.
[17] R.G. Whirley, B.E. Engelmann and J.O. Hallquist, DYNA2D, A nonlinear, explicit, two-dimensional finite element code for solid mechanics, User Manual, Lawrence Livermore National Laboratory Report, UCRL-MA-110630, 1992.
[18] R.C. Batra and C.H. Kim, Analysis of shear bands in twelve materials, Int. J. Plasticity 8 (1992) 75–89.
[19] B. Deltort, Experimental and numerical aspects of adiabatic shear in a 4340 steel, J. de Physique, Colloque C8 4 (1994) 447–452.
[20] J.B. Stevens, Finite element analysis of adiabatic shear banding in impact and penetration problems, M.S. Thesis, Virginia Polytechnic Institute and State University, Blacksburg, 1996.

TO PUBLISHER

mailed 12/12/97

INTP 202p

Pergamon

International Journal of Plasticity, Vol. 00, No. 0, pp. 000–000, 1998
© 1998 Elsevier Science Ltd
Printed in Great Britain. All rights reserved
0749-6419/98 $19.00 + 0.00

PII: S0749-6419(97)00039-9

ADIABATIC SHEAR BANDS IN PLANE STRAIN DEFORMATIONS OF A WHA

R. C. Batra* and N. M. Wilson

Department of Engineering Science and Mechanics, Virginia Polytechnic Institute and State University, Blacksburg, VA 24061-0219, U.S.A.

(*Received in final revised form* 6 *September* 1996)

Abstract—We study plane strain thermomechanical deformations of a prismatic body with a rectangular cross-section and made of a tungsten heavy alloy (WHA). Tungsten and iron–nickel–tungsten (Fe–Ni–W) particles are modeled as thermally softening but strain and strain rate hardening. The deformations are assumed to be locally adiabatic and the effect of inertia forces is considered. The body is loaded by applying a normal component of velocity to the opposite edges; the speed increases from zero to the final value in 5 microseconds and is then kept steady there so that the maximum average strain rate is 5000 s^{-1}. Different volume percentages of Fe–Ni–W particles are taken to be randomly distributed in the cross-section. It is found that the time history of the compressive load required to deform the body is initially unaffected by the volume percentage of Fe–Ni–W particles. At an average strain of 0.10 these load histories begin to differ somewhat; at any given value of the nominal strain, the decrease in the magnitude of the load is not a monotonic function of the increase in the volume percentage of Fe–Ni–W particles. For a fixed volume percentage of Fe–Ni–W particles, different random distributions result in essentially the same load history but give different patterns of shear bands. For eight randomly distributed Fe–Ni–W particles clustered around the horizontal centroid axis, none of the shear bands passed through any one of these particles. © 1998 Elsevier Science Ltd. All rights reserved

I. INTRODUCTION

A tungsten heavy alloy (WHA) usually consists of 93% by weight tungsten particles interspread in a matrix of iron–nickel or other materials. For its application as an anti-armor material it is desirable to have as much tungsten, because of its high mass density, as possible. It is believed that the penetration performance of a WHA will be enhanced if adiabatic shear bands form in it continuously and the material fails along these bands (Magness and Farrand (1990)). An adiabatic shear band is a narrow region of intense plastic deformation that usually forms during high strain rate deformation of most metals and many polymers. A shear band is generally followed by a crack, and is an important failure mechanism in ductile materials. It is called adiabatic since there is not enough time for the heat to be conducted out of the hot and severely deformed region. The reader is referred to the book by Bai and Dodd (1992), a special issue of *Applied Mechanics Reviews* edited by Zbib *et al.* (1992), an issue of *Mechanics of Materials* edited by Armstrong *et al.* (1994), and the volume edited by Batra and Zbib (1994) for references on the subject.

*Corresponding author.

A penetration problem in general will involve three-dimensional deformations of the WHA; here we study, for simplicity, its plane strain deformations. The WHA is usually made by sintering and tungsten particles are interspread in the matrix phase. We assume that matrix particles are randomly distributed among the tungsten particles, the two sets of particles deform coherently in the sense that surface tractions and displacements among adjoining particles are the same. Thus no separation across the interface between two different material phases is allowed. The deformations are assumed to be locally adiabatic; this assumption appears reasonable because of the short times, of the order of a few microseconds, involved for the development of a shear band. Batra and Kim (1991), through numerical experiments, have shown that the effect of thermal conductivity on the time of initiation of a shear band is negligible; however, the post localization behavior is noticeably affected by heat conduction.

We investigate the effect of the volume of iron–nickel–tungsten (Fe–Ni–W) particles dispersed randomly among the tungsten particles and consider cases when the former equals 10, 8, 6, 4, 2, 0.2, 0.1, 0.02 and 0.01% of the total volume. For each one of the first five cases, seven different random distributions of Fe–Ni–W particles are analysed with the objectives of finding statistically the average strain at the initiation of a shear band and the standard deviation in this value. The computed results reveal that the initial distribution of Fe–Ni–W particles, provided it exceeds 0.1%, has a negligible effect on the time-history of the compressive load required to deform the body till the time a shear band initiates and also on the instant when a shear band initiates. For the present problem, it is not easy to decipher when a shear band initiates since it is difficult to formulate an objective criterion. The load required to deform the body drops noticeably much after (about 2 or 3 microseconds out of a total of 30 microseconds) the mesh has severely deformed; the mesh begins to deform intensely before that time. However, the number of bands, their locations and the general pattern of the deformed mesh depend upon the volume percentage and the distribution of Fe–Ni–W particles. Shear bands also form in pure tungsten and the load history in this case is quite different from that when there are Fe–Ni–W particles distributed randomly in tungsten particles. After one or more shear bands have developed in the block, dead zones with essentially zero strain rates and separated by these bands develop. We note that Batra and Peng (1995) studied a similar problem for tungsten and uranium blocks and also computed these dead zones. They considered a block of a homogenized tungsten alloy with 0.1, 0.2 and 0.3% randomly distributed defects, modeled as either very soft, very hard or 5% weak particles and employed the Johnson–Cook (1983) relation to simulate the thermoviscoplastic response of the material. Here we employ a similar constitutive relation except that the thermal softening is modeled by a power-law type function Zhou (1993) obtained by fitting a curve through the experimental data. We consider a two phase mixture with each constituent assigned material properties obtained from test data. Thus the speeds of elastic and plastic waves are different in the two constituents. We add that there is no failure or fracture criterion included in this work; thus each constituent can undergo unlimited amount of plastic deformations until it melts. A melted particle is modeled as a compressible ideal fluid. However, in our simulations, no material particle melted.

II. FORMULATION OF THE PROBLEM

We use rectangular Cartesian co-ordinates, with origin at the centroid of the rectangular 1 cm×2 cm block (cf. Fig. 1), to analyse plane strain, locally adiabatic,

thermomechanical deformations of a WHA consisting of tungsten and Fe–Ni–W particles. It is assumed that Fe–Ni–W particles are randomly distributed in the quarter cross-section lying in the first quadrant, they are situated symmetrically with respect to the horizontal and vertical centroidal axes in other quadrants, and during the deformation process, surface tractions and displacements at the interfaces between different particles are continuous. We use the referential or Lagrangian description of motion and refer the reader to Truesdell and Noll (1965) for equations expressing the balance of mass, linear momentum, moment of momentum and internal energy. We assume that the moment of momentum is identically satisfied and all of the plastic working rather than 90 to 95% of it as asserted by Taylor and Farren (1925) and Sulijoadikusumo and Dillon (1979) is converted into heating.

We assume that each material is isotropic, elastic-viscoplastic and obeys von Mises yield criterion with isotropic hardening; the radius of the yield surface at a material point increases with an increase in the effective plastic strain and effective plastic strain-rate and decreases with a rise in the temperature there. The flow stress, σ_y, at a material point is assumed to be given by

$$\sigma_y = (A + B(\varepsilon_p)^n)(1 + C\ln(\dot{\varepsilon}_p/\dot{\varepsilon}_0))\left(1 - \beta\left(\left(\frac{T}{T_0}\right)^m - 1\right)\right). \tag{1}$$

Here $A, B, n, C, \dot{\varepsilon}_0, \beta$ and m, are material parameters, T_0 is the room temperature in degrees Kelvin, ε_p is the effective plastic strain, $\dot{\varepsilon}_p$ is time rate of change of ε_p and T is the present temperature in degrees Kelvin of the material particle. Equation (1) differs from the Johnson–Cook (1983) relation only in the dependence of the flow stress upon the temperature rise. Bell (1968) concluded from tests done in his laboratory that, for several metals, the yield stress is an affine function of the temperature rise. Zhou (1993) obtained

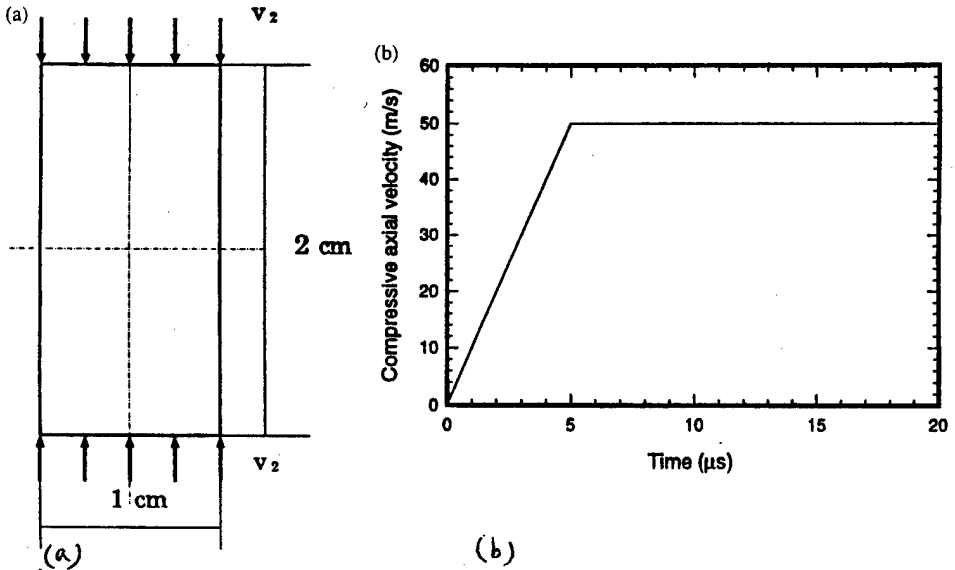

Fig. 1. A schematic sketch of the problem studied, and the time history of the vertical component of velocity prescribed on the top and bottom edges.

the temperature dependence indicated in eqn (1) by fitting a smooth curve to the experimental data for the Fe–Ni–W phase, and the homogenized WHA. In the absence of any test data for tungsten particles, he postulated a similar expression for tungsten and gave for it values of β and m. These and values of A, B, n, C and $\dot{\varepsilon}_0$ obtained by fitting curves to the data points computed from the relations given by Zhou (1993) for tungsten and Fe–Ni–W particles are listed below.

Tungsten:

$$\rho = 19300\,\text{kg m}^{-3},\quad G = 155\,\text{GPa},\quad A = 730\,\text{MPa},\quad B = 562\,\text{MPa},$$
$$n = 0.0751,\quad C = 0.02878,\quad \dot{\varepsilon}_0 = 1.355 \times 10^{-7}\,\text{s}^{-1},\quad c = 138\,\text{J kg}^{-1}\,^{\circ}\text{C}^{-1} \tag{2}$$
$$m = 0.15,\quad \beta = 2.4,\quad T_0 = 293\,\text{K}$$

Fe–Ni–W:

$$\rho = 9200\,\text{kg m}^{-3},\quad G = 98.84\,\text{GPa},\quad A = 150\,\text{MPa},\quad B = 546\,\text{MPa},$$
$$n = 0.208,\quad C = 0.0838,\quad \dot{\varepsilon}_0 = 6.67 \times 10^{-7}\,\text{s}^{-1},\quad c = 382\,\text{J kg}^{-1}\,^{\circ}\text{C}^{-1}, \tag{3}$$
$$m = 0.20,\quad \beta = 2.4,\quad T_0 = 293\,\text{K}.$$

Here ρ is the mass density, G the shear modulus, and c the specific heat of the material. We assume that the volumetric response of the material is elastic with the hydrostatic pressure p, taken to be positive in compression, is related to the specific volume change by

$$p = K(\rho/\rho_o - 1) \tag{4}$$

where ρ_0 equals the mass density in the reference configuration, $K = 317.45\,\text{GPa}$ for tungsten and 202.4 GPa for Fe–Ni–W particles. For the present problem, plastic deformations are expected to be dominant. Since plastic deformations are assumed to be independent of the hydrostatic pressure, the precise form of the equation of state will have a negligible effect on the time of initiation of a shear band. This was confirmed by running a few cases with the Mie–Gruniesen equation of state. The two sets of results differed only slightly in the magnitude of the compressive load required to deform the block, but the pattern of shear bands and their time of initiation remained unchanged. Results presented herein are for the polynomial equation of state (4).

We note that the values of material parameters given in (2) and (3) may not be valid at strains, strain-rates and temperatures likely to occur in a shear band even though Zhou (1993) used these to analyse a shear band problem. Klepaczko *et al.* (1987) have stated that most of these material parameters should be taken to depend upon the temperature. In the absence of any test data available to find their temperature dependence, we regard them as constants.

We assume that the block is initially at rest, is stress free and is at a uniform temperature T_0. We take all bounding surfaces of the block to be thermally insulated; the vertical edges of the block to be traction free; the top and bottom horizontal edges to be free of tangential tractions and with a vertical component of velocity prescribed on them. The magnitude of this prescribed velocity increases from zero to $50\,\text{m s}^{-1}$ in $5\,\mu\text{s}$ and then stays fixed at $50\,\text{m s}^{-1}$ (cf. Fig. 1(b)); thus, the nominal strain-rate increases from 0 to $5000\,\text{s}^{-1}$ in $5\,\mu\text{s}$ and then stays fixed at $5000\,\text{s}^{-1}$.

Because of the symmetry of the specimen, and initial and boundary conditions about the horizontal and vertical centroidal axes, we assume that thermomechanical deformations of the block are symmetrical about these two axes and analyse deformations of the material in the first quadrant. Thus conditions arising from the symmetry of deformations, i.e. zero tangential tractions, vanishing normal component of velocity, and zero heat flux are prescribed on these edges.

III. COMPUTATION AND DISCUSSION OF RESULTS

The coupled thermomechanical problem formulated above is highly nonlinear and can not be solved analytically, therefore, we seek its approximate solution by the finite element method by using the explicit large scale finite element code DYNA2D developed by Whirley *et al.* (1992). The material subroutine in the code for the Johnson–Cook model was modified to incorporate the thermal softening function included in eqn (1). The code uses 4-noded isoparametric quadrilateral elements with one-point integration rule and an hour-glass control algorithm to suppress the spurious modes. The time step is adjusted adaptively to satisfy the Courant condition after each time increment. For the two phase material being studied here, the speed of the expansion (volumetric) wave equals 4.06 mm μs^{-1} in W and 4.69 mm μs^{-1} in Fe–Ni–W. Since the volumetric wave travels faster than the shear wave, the time step size is set equal to a fraction of the time taken for the volumetric wave to travel through the smallest Fe–Ni–W element in the mesh. The initial mesh consists of 10^4 uniform rectangular elements with 100 elements in each direction. However, Fe–Ni–W particles are expected to deform more severely, because of their low yield stress, than pure tungsten particles and will control the time step size. The computed results show that this is not necessarily the case.

Figure 2 depicts, in the reference configuration, three random distributions of 200 Fe–Ni–W particles; the larger rectangles depict two abutting Fe–Ni–W particles. As mentioned earlier, for a fixed number of Fe–Ni–W particles, seven different random distributions, generated by using different seed numbers, were considered. However, the computed time histories of the compressive load were essentially similar for the seven cases. In order to save space, the time histories of the compressive load for 1 cm thick block and for three random distributions of 200 Fe–Ni–W particles are illustrated in Fig. 3. It is clear that, in the beginning, different distributions of 200 Fe–Ni–W particles have a minimal effect on the load required to deform the block. For average axial strains exceeding 0.1, one starts to see differences in the load mainly because around this time the deformation begins to localize. Since the load has been obtained by integrating normal tractions on the top surface, and the integration has a smoothening effect, essentially identical load distributions may give quite different deformation patterns as evinced by the deformed meshes plotted in Fig. 4. Even though almost four dominant narrow regions of intense plastic deformation stand out clearly, there are several thin regions of large plastic deformation. Similar deformation patterns were obtained for other random distributions of 200 Fe–Ni–W particles and also for 10, 20, 400, 600, 800 and 1000 Fe–Ni–W particles. Once the elements have distorted severely, the deforming region needs to be rezoned to obtain satisfactory results. This was not done and it explains why the load histories for the composite block are plotted only upto an average axial strain of 0.15. A comparison of deformed meshes of Fig. 4 with that shown in Fig. 5(b) of Batra and Peng (1995) suggests that the different thermal softening function in eqn (1) and the substitution of weak elements by Fe–Ni–W

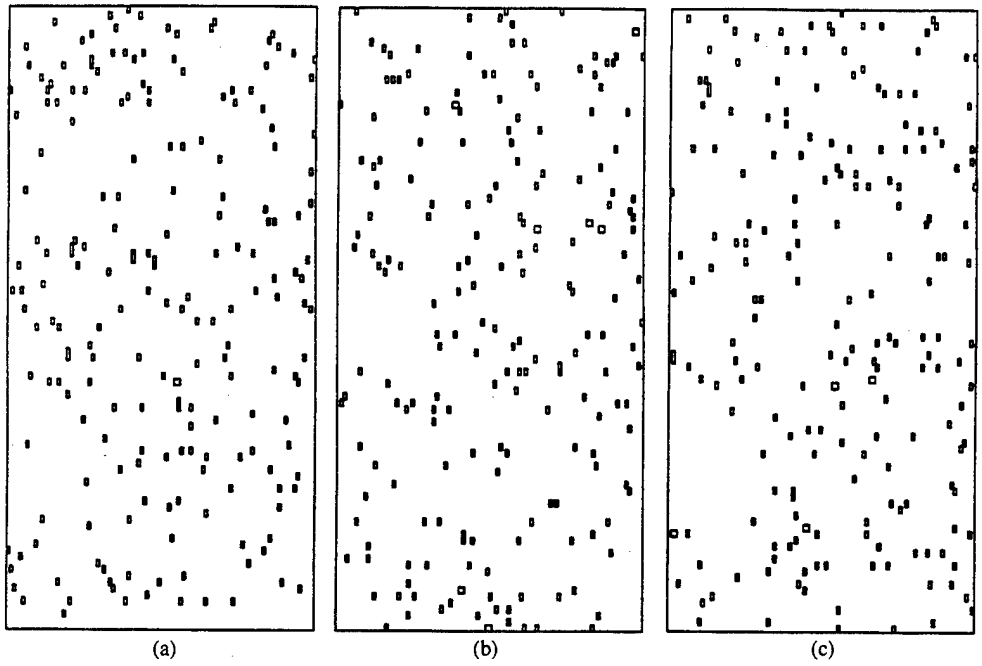

Fig. 2. Three random distributions of 200 Fe–Ni–W particles among 10 000 particles of the WHA.

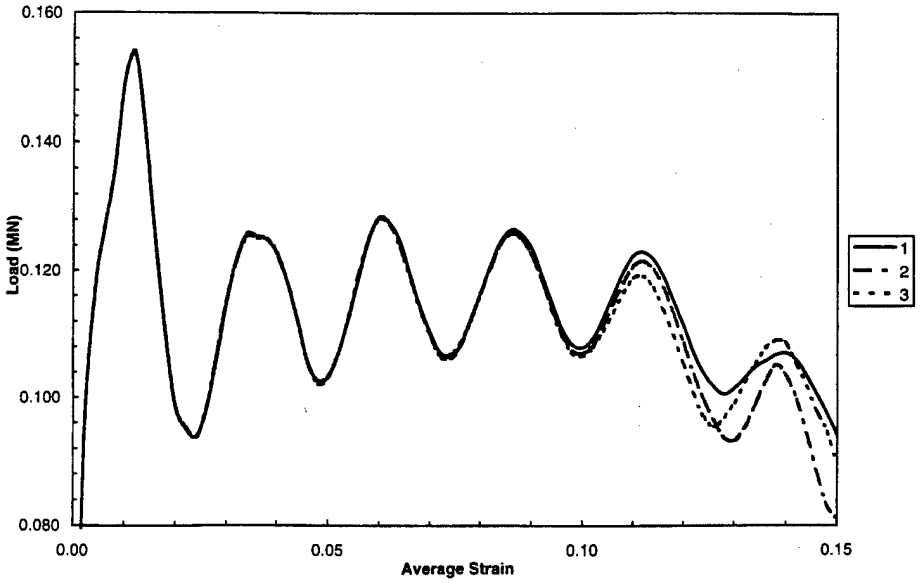

Fig. 3. Time histories of the compressive load (shown positive) required to deform the block for the three random distributions shown in Fig. 2.

particles have no effect on the general orientation of the localized regions of intense plastic deformation or shear bands. Batra and Peng (1995) pointed out that the shear modulus affects this orientation. We note that, except for the two differences mentioned above, the problem studied by Batra and Peng (1995) is identical to the present one. They seemed to believe that a shear band, as indicated by the deformed mesh, formed at an average axial strain of 0.2. They did not study details of the deformation within the localized region; we discuss these below. Because of the different elastic moduli and mass densities of tungsten and Fe–Ni–W particles, the coherence conditions require that both elastic and plastic waves be scattered from Fe–Ni–W particles; no such scattering of elastic waves occurs from the weak elements considered by Batra and Peng.

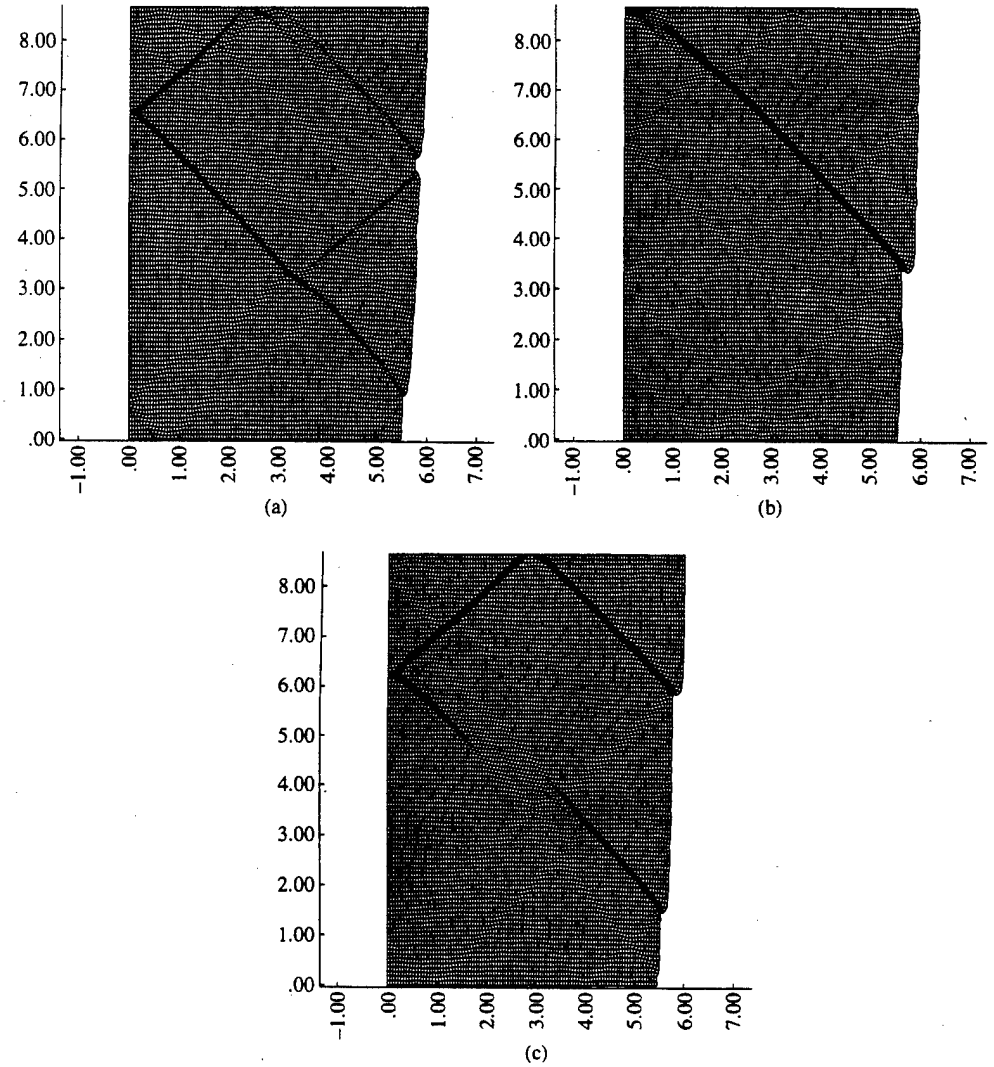

Fig. 4. Deformed meshes at an average axial strain of 0.1375 for the three random distributions shown in Fig. 2.

For the one-dimensional simple shearing problem Wright and Walter (1987) pointed out that the shear stress within the band drops catastrophically; this was confirmed experimentally by Marchand and Duffy (1988) in torsional deformations of a thin-walled tube. Batra and Zhang (1994) analysed torsional deformations of a thin-walled tube as a three-dimensional problem by using DYNA3D and the Johnson–Cook material model and found that the torque required to twist the tube began to drop rapidly essentially at the same time as the shear band, evidenced by severe distortions of the mesh, initiated. The sudden drop in the torque was clearly demarcated by a sharp change in the slope of the torque versus average shear strain curve. Partly because of the oscillations in the load-average strain curve, it is hard to delineate precisely when the load begins to drop rapidly; these oscillations result from the interaction of waves reflected from the boundaries. For the present problem the time when a shear band initiates cannot be objectively defined either from the load versus average strain curve or from the deformed meshes.

From the deformed meshes shown in Fig. 4 it is hard to ascertain if all of the elements within the severely deformed region are equally deformed. Figure 5 depicts, for five different values of the average strain, the distribution of the effective plastic strain at points on the line joining $A(0.4725, 0.4350)$ and $B(0.2275, 0.7450)$ in the reference configuration. These points were identified visually from the deformed mesh to lie within the severely deformed region. During the deformations of the block the orientation of the line changes from an initial value of $-51.7°$ to $-46.2°$ at an average axial strain of 0.135 when a narrow region of intense plastic strain has developed (cf. Fig. 6). We add that the line AB may pass through different material particles at various times. For the plane strain compression problem being studied here the maximum shear stress should occur in the current configuration on a plane inclined at $\pm 45°$ direction to the horizontal axis. One possible reason for the slight deviation of the angle of line AB from this value is that the cross-section is not necessarily rectangular due to the nonhomogeneous deformations of the composite body. The line passed through only one Fe–Ni–W particle for each one of the

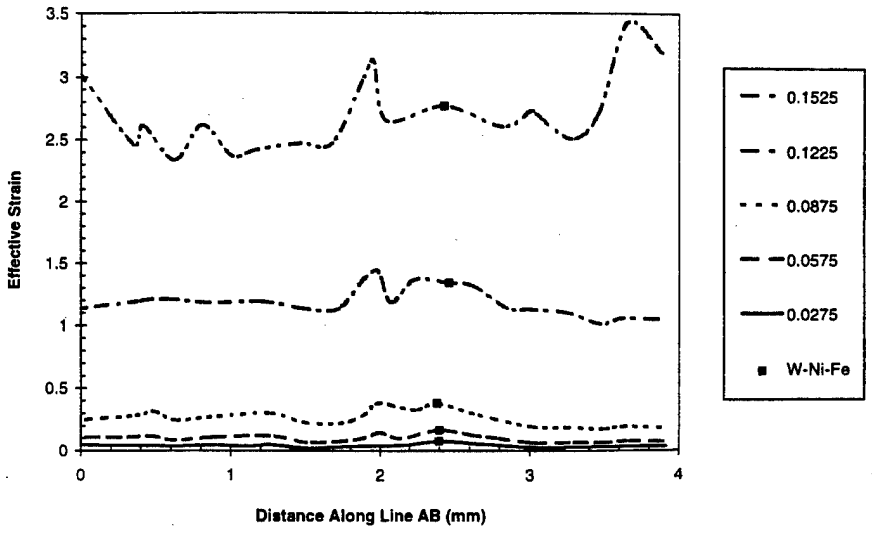

Fig. 5. Distribution, for five different values of the average axial strain, of the effective plastic strain at points on line AB lying within the severely deformed region.

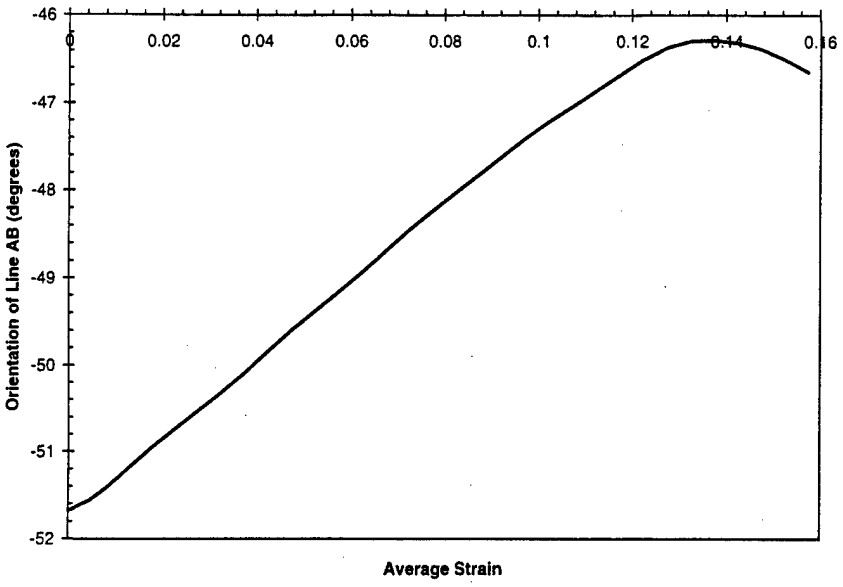

Fig. 6. Orientation of line AB versus the average axial strain.

five values of time considered; the location of this point is marked by a dark square on Fig. 5. If a shear band is taken to have fully developed when the effective plastic strain in it equals at least 1.1, then a shear band forms at an average strain of 0.1225. It is clear that the time of formation of a shear band depends upon its definition. The distribution of the effective plastic strain at points on line AB vividly illustrates that all of these points are not equally deformed. Also the plastic strain at any one point is not significantly higher than that at other points on the line; interestingly enough, a tungsten particle has the largest value of the effective plastic strain. Thus one can not determine whether a shear band initiates at one point first and then propagates in either direction along line AB or several shear bands initiate more or less simultaneously at numerous points and then merge together. In order to shed some light on this we have plotted in Fig. 7(a) the time history of the effective stress at points A, B and an arbitrarily chosen point E(0.3375, 0.6050) on line AB; the effective stress versus effective strain curves for these points are given in Fig. 7(b). Since the effective stress after having attained its peak value drops rather gradually in time (cf. Fig. 7(a)), we adopt the criterion proposed by Batra and Kim (1992) that a shear band initiates in earnest when the effective stress has dropped to 90% of its peak value. Deltort (1994) has postulated that the severe localization of deformation occurs when the shear stress in a simple shearing problem has dropped to 80% of its maximum value. In torsional experiments Marchand and Duffy (1988) associated the initiation of a shear band with the instant where the shear stress begins to drop sharply. According to Batra and Kim's criterion a shear band initiates at point B first and propagates to points E and A; its average speed from B to E equals $802\,\mathrm{m\,s^{-1}}$ and that from E to A $1938\,\mathrm{m\,s^{-1}}$. In general, it is nearly impossible to determine *a priori*, except possibly when there are one or two relatively strong defects present in the body, where a shear band will initiate first. Batra (1996) has reviewed some of the known results for the shear band speed. Depending upon the definition of a shear band and its direction of propagation, the speed in 4340

steel can vary from 60 m s^{-1} to 600 m s^{-1}. For example, during the torsional deformations of a thick-walled 4340 steel tube, a shear band, defined as the region wherein the effective plastic strain exceeds 0.7, propagates in the circumferential direction at about 600 m s^{-1} but at only 60 m s^{-1} in the radial direction.

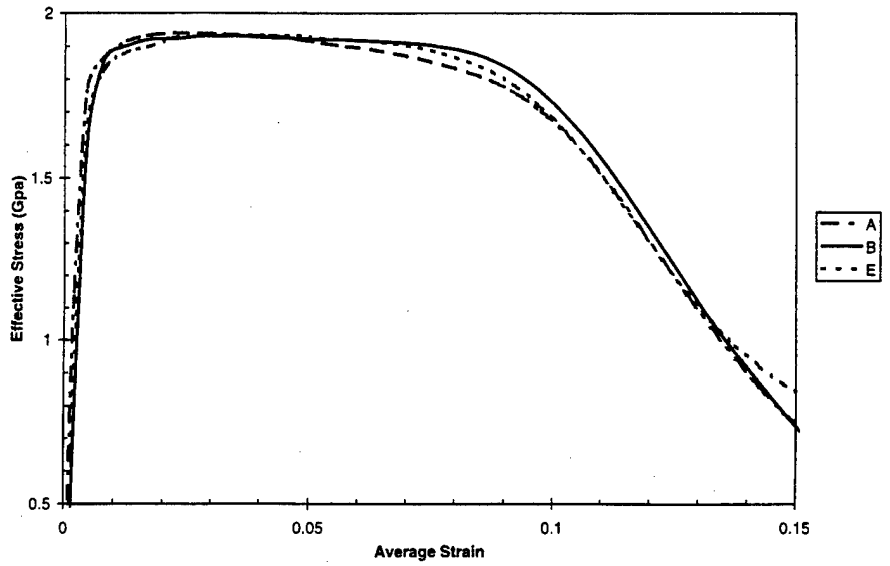

(a)

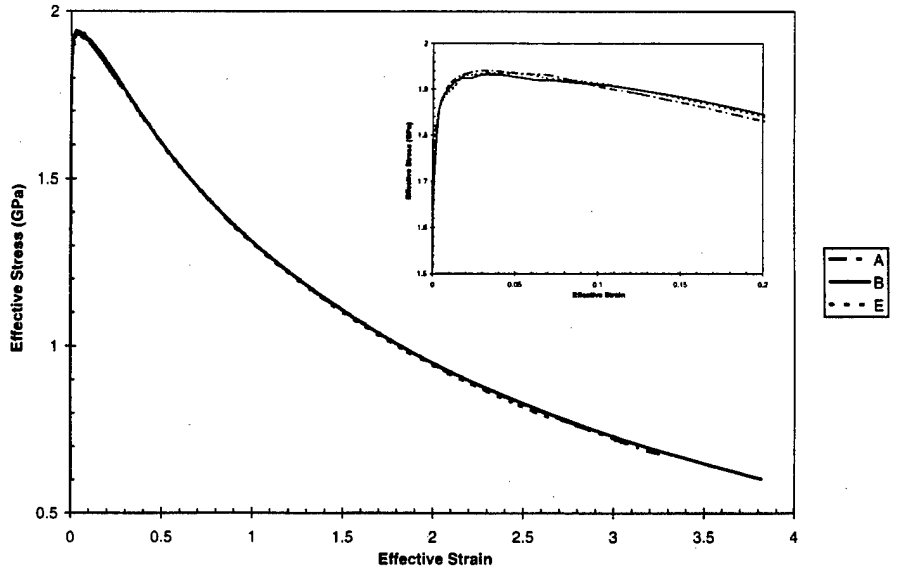

(b)

Fig. 7. (a) Time history of the effective stress at points A(0.4725, 0.4350), B(0.2275, 0.7450) and an arbitrarily chosen point E(0.3375, 0.6050) on line AB. (b) Effective stress versus effective strain curves at points A, B and E.

Figure 8(a) and (b) illustrate the distribution of the effective plastic strain and the nondimensional temperature, T/T_0, at points on line CD perpendicular to the instantaneous position of AB and passing through the arbitrarily chosen point E; co-ordinates of points C and D in the reference configuration are (0.1592, 4.500) and (0.5336, 0.7600) respectively. For the three values of the average strain considered, no Fe–Ni–W particle

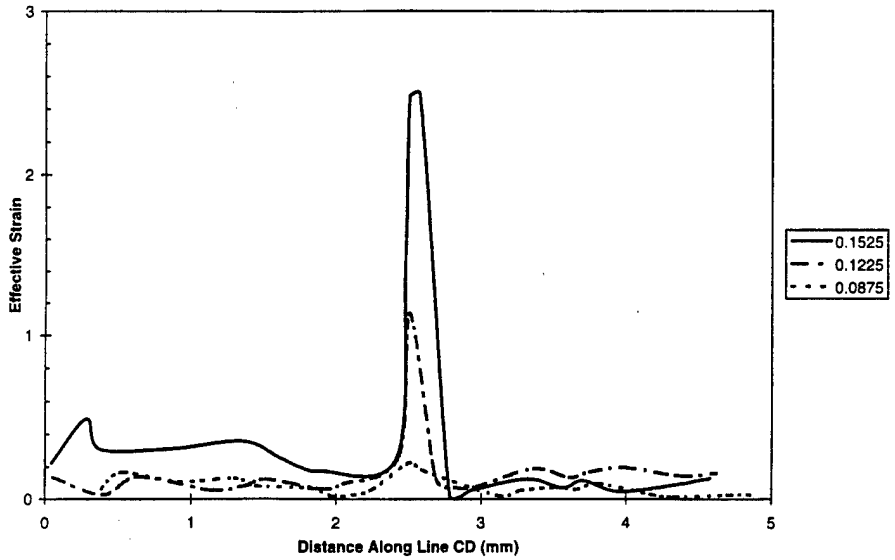

(a)

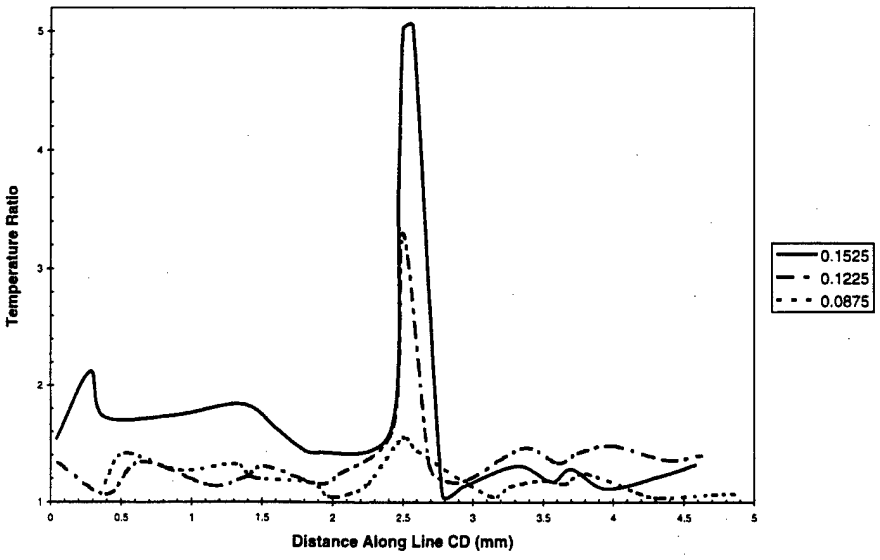

(b)

Fig. 8. Distribution, at three values of the average axial strain, of the effective plastic strain and nondimensional temperature on line CD perpendicular to AB.

occupied a place on line *CD*. It is clear that tungsten particles are intensely deformed, and the maximum temperature of any tungsten particle on line *CD* equals 1478 K. Of course, this value and the width, approximately 400 μm, of the severely deformed region as well as other results presented herein are mesh dependent. A much finer mesh could not be used with the available computational resources. Our experience with adaptively refined meshes (e.g. see Batra and Ko (1992)) indicates that present results are qualitatively correct and a finer mesh may alter slightly the nominal strain at which a shear band initiates. One way to obtain mesh independent results is to use a higher-order gradient theory (Batra and Hwang, 1994; Batra, 1987).

We have plotted in Fig. 9(a) and (b) the velocity of Fe–Ni–W particles for the same value of the average strain at which deformed meshes are plotted in Fig. 4(a) and (b). The velocity of tungsten particles is not shown to avoid cluttering the plots. It is clear that for the deformed mesh of Fig. 4(a), the deforming region is divided into three parts; the material near the top left corner lying above the shear band is moving vertically downward, that between the two localized regions of intense deformation and the right boundary is moving with essentially a uniform velocity in the −45° direction, and the third part between the −45° band and the bottom left corner is practically at rest. Thus in this case, there is a large dead zone formed. For the deformed mesh of Fig. 4(b), the deforming region is divided into two parts; the one above the band moves as a rigid body in the −45° direction and that below the band is virtually at rest. At the instant the deformed mesh in Fig. 4(c) is plotted, the body is divided into four regions; the one near the top left corner is moving vertically downwards with the applied velocity, that near the top right corner is moving with a uniform velocity in the −45° direction, the one enclosed

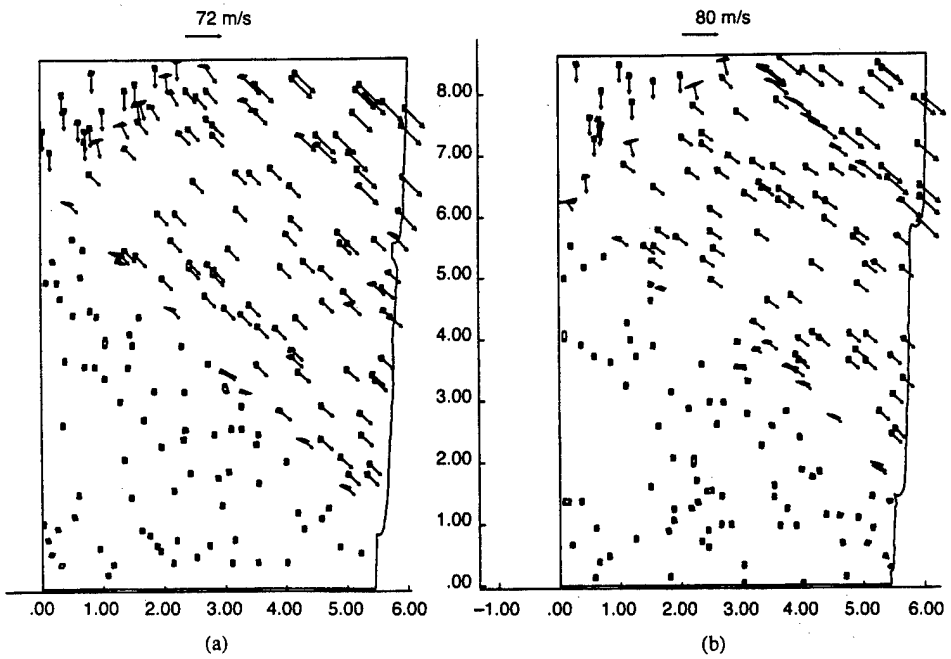

Fig. 9. Velocity distribution in Fe–Ni–W particles at an average axial strain of 0.1375 for the random distributions shown in Fig. 2(a) and (c).

by narrow regions of intense deformation on three sides with the fourth side traction free is also moving in the −45° direction but with a considerably lower speed than the region adjoining the top right corner. The large region bounded by a part of the left edge, bottom edge, a shear band and a part of the right edge constitutes the dead zone.

The effect of the volume percentage of Fe–Ni–W particles on the load versus average strain curve is exhibited in Figs 10(a) and (b). Initially, the load decreases monotonically with an increase in the volume percentage of Fe–Ni–W particles. However, for an average axial strain exceeding 0.10, the load required to deform the composite block with 0.1% Fe–Ni–W particles is less than that for 0.2% Fe–Ni–W particles. Similarly, the load for 4% Fe–Ni–W particles is less than that for 6% Fe–Ni–W particles. This is because the two distributions of Fe–Ni–W particles result in different deformation patterns. For the pure tungsten case (Fig. 10(c)), the load drops at a much higher value of the average strain than that for the case of only one randomly situated Fe–Ni–W particle. However, for two randomly located Fe–Ni–W particles in the lower one-fourth of the block, the load dropped at almost the same time as for pure tungsten. In this case three parallel shear bands, as shown in Figs 11(a) and (b), initiated first in the approximately 45° direction near the bottom right edge but eventually a dominant shear band (cf. Fig. 11(c)) passing through a point near the bottom right corner and inclined at nearly −45° formed. None of these bands passed through either one of the two Fe–Ni–W particles. This does not support Backmann and Finnegan's (1973) suggestion that shear bands initiate from defects, second phase particles or other impuritites in the body. For the block made of pure tungsten, the nonhomogeneity in the deformation occurs because of the interaction between incident waves and waves reflected from the boundaries; for other case waves scattered from Fe–Ni–W particles interact with other waves mentioned earlier. As is obvious from the deformed meshes of Fig. 4 and the random distributions of Fe–Ni–W particles shown in Fig. 3, a shear band does not initiate from every point where the effective plastic strain is expected to be higher than that at its neighboring points. One will speculate that a larger volume percentage of Fe–Ni–W particles will result in an earlier onset of the localization process; however, this can not be concluded from the load versus average strain curves except when there is only one Fe–Ni–W particle. For torsional deformations of a thin-walled tube with thickness varying sinusoidally in the axial direction, Batra *et al.* (1996) found that the average strain at the initiation of a shear band decreased monotonically with a decrease in the minimum thickness of the tube or an increase in the defect size; Chi (1990), Murphy (1990) and Deltort (1994) obtained similar results experimentally. Molinari and Clifton (1987) and Wright (1994) have investigated analytically the effect of the defect size on the localization of the deformation in a simple shearing problem. However, for the plane strain problem studied by Batra and Peng (1995), and for the present problem the load required to deform the tube did not decrease monotonically with an increase in the number of randomly distributed weak elements. One may argue that a larger number of Fe–Ni–W particles does not necessarily imply that the defect size has increased.

Figure 12 depicts the deformed mesh at an average axial strain of 0.135 when there is only one (0.01%) randomly located Fe–Ni–W particle; in this case two shear bands in the form of an X pass through the Fe–Ni–W particle. This deformation pattern resembles that observed by Batra and Liu (1989) during plane strain deformations of a steel block with only one weak element at the centroid but differs from the ones computed herein with two or more Fe–Ni–W particles (cf. Figs 4 and 11).

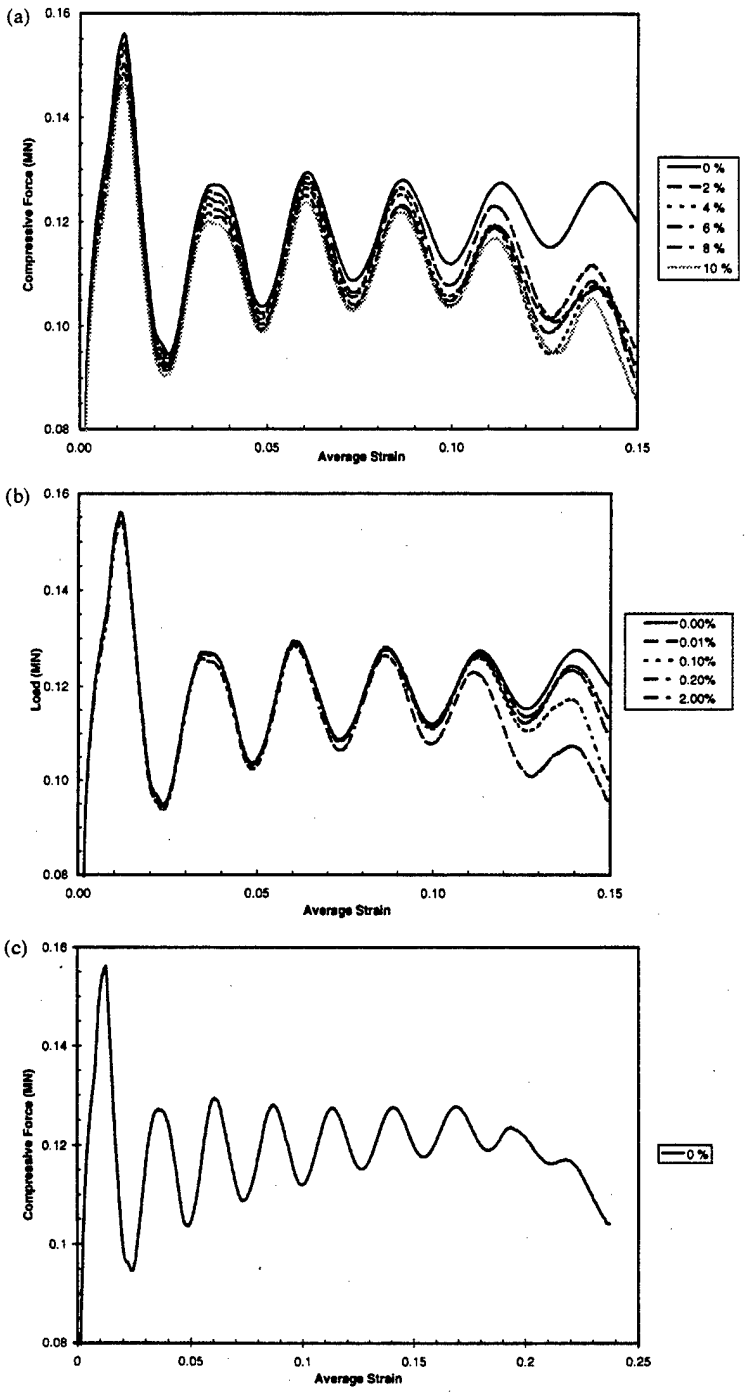

Fig. 10. Compressive load versus average axial strain curves for different volume percentages of Fe–Ni–W particles; in each case these particles are randomly distributed.

We also simulated axisymmetric deformations of a 5-cm long WHA cylinder of 1-cm radius and deformed by prescribing the axial component of velocity on the top and bottom faces. A plane passing through the axis of the cylinder was divided into 10^4 uniform rectangular elements with 100 elements each in the radial and axial directions. For upto 10% randomly distributed Fe–Ni–W elements on this cross-section and an average axial strain of 50% no shear bands were observed. However, when the exponent m in the thermal softening expression in eqn (1) was changed to 1.0, shear bands formed even in pure tungsten cylinders. This signifies that the thermal softening function plays a critical role especially during the axisymmetric deformations of the body. Walter (1992) has elucidated upon how different thermal softening functions influence the localization of deformation in simple shearing deformations of a thermoviscoplastic body.

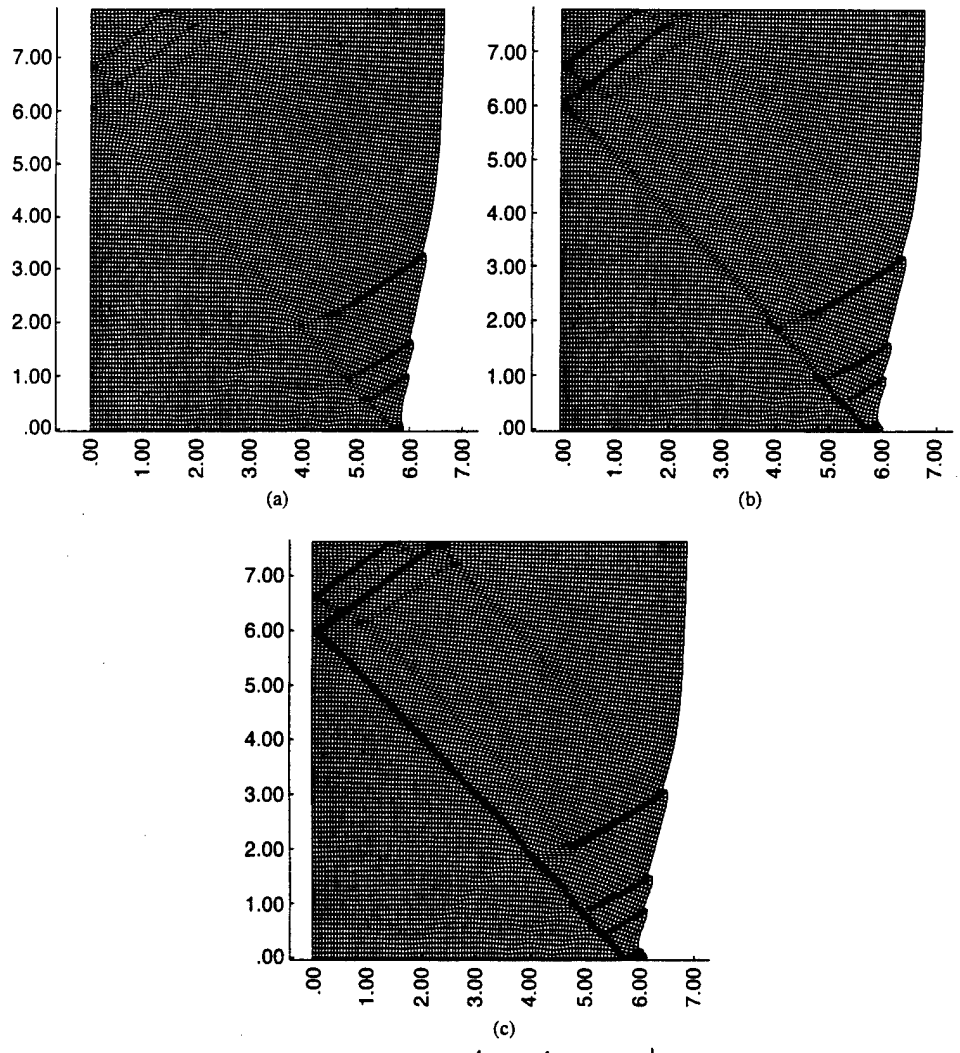

Fig. 11. Deformed meshes at average axial strains of 0.1875, 0.2125 and 0.2250 for the case of two randomly located Fe–Ni–W particles.

(a) (b) (c)

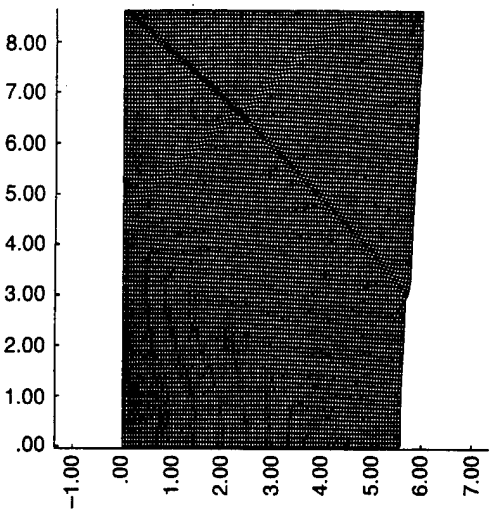

Fig. 12. The deformed mesh at an average axial strain of 0.1375 for one randomly located Fe–Ni–W particle.

IV. CONCLUSIONS

We have studied dynamic plane strain and axisymmetric deformations of a WHA with tungsten and iron–nickel–tungsten modeled as thermoviscoplastic materials. Except when the thermal softening effect is made arbitrarily large, no shear bands were observed in axisymmetric deformations. For values of material parameters determined from test findings of Zhou (1983), and for plane strain compression of a WHA block, different volume percentages of Fe–Ni–W particles resulted in essentially identical compressive load versus average axial strain curves for upto an average axial strain of 0.10; for average axial strains exceeding 0.10, the decrease in the load was not a monotonic function of the increase in the volume percentage of Fe–Ni–W particles. Also for a fixed percentage of Fe–Ni–W particles, no noticeable differences were observed in the load-average axial strain curves for seven different random distributions of 2, 4, 6, 8 and 10% Fe–Ni–W particles. However, in each case, the computed deformation patterns, the number of shear bands, and the sizes and shapes of the dead zones were different. Except for the case when there is only one Fe–Ni–W particle, it is hard to ascertain where a shear band will initiate first. For one random distribution of 2 Fe–Ni–W particles, three parallel shear bands, as evidenced by the deformed mesh, initiated first in the 45° but eventually one dominant band formed in the −45° direction; none of these bands passed through either one of the two Fe–Ni–W particles. In every case considered, more than one shear band as characterized by narrow regions of intense plastic deformation formed; the plastic strain distribution in these narrow regions is not uniform. Even though the effective stress at a material point within a shear band when plotted against the effective strain there drops rapidly, the time-rate of drop of the effective stress is low for sometime and picks up subsequently. Also, the compressive load required to deform the block does not drop catastrophically even when a shear band, as indicated by the severely deformed mesh, has fully developed.

Acknowledgements—This work was supported by the Army Research Office grant DAAH04-95-1-0042 and the National Science Foundation grant CMS9411383 to Virginia Polytechnic Institute and State University. The authors are grateful to J. Boyet Stevens, a graduate student at VPI, for his help with the determination of the values of material parameters.

REFERENCES

Armstrong, R., Batra, R. C., Meyers, M. A. and Wright, T. W. (Guest eds) (1994) Special issue on shear instabilities and viscoplasticity theories. *Mech. Mater.* **17**, 83–327.

Backmann, M. E. and Finnegan, S. A. (1973) The Propagation of Adiabatic Shear. In *Metallurgical Effects at High Strain Rates*, eds R. W. Rhode, B. M. Butcher, R. Holland and C. H. Karnes, pp. 531–543. Plenum Press, New York.

Bai, Y. and Dodd, V. (1992) Adiabatic shear localization, occurrence, theories, and applications, Pergamon Press.

Batra, R. C. (1987) The initiation and growth of, and the interaction among adiabatic shear bands in simple and dipolar materials. *Int. J. Plasticity* **3**, 75–89.

Batra, R. C. (1996) The Speed of Propagation of an Adiabatic Shear Band in Thermoviscoplastic Materials. *Proc. Third Asia-Pacific Symp. on Advances in Engineering Plasticity and its Applications*, eds T. Abe and T. Tsuta, pp. 105–110. Pergamon Press, Amsterdam, Oxford, New York, Tokyo.

Batra, R. C. and Hwang, J. (1994) Dynamic shear band development in dipolar thermoviscoplastic materials. *Comp. Mechs.* **12**, 354–369.

Batra, R. C. and Kim, C. H. (1991) Effect of thermal conductivity on the initiation, growth, and band width of adiabatic shear bands. *Int. J. Engng. Sci.* **29**, 949–960.

Batra, R. C. and Kim, C. H. (1992) Analysis of shear bands in twelve materials. *Int. J. Plasticity* **8**, 425–452.

Batra, R. C. and Ko, K. J. (1992) An adaptive mesh refinement technique for the analysis of shear bands in plane strain compression of a thermoviscoplastic block. *Comp. Mechs.* **10**, 369–379.

Batra, R. C. and Liu, D. S. (1989) Adiabatic shear banding in plane strain problems. *J. Appl. Mechs.* **56**, 527–534.

Batra, R. C. and Peng, Z. (1995) Development of shear bands in dynamic plane strain compression of depleted uranium and tungsten blocks. *Int. J. Impact Engng.* **16**, 375–395.

Batra, R. C. and Zbib, H. M. (1994) *Material Instabilities: Theory and Applications.* ASME Press, New York.

Batra, R. C. and Zhang, X. (1994) On the propagation of a shear band in a steel tube. *J. Engng. Materials and Tech.* **116**, 155–161.

Batra, R. C., Adulla, C. and Wright, T. W. (1996) Effect of defect shape and size on the initiation of adiabatic shear bands. *Acta Mechanica* **116**, 239–243.

Bell, J. F. (1968) *The Physics of Large Deformation of Crystalline Solids.* Springer-Verlag, New York.

Chi, Y. C. (1990) Measurement of the local strain and temperature during the formation of adiabatic shear bands in steel, Ph.D. thesis. Brown University.

Deltort, B. (1994) Experimental and numerical aspects of adiabatic shear in a 4340 steel. *J. de Physique, Colloque C8* **4**, 447–452.

Farren, W. S. and Taylor, G. I. (1925) The heat developed during plastic extrusion of metal. *Proc. R. Soc.* **A207**, 422.

Johnson, G. R. and Cook, W. H. (1983) *A Constitutive Model and Data for Metals Subjected to Large Strains, High Strain Rates and High Temperatures.* Proc. 7th Int. Symp. *Ballistics*, The Hague.

Klepaczko, J. R., Lipinski, P. and Molinari, A. (1987) *An Analysis of the Thermoplastic Catastrophic Shear in Some Metals, Proc. Impact Loading and Dynamic Behavior of Materials*, eds C. Y. Chiem, H. -D. Kunze and L. W. Meyer. Informationsgesellschaft, Verlag, Bremen.

Magness, L. S. and Farrand, T. (1990) Deformation behavior and its relationship to the penetration performance of high density KE penetrator materials. *Proc. Army Sci. Conf.* West Point, New York.

Marchand, A. and Duffy, J. (1988) An experimental study of the formation process of adiabatic shear bands in a structural steel. *J. Mech. Phys. Solids* **36**, 251–283.

Molinari, A. and Clifton, R. J. (1987) Analytical characterization of shear localization in thermoviscoplastic materials. *J. Appl. Mech.* **54**, 806–812.

Murphy, B. P. (1990) Shear band formation in a structural steel under a combined state of stress. M.S. Thesis, Brown University, Providence, RI, USA

Sulijoadikusumo, A. V. and Dillon, Jr, O. W. (1979) Temperature distribution for steady axisymmetric extrusion with an application to Ti-6Al-4V, Part 1. *J. Thermal Stresses* **2**, 97–112.

Truesdell, C. A. and Noll, W. (1965) *The Nonlinear Field Theories of Mechanics, Handbuch der Physik*, ed. S Flügge, Springer, Berlin.

Walter, J. W. (1992) Numerical experiments on adiabatic shear band formation in one dimension. *Int. J. Plasticity* **8**, 657–694.

Whirley, R. G., Englemann, B. E. and Hallquist, J. P. (1992) DYNA2D, *A Nonlinear, Explicit, Two-Dimensional Finite Element Code for Solid Mechanics.* User manual, Lawrence Livermore National Laboratory Report, UCRL-MA-110630.

Wright, T. W. and Walter, J. W. (1987) On stress collapse in adiabatic shear bands. *J. Mech. Phys. Solids* **35**, 701–716.

Wright, T. W. (1994) Toward a defect invariant basis for susceptibility to adiabatic shear bands. *Mech. Materials* **17**, 215–222.

Zbib, H. M., Shawki, T. and Batra, R. C. (eds) (1992) *Material Instabilities*, special issue of *Applied Mechanics Reviews*, **45**(3).

Zhou, M. (1993) Dynamic shear localization in a tungsten heavy alloy and ductile rupture in a spheroidized 1045 steel. Doctoral dissertation, Brown University, Providence, RI, USA.

CAS 1849 [DJH 31/1/98]

Pergamon

PII: S0045-7949(97)00103-X

Computers & Structures Vol. 00, No. 0, pp. 1–13, 1998
© 1998 Elsevier Science Ltd. All rights reserved
Printed in Great Britain
0045-7949/98 $19.00 + 0.00

PENETRATION/PERFORATION OF ALUMINUM, STEEL AND TUNGSTEN PLATES BY CERAMIC RODS

N. V. NECHITAILO and **R. C. BATRA**†

Department of Engineering Science and Mechanics, Virginia Polytechnic Institute and State University, Blacksburg, VA 24061-0219, U.S.A.

(*Received* 19 *December* 1996; *accepted* 29 *August* 1997)

Abstract—The axisymmetric penetration/perforation of rigidly clamped circular metallic plates by fast moving AD-85 ceramic cylindrical rods has been studied. The ceramic is modeled as an elastic–plastic material with pressure cut-off and the target material is modeled as linearly strain-hardening elastic–plastic material with a material point failing when the effective plastic strain there attains a prescribed value; failed elements are removed from the analysis. For low impact speeds, the ceramic rod fails causing a shallow crater in the metallic target. However, at impact speeds in the range of 1 to 5 km/s, the partially destroyed ceramic rods perforate through the metallic targets. The effect of material parameters of the metallic plates on the efficiency of penetration has been studied. © 1998 Elsevier Science Ltd. All rights reserved

Key words—kinetic energy penetrators, metallic targets, finite element method, multiple impacts, elastic–plastic material, material failure

INTRODUCTION

The dynamic response of engineering ceramics to impulsive loading has been studied during the last thirty years. The commercial AD-85 alumina has been shown to exhibit the following features: the loss of shear strength during shock loading, reduction of the spall strength with an increase in the intensity of the compression shock, multiple microcracking and viscous flow associated with local melting [1, 2]. The residual spall strength after passage of the compressive wave is shown to be a function of the initial impact speed [3]. Furthermore, strength of ceramics is quite high under shock loading [4]. The Hugoniot elastic limit of ceramics (~6–10 GPa) is very high compared with that of high-strength metallic alloys (~1–3 GPa) [1, 5]. Good fracture toughness and high Hugoniot elastic limit of ceramics have been used to protect metallic and composite structures from damage during a penetration event by bonding ceramic layers on their outside surfaces. The high strength and inertia of ceramic layers result in high impact stresses leading to fracture or severe plastic deformations of steel projectiles.

Although there is considerable theoretical and experimental work on the use of ceramics as targets, we have not found any published theoretical or experimental study on using ceramics as penetrators. It could be due to the fact that ceramic projectiles are perceived to be too weak and crushable to penetrate hard steel targets. However, because of their high Hugoniot elastic limit and compressive strength, it seems that they should be able to impart high kinetic energy to the metallic target and deform it severely. An objective of this study is to demonstrate that indeed ceramic rods can perforate even tungsten targets at moderate impact speeds. We use simple material models, assume that an element fails when the effective plastic strain in it reaches a critical value and delete failed elements from the analysis. This approach to deal with failed elements was developed and popularized by Stetcher and Johnson [10] and is currently in wide use, for example, see Refs [11, 12].

FORMULATION OF THE PROBLEM

We use the Lagrangian/referential description of motion to analyze the axisymmetric deformations of a rigidly clamped circular metallic plate impacted at normal incidence by a fast moving cylindrical ceramic rod. Equations expressing the balance of mass and linear momentum may be found in Truesdell and Noll [6]. Even though such impact problems involve high pressures and possibly high temperatures, especially at points adjoining the target–penetrator interface, the dependence of material properties upon the temperature is neglected and a mechanical problem is analyzed herein.

The target material (aluminum, steel or tungsten) is modeled as elastic–plastic with linear strain-hardening. An element is assumed to fail when the effective plastic strain in it reaches a preassigned value

†Author to whom all correspondence should be addressed.

CAS 1849 [DJH 31/1/98]

and failed elements are removed from the analysis. The ceramic material is modeled as elastic–plastic with a pressure cut-off. The experimental work of Rosenberg [8] on AD-85 ceramic suggests that the dynamic yield stress, σ_{dyn}, depends affinely upon the hydrostatic pressure p, but is independent of the effective strain-rate; thus

$$\sigma_{dyn} = \sigma_{st} + pA, \tag{1}$$

where σ_{st} equals the yield stress in a uniaxial simple compression test, p is taken to be positive in compression and

$$A = 3[(1-2\nu)\sigma_H - (1-\nu)\sigma_{st}]/[(1+\nu)\sigma_H]. \tag{2}$$

Here ν is Poisson's ratio and σ_H is the Hugoniot elastic limit. We note that values of σ_H and σ_{st}, and hence of A, are different in compression and tension; these are given by:

$$\sigma_H^t = \frac{(1-\nu)}{(1-2\nu)}\sigma_{dyn}, \tag{3}$$

$$\sigma_H^c = \sigma_H^t(\sigma_{st}^c/\sigma_{st}^t), \tag{4}$$

where the superscripts t and c signify tensile and compressive loading, respectively. Following Rajendran [7], we use the modified Mie–Gruneisen equation of state to model the volumetric behavior of the AD-85 ceramic under impact loading. Neglecting thermal effects and assuming that the ratio of the bulk to shear moduli degraded due to the evolution of porosity and/or microcracks is the same as that of the intact material, we obtain:

$$p = \alpha R_k[2 - \Gamma + (-3 + 2.5\Gamma)e^{\epsilon_v} + (1 - 2\Gamma)e^{2\epsilon_v} + 0.5\Gamma^{3\epsilon_v}],$$

where

$$R_k = 2(1-f)(1-2\nu)/[2(1-2\nu) + f(1+\nu)]. \tag{6}$$

Here, α is the effective bulk modulus and takes account of the degradation of the material properties of the ceramic due to its initial porosity, f is the void fraction or porosity of the material, Γ is the Mie–Gruniesen parameter, R_k the Mackenzie correction factor and $\epsilon_v = \ln(v/v_0)$ is the volumetric strain, where v and v_0 are the present and specific volumes. During elastic unloading from a plastic state, we assume that the bulk modulus stays constant and its magnitude equals α, the slope of the equation of state at $\epsilon_v = 0$. A ceramic material point is assumed to fail when the hydrostatic pressure there is tensile and its magnitude exceeds the spall strength of the material.

At the target–penetrator interface, we impose the condition of impenetrability and assume that the dynamic coefficient of friction, μ, is given by

$$\mu = \mu_k + (\mu_s - \mu_k)e^{-\gamma v_{rel}}, \tag{7}$$

where μ_s and μ_k are the static and kinetic coefficients of friction respectively, γ is a transition coefficient and v_{rel} is the relative speed between the two sliding surfaces. Frictional forces are not anticipated to play any significant role in this problem because of the quick failure of ceramic elements. All bounding surfaces of the penetrator except the target–penetrator interface are traction free. The target plate is assumed to be rigidly clamped at its periphery and other surfaces except the target–penetrator interface are taken to be traction free.

Initially the target particles are at rest and are unstressed and the penetrator particles are moving in the axial direction with a uniform speed V_0. The penetrator strikes the target at normal incidence and the deformations of both the penetrator and the target are assumed to be axisymmetric.

RESULTS AND DISCUSSION

The afore-stated problem is highly nonlinear due to both geometric and material nonlinearities and is difficult to solve analytically. We seek its approximate solution by the finite element method and use the explicit general purpose code DYNA2D [9]. It employs four-noded quadrilateral elements, an explicit time integration scheme, a one-point quadrature rule to evaluate various integrals and an hour-glass control to eliminate spurious modes. We used the standard DYNA2D hour-glass stabilization method with the hour-glass viscosity coefficient = 0.10, bulk viscosity type 1, quadratic bulk viscosity = 1.5 and linear shock viscosity coefficient = 0.06. The time step equalled 20% of that computed in the code from the Courant condition (i.e. the time required for an elastic wave to travel through the smallest element in the mesh). As is evident from the finite element discretization of the penetrator and the target shown in Fig. 1, both the penetrator and the target are divided into uniform rectangular elements. The deforming regions are rezoned after a few elements have failed and/or other elements have been severely distorted; the rezoning option in DYNA2D is employed for this purpose. The 'automatic contact' feature in DYNA2D was used to identify surfaces of potential contact after each time step. The scale factor for automatic slideline penalty parameter was assigned the value 1.2 and $\mu_k = 0.06$, $\mu_s = 0.78$ and $\gamma = 0.0055$.

In order to compute the numerical results presented below, the following values are assigned to various material parameters; the values of geometric parameters are indicated in Fig. 1. AD-85 Ceramic [7,8]: Poisson's ratio, $\nu = 0.22$; Mie Gruniesen parameter, $\Gamma = 1.0$; initial mass density, $\rho = 3420\ kg/m^3$; shear modulus, $\mu = 108$ GPa; static tensile yield stress, $\sigma_{st}^t = 0.155$ GPa; static compressive yield stress, $\sigma_{st}^c = 1.93$ GPa; spall strength, $\sigma_{sp} = 0.4$ GPa; effective bulk modulus, $\alpha = 186$ GPa; Hugoniot elastic limit in compression, $\sigma_H^c = 6$ GPa.

CAS 1849 [DJH 31/1/98]

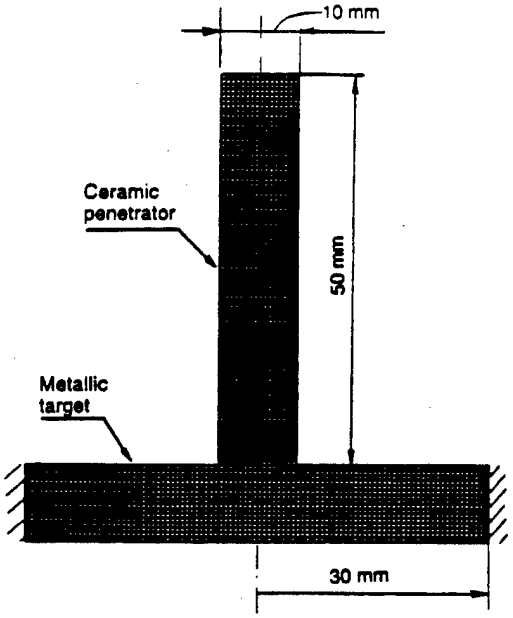

Fig. 1. Schematic sketch of the problem studied and finite element discretization of the penetrator and the target.

For the target materials, the material properties are listed in Table 1.

Upon impact, compressive stress waves are generated in both the penetrator rod and the target plate. For subsonic impacts these waves propagate at the sound speed of the materials and at the shock speed for impacts at hypervelocity. These are followed by slower moving shear waves. The two waves propagate until they interact with a free surface from which a compressive wave is reflected as a tensile wave. For proper duration and amplitude of the tensile pulse, material failure by a variety of mechanisms can occur, see Ref. [5]. Since the penetrator is slender, the interaction between incident and reflected waves in it results in rather complicated and interesting failure patterns. Depending on the target material, geometry and impact conditions, a projectile can lose its nose, or it can break or buckle or different regions can get eroded away. We discuss these below for three different target materials.

Target plate made of 6061-T6 aluminum

Figure 2 depicts the deformed configurations of the ceramic rod and the aluminum plate at three instants of time and for impact speeds of 0.5 and 3 km/s; the failure patterns in the ceramic rod and the aluminum plate in the two cases are quite different. At an impact speed of 0.5 km/s, the central portion of the ceramic rod near the impact surface fails 2 μs after impact making it a hollow cylinder of nonuniform thickness. The hollow cylinder cuts a concave cavity in the plate. At 22 μs, the failed region has propagated along the axis of the penetrator to the rear free end and the central portion of the target plate has been bent. The deformation patterns in the penetrator and the target plate remain essentially unchanged until 41.6 μs and the plate is not perforated in this case. However, for an impact speed of 3 km/s, ceramic material near the impacted end of the penetrator is severely deformed and the penetrator nose becomes conical at 1.6 μs after impact. In addition, there is a crater formed in the aluminum plate. Because of the erosion of the penetrator material, there is a gap between the ceramic rod and the aluminum target; the intact portion of the rod impacts the plate again causing severe damage and essentially a hole in the plate at 8.4 μs. Because of the kinetic energy imparted to the plate, the hole diameter near the back surface of the plate becomes larger with time and the penetrator moves through it.

For impact speeds of 2, 4 and 5 km/s, the sequences of deformations of the penetrator and the target are essentially similar to those observed at an impact speed of 3 km/s. For a 5 km/s impact speed, the flat impacted end of the penetrator is deformed into a conical one at 1.19 μs which because of the failure/erosion of the material becomes flat again at 2.39 μs and impacts the target surface at a subsequent time. At 4.39 μs, there is a large crater formed in the aluminum plate and a significant portion of the ceramic material in the interior of the penetrator has failed. There is a hole formed in the plate at 6 μs and the penetrator passes through it subsequently. Because of the kinetic energy imparted to the plate, the hole diameter continues to grow.

A major difference between the impact of an aluminum plate by a fast moving metallic rod and a ceramic rod is that in the former case, the penetrator nose is generally deformed into a mushroom, the target–penetrator interface moves into the target and multiple impacts do not occur. However, for the ceramic penetrator, a significant portion of the material near the impacted end is

Table 1. Material properties of the target materials

Material parameter	6061-T6 aluminum	4340 steel	D17-tungsten
Young's modulus, E (GPa)	73.3	200.00	350.00
Poisson's ratio, ν	0.28	0.29	0.28
Yield stress, σ_0 (MPa)	298.00	970.00	1550.00
Tangent modulus, E_T (GPa)	0.38	0.47	1.23
Effective plastic strain at failure	0.85	0.77	1.75
Mass density (kg/m^3)	2700.00	7850.00	17000.00

CAS 1849 [DJH 31/1/98]

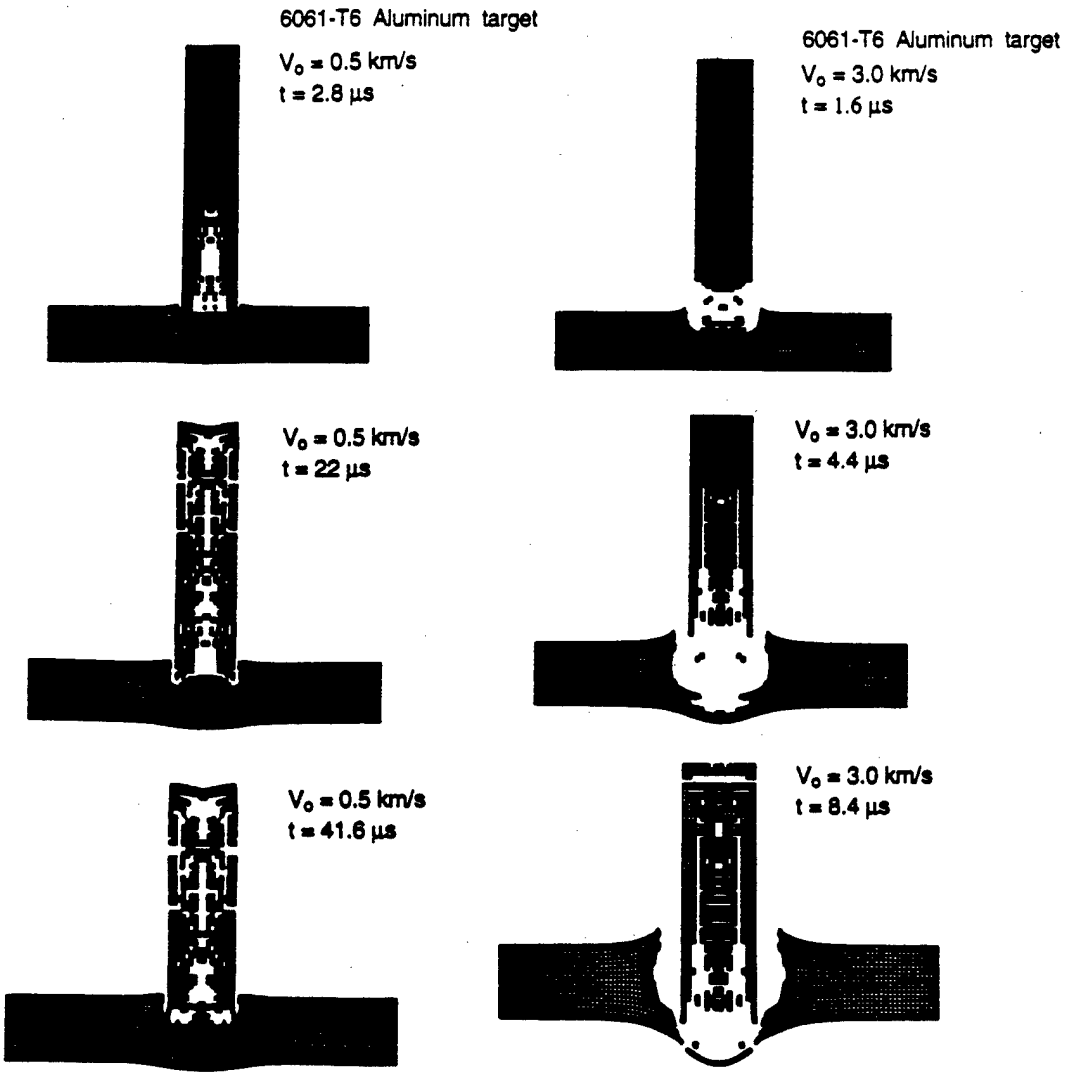

Fig. 2. Deformed configurations of the ceramic penetrator and the aluminum target plate at three instants of time for impact speeds of 0.5 and 3 km/s.

severely deformed and multiple impacts between the moving rod and the target transfer momentum to the deforming crater surface in the target. In both cases, deformations of the penetrator and the target depend strongly upon the impact speed. For a ceramic rod moving at 12 km/s just prior to impact, the complete perforation of the aluminum plate occurred in 2.5 μs and the penetrator nose experienced very little failure. When the target density was artificially increased to 10 times its normal value, we observed multiple impacts at an impact speed of 4 km/s, a parabolic crater during a late stage of penetration and almost complete erosion of the rod. The shape of the crater depends strongly upon the failure strain presumed for the target material. For small values of the failure strain, a smooth cylindrical crater is formed, but for high values of the failure strain, the crater is hemispherical with rough surfaces.

The evolution of the crater depth for different impact speeds is depicted in Fig. 3. These plots indicate that there is no perforation of the aluminum plate at an impact speed of 0.5 km/s and the perforation times for impact speeds of 3, 4, 5 and 6 km/s are considerably smaller than those for an impact speed of 1 km/s. The perforation time does not decrease monotonically as the impact speed is increased from 1 to 6 km/s. This could be due to the differences in the failure of the penetrator near the impacted end, the number of multiple impacts and the shape of the crater formed.

We have deleted failed elements irrespective of their locations. Thus, the kinetic energy associated with these failed elements is removed from the analysis and the space occupied by them just prior to failure is replaced by vacuum. In experiments the failed material may not disappear instantaneously. Thus, some of the computed shapes of the target

CAS 1849 [DJH 31/1/98]

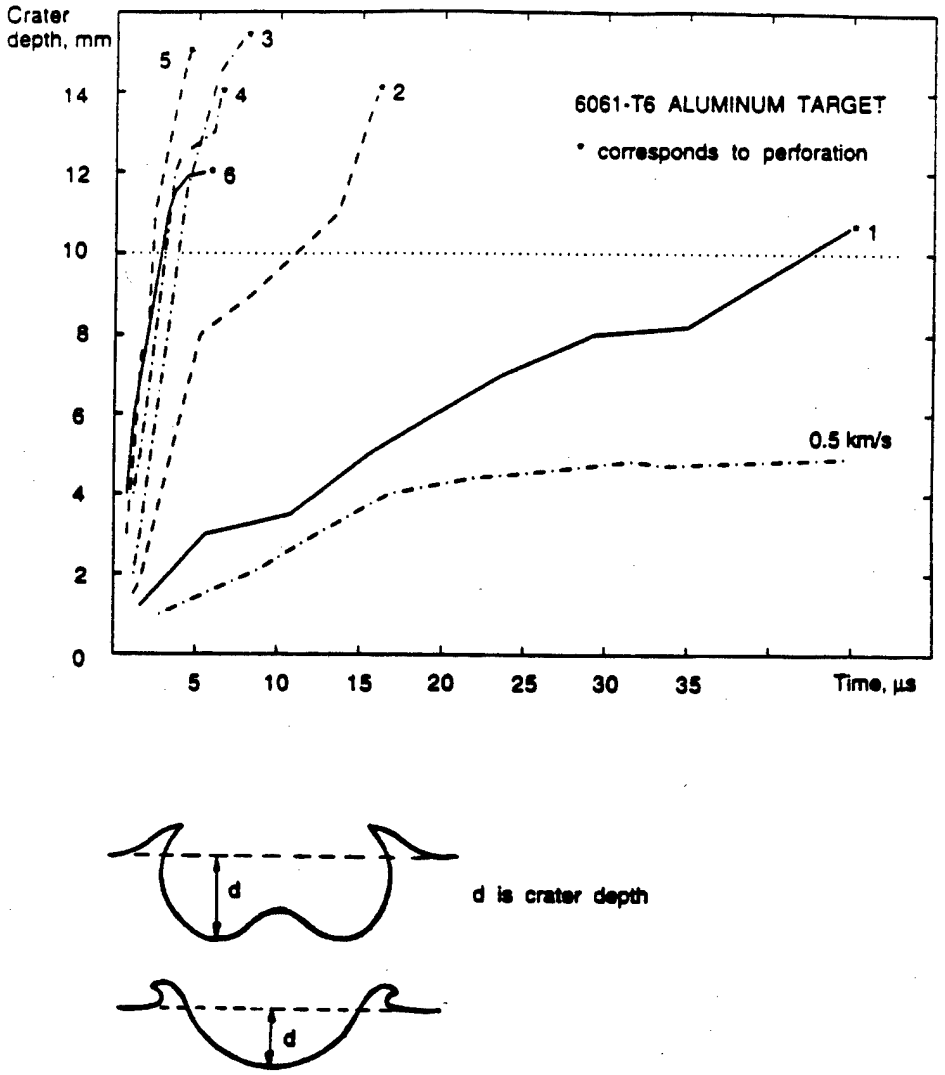

Fig. 3. Time history of the evolution of the crater depths in the aluminum plate struck at normal incidence by a ceramic rod at different impact speeds. The dotted horizontal line corresponds to the initial thickness of the plate. The crater depth for two different crater shapes is also defined in the figure.

and the penetrator may not match well with those observed in experiments when such tests are indeed performed. The results presented herein lead one to conclude that high kinetic energy ceramic rods can perforate metallic targets.

Target plate made of 4340 steel

For an impact speed of 0.5 km/s, the deformation patterns are similar to that for an aluminum target described above. Whereas initially the inner portion of the ceramic rod close to the axis of symmetry failed as was the case for an aluminum plate, subsequently the portion of the penetrator near the target–penetrator interface buckled because of the high resistance to penetration offered by the strong and dense steel plate. The failure of the rod material was due to the spall zone created at the axis of symmetry by tensile waves generated by the reflection of compressive waves from the free lateral surface of the rod. The rod material near the target–penetrator interface also expanded by sliding along the interface and buckled. The spall zone propagated to the upper part of the rod and its failure due to buckling also continued. Even though the plate bent, there was no noticeable crater formed.

The transition from axisymmetric buckling failure mode to mushrooming failure mode was observed for impact speeds of approximately 1 km/s. This deformation mode in which both the target and the penetrator material near the target–penetrator interface expand is less damaging for the penetrator, but more damaging for the target.

At the impact speed of 2 km/s, as shown in Fig. 4, the sequence of events is totally different from that at the impact speed of 0.5 km/s. Initially, the ceramic near the outer surface of the rod and close to the impacted end fails, making the penetrator nose somewhat pointed. There is a small crater formed

CAS 1849 [DJH 31/1/98]

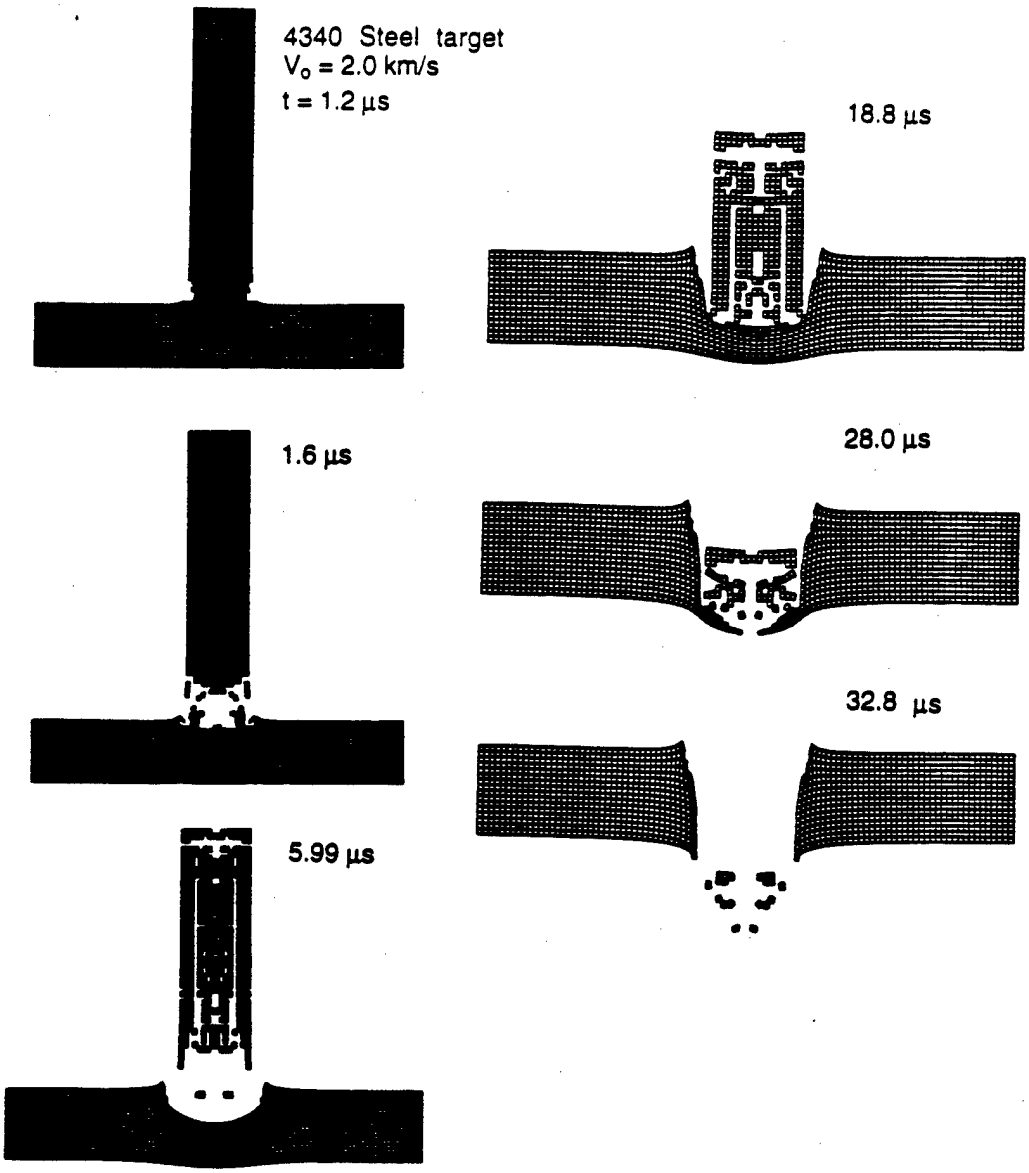

Fig. 4. Deformed configurations of the ceramic penetrator and the steel plate at different instants of time for an impact speed of 2 km/s.

in the steel plate at 1.6 μs and the ceramic material near the penetrator nose has been eroded giving rise to a gap between the penetrator and the target. Multiple impacts occur between the rod and the plate, the crater continues to enlarge, the plate is eventually perforated and essentially all of the penetrator is destroyed. The cylindrical surface of the crater is smooth even though the assumed value of the failure strain is relatively large.

For higher impact speeds, an impact flash is generated at the instant of impact, high-intensity stress waves propagate into the rod and the target and cratering of the plate surface and penetration of the rod commence immediately. Since, on initial impact, the peak pressure at the interface far exceeds the material strength of the rod and target, the penetrator front suffers hydrodynamic-like erosion, while the remainder of the rod enters the cavity undeformed. The crater deepens and its bottom expands due to the pressure exerted by the fluid-like expanding flow of the eroding rod nose. Intense shearing stresses are developed in the target material adjoining the target–penetrator interface. Plate failure occurs by one or more mechanisms described by Zukas[5].

At higher impact speeds the crater formed in the steel plate prior to complete perforation is hemi-toroidal rather than hemispherical and the penetrator nose shape becomes conical with a pointed nose and the cone angle of 45° immediately after impact. This change in the geometry of the rod makes the penetration process more efficient. For example, at

CAS 1849 [DJH 31/1/98]

an impact speed of 3 km/s, the penetration depth increases from 0.8 mm at $t = 1.6\ \mu s$ to 6.4 mm at $t = 5.59\ \mu s$. A significant part of the rod is eroded away and its nose shape changes from conical to a concave cutter. Multiple impacts increase both the depth and the diameter of the crater which transforms from a hemi-toroidal shape to a bubble-type. The number of multiple impacts and the shape and length of the residual penetrator vary with the impact speed. Higher the impact speed, greater the length of the residual penetrator after completion of the perforation process. For impact speeds of 5 and 6 km/s typical patterns of penetrator-target interaction were observed to be as follows: sharpening of the penetrator nose to conical with the remainder of the penetrator virtually undamaged, breaking away of the conical portion leading to a flat nosed solid rod, secondary impact leading to erosion of the rod nose material near its axis of symmetry thus resulting in a cutter nose, multiple impacts damaging the rod, the crater shape changing from hemi-toroidal to parabolic and to bubble-type cavity.

Target plate made of a D17 tungsten alloy

Figure 5 depicts deformed configurations of the ceramic penetrator and the tungsten target plate at different times for impact speeds of 3, 3.5 and 4 km/s. Whereas the tungsten plate is not perforated at an impact speed of 3 km/s, complete perforation occurs at the other two speeds and the shape of the hole formed depends noticeably upon the impact speed. For impact speed of 3 km/s, the central part of the penetrator head experiences maximum shear deformations and rapid failure of the front part of the rod creates a new flat surface at $t = 2.5\ \mu s$. Reflected tensile waves from the free lateral surface cause failure at inner points of the rod. Multiple impacts between the rod and the plate transfer momentum and energy to the target. At $t = 11.2\ \mu s$, the tungsten at the crater surface behaves as a compressible fluid. The crater is nearly hemispherical and both maximum shear stresses and plastic strains occur at points on the crater surface. Subsequent impacts between the rod and the crater surface transform the hemispherical shape of the crater into a cylindrical one and the depth of the final crater formed exceeds the thickness of the plate. The crater and hence the hole formed is parabolic at impact speeds of 3 and 3.5 km/s, a cylindrical hole is formed at impact speeds of 4 km/s and higher. Also significant bulging out and distortions of the penetrator material occur and the hole diameter is much larger than the diameter of the ceramic rod. For an impact speed of 4 km/s, the crater depth just prior to perforation exceeds twice the initial thickness of the plate.

Deformed configurations of the ceramic rod and the tungsten plate for an impact speed of 5 km/s are shown in Fig. 6 wherein contours of effective plastic strain in the two bodies at $t = 1.6\ \mu s$ are also plotted. Significant compressive plastic strains occur in the penetrator near the penetrator–target interface. The embedding followed by mushrooming and failure of the rod nose creates plastic flow and a hemispherical cratering of the target. The immersed nose experiences strong compression and unloading waves reflected from the free lateral surfaces cause erosion of the penetrator material resulting in a shape with cutting outer edges. Intensive plastic flow at the crater surface expands downwards and creates a large hemispherical cavity. Secondary impacts cause the fluid-like plastically deforming tungsten material to flow along the crater surface. At $t = 14\ \mu s$, the bottom part of the plate is intensively thinning, stretching and bending due to inertial effects. At an impact speed of 6 km/s, the penetration and perforation mechanisms are essentially similar to those for an impact speed of 5 km/s, but more damage is caused to the tungsten plate. All of the ceramic rod is consumed at an impact speed of 6 km/s. However, the length of the ceramic rod that survives increases with an increase in the impact speed.

We have plotted in Fig. 7, the evolution of the crater depth for steel and tungsten plates struck at normal incidence by ceramic rods at different speeds. The minimum impact speed at which complete perforation of the plate occurs in the two cases is quite different as expected because of the differences in the densities and material properties of the two materials. In each case, the time required to perforate the plate decreases monotonically with an increase in the speed of the rod.

For comparison, we have also studied the penetration/perforation of a tungsten rod, identical in shape to the ceramic rod, into a tungsten plate. Figure 8 depicts the deformed configurations of the rod and the plate at different times for impact speeds of 0.5, 3 and 5 km/s. For an impact speed of 0.5 km/s, the tungsten rod undergoes significant mushrooming and lateral expansion, but no perforation occurs. At $V_0 = 2$ km/s, the tungsten rod survives mushrooming, embedding into the target and perforates a wide hole whose diameter equals nearly twice that of the rod. When the impact speed equals 3 km/s, the penetration process is similar to that found for the ceramic rod moving at 5 km/s. However, the length of the residual tungsten rod is much greater than that of the residual ceramic rod and the residual tungsten rod undergoes very little damage except near the front end. In addition, multiple impacts do not occur for a tungsten rod impacting a tungsten plate. At impact speeds of 5–6 km/s the time required for ceramic rods to perforate through tungsten plates is slightly less than that for geometrically identical tungsten rods. Thus, the penetration–perforation capability of a ceramic rod into a tungsten plate approaches that of a tungsten rod.

CAS 1849 [DJH 31/1/98]

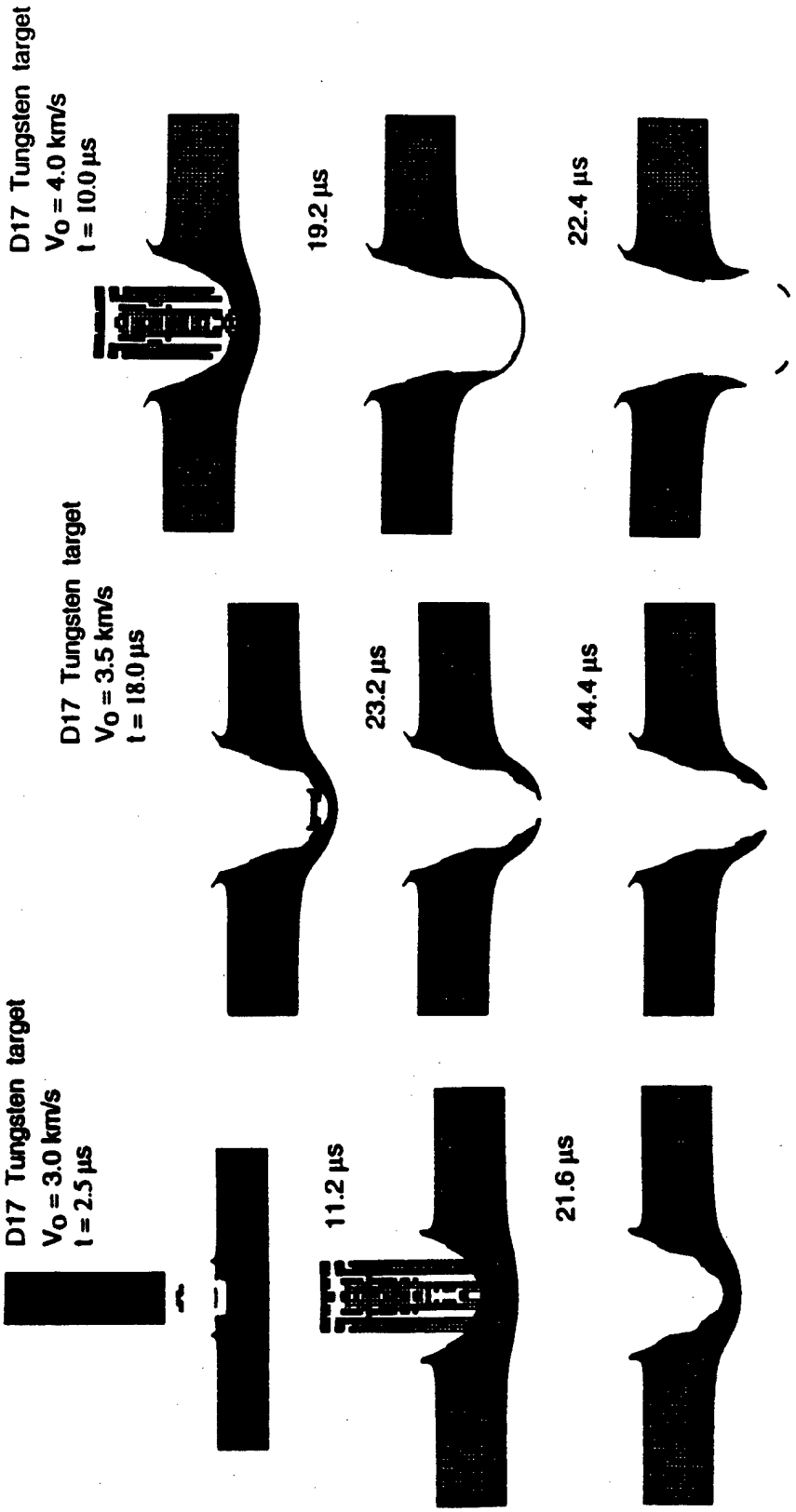

Fig. 5. Deformed configurations of the ceramic penetrator and the tungsten plate at different times and at impact speeds of 3, 3.5 and 4 km/s.

CAS 1849 [DJH 31/1/98]

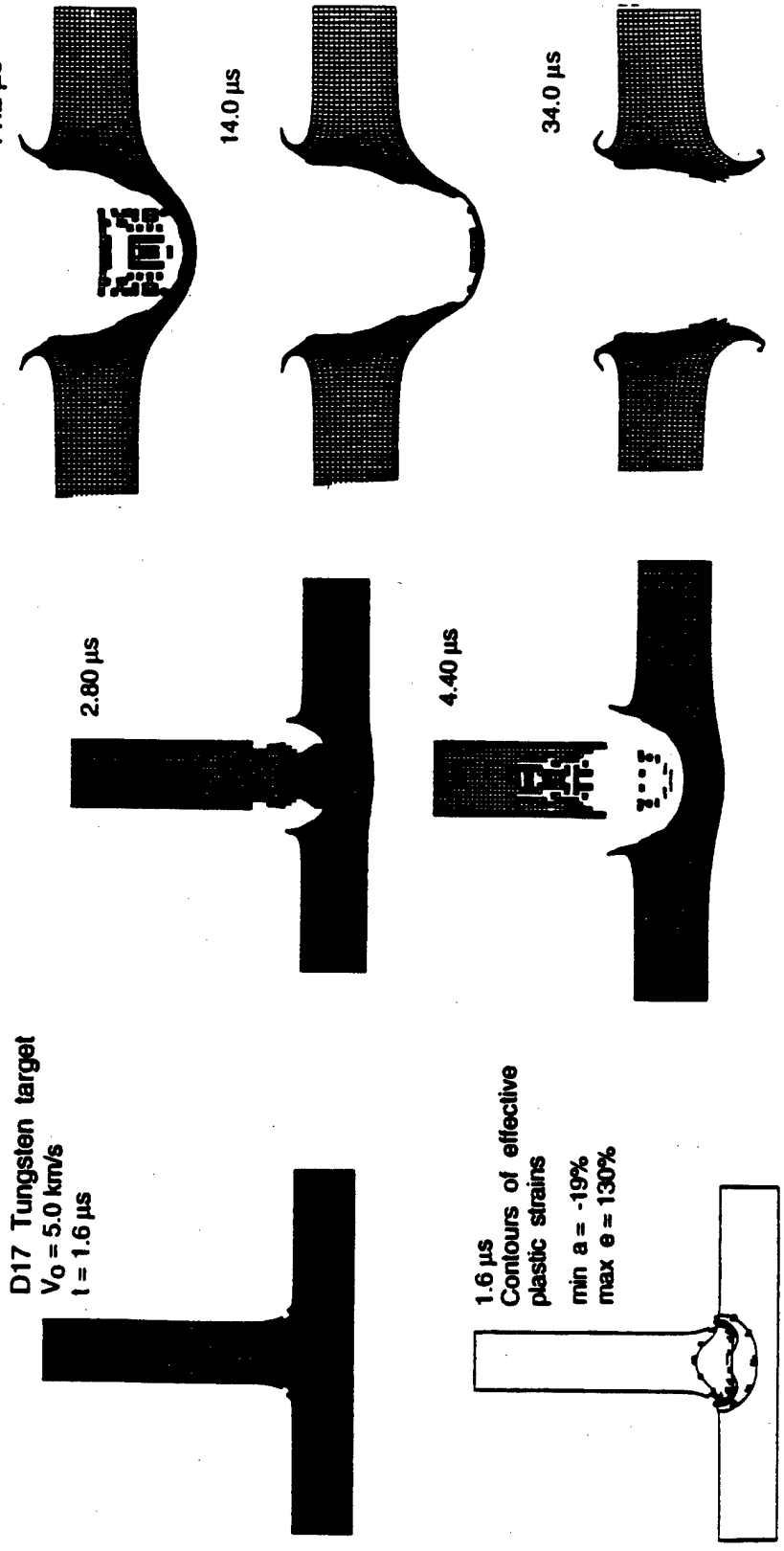

Fig. 6. Deformed configurations of the ceramic penetrator and the tungsten plate at different times and at an impact speed of 5 km/s.

CAS 1849 [DJH 31/1/98]

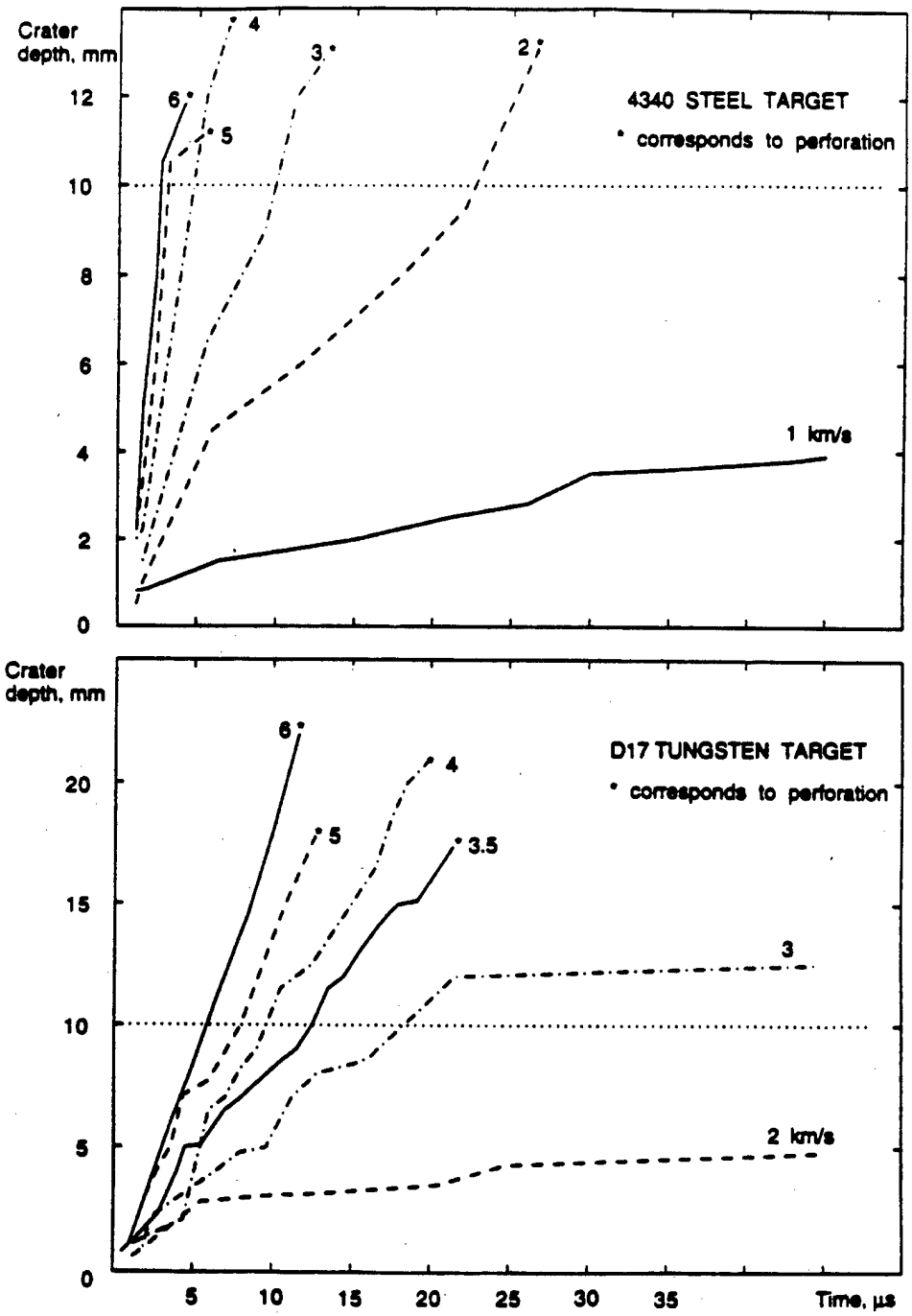

Fig. 7. Time histories of the evolution of crater depths in the 4340 steel and D17 tungsten plates struck at normal incidence by a ceramic rod at different impact speeds. The dotted line corresponds to the initial thickness of the plate.

For the problem being studied, the penetrator and the target support conditions are fixed. Thus, the crater depth and the residual penetrator speed when the target is perforated depends upon the mass density, yield strength, work-hardening and failure strain of the target material. As expected, higher mass density, yield strength and failure strain for the tungsten material result in lower values of the crater depth. Our numerical experiments with 'artificial' aluminum targets described above indicate that the mass density and the failure strain influence significantly the crater's shape and depth. Rosenberg and Dekel [12, 13] have also shown through numerical experiments that the failure strain affects noticeably the penetration depth and at high values of the penetrator length/penetrator

CAS 1849 [DJH 31/1/98]

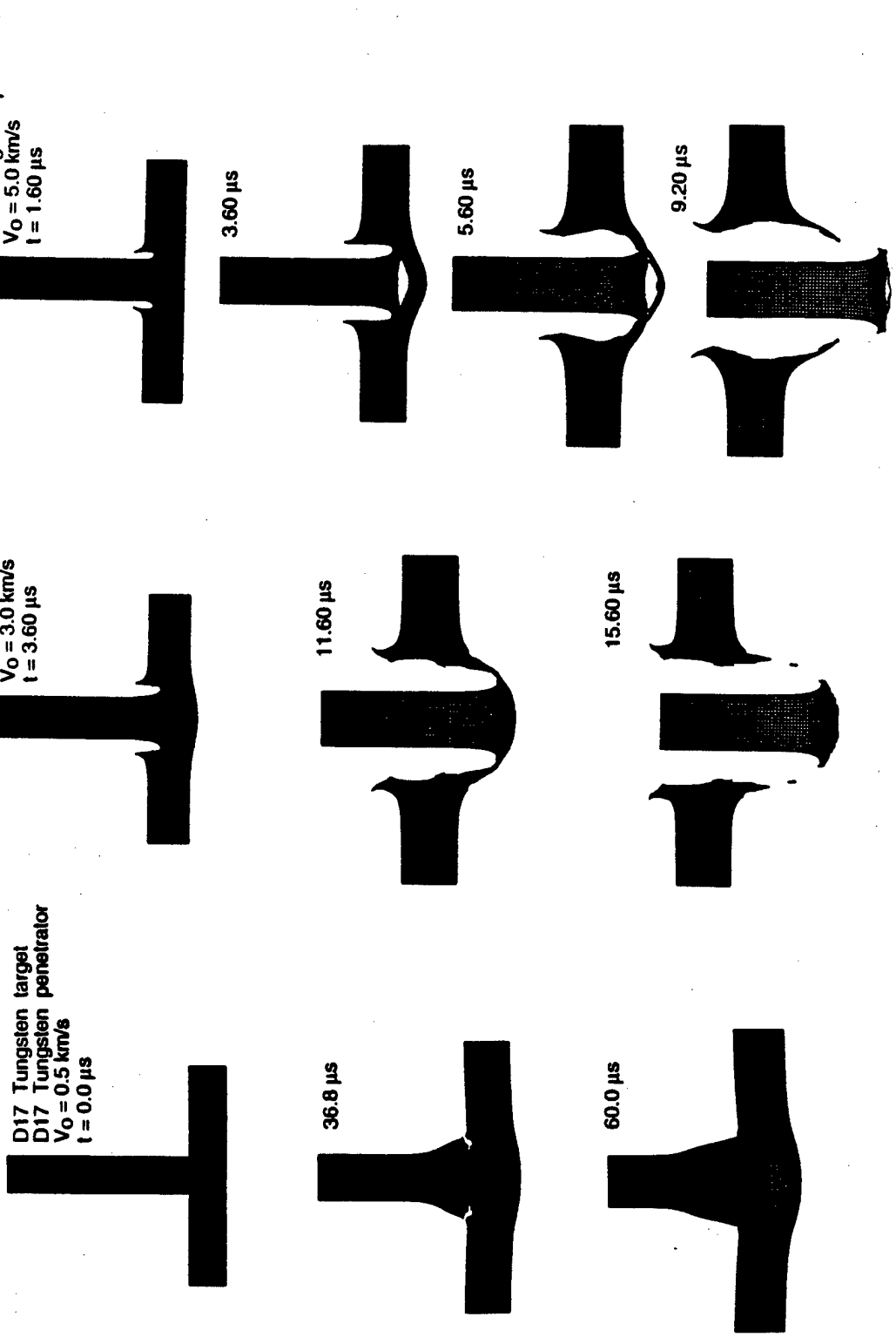

Fig. 8. Deformed configurations of the tungsten penetrator into a tungsten plate at different times for impact speeds of 0.5, 3 and 5 km/s.

CAS 1849 [DJH 31/1/98]

diameter a low-strength projectile can be more efficient than a high-strength one. This suggests that a ceramic rod should be able to perforate a hard target as is confirmed by our simulations. We note that Littlefield *et al.* [14] used the eroding element concept to simulate the penetration of tungsten rods into steel targets and found a good agreement between computed penetration depths and those observed experimentally. Bless *et al.* [15, 16] have conducted penetration tests with ceramic rods, but the impact speeds used were too low to result in any significant crater formation. This is consistent with our numerical simulations. Apparently, they found it difficult to conduct reverse ballistic tests (a moving target hits a stationary rod) at high impact speeds.

Analytical penetration models include the one-dimensional models of Alekseevskii [17] and Tate [18] and the cavity expansion model of Forrestal *et al.* [19] Rosenberg and Dekel have shown that the one-dimensional models are not valid for simulating two-dimensional tests. Furthermore, these one-dimensional models assume a semi-infinite target and we have analyzed targets of finite thickness. Ravid *et al.* [20] and Batra and Chen [21], among others, have developed models to analyze the normal perforation of metallic plates by essentially rigid projectiles. The unknown parameters presumed in the kinematically admissible flow field are found by a minimization technique. Because of the rather rapid failure of the ceramic rod, these models are not applicable to the present problem.

CONCLUSIONS

We have studied the axisymmetric penetration of the ceramic rod into aluminum, steel and tungsten plates. The ceramic is modeled as an elastic–plastic material with different properties in compression and tension and a material point is assumed to fail when the hydrostatic pressure there is tensile and exceeds the spall strength of the material. The plate material is modeled as an isotropic elastic/plastic with linear strain hardening and a material point is assumed to fail when the effective plastic strain there attains a critical value. Failed elements are deleted from further analysis.

Plates made of aluminum, steel and tungsten were found to be perforated by the ceramic rod. However, deformations of the ceramic penetrator and the shape of the hole formed depended strongly upon the impact speed. For aluminum plates, the hole was found to be smooth cylindrical for small values of the failure strain and rough hemispherical for large values of the failure strain. For the steel and tungsten plates, the nose shape was initially deformed from flat to conical and the conical part failed giving rise to a smaller flat-nosed rod. Subsequently, the rod material near its axis of symmetry and the front end failed resulting in a cutter edge. Multiple impacts between the rod and the crater formed in the plate eventually perforated the plate. The residual length of the rod after perforation was found to be more at higher impact speeds.

Acknowledgements—This work was supported by the U.S. Army Research Office grant DAAH04-95-1-0042 to the Virginia Polytechnic Institute and State University. We are indebted to Mr Forrest Flocker, a graduate student at the University of Missouri-Rolla and Miss Sharon Smale, an undergraduate student at VPI&SU, for help with DYNA2D and some of the computations. Miss Smale was supported by a grant from the NSF to VPI&SU.

REFERENCES

1. Brandon, D. G., Yeshurun, Y., Rosenberg, Z. and Ozeri, Y., Micromechanisms of impact failure in engineering ceramics. *Macro- and Micro-Mechanics of High Velocity Deformation and Fracture*. IUTAM Symposium on MMMHVDF, Tokyo, Japan, 1987, pp. 127–133.
2. Anderson, C. E. Jr, O'Donoghue, P. E., Lankford, J. and Walker, J. D. Numerical simulation of SHPB experiments for the dynamic compressive strength and failure of ceramics. *International Journal of Fracture*, 1992, **55**, 193–208.
3. Rosenberg, Z., Yaziv, D. and Bless, S. J., The shear strength of shock-loaded alumina as determined with embedded longitudinal and transverse manganin gauges. Report UDR-TR-86-123, University of Dayton Research Institute—Impact Physics Laboratory, 1989.
4. Bless, S. J., Impact behavior of ceramics. In *Dynamic Constitutive/Failure Models*, ed. A. M. Rajendran and T. Nicholas. Report AFWAL-TR-4229, Wright-Patterson Air Force Base, OH, 1988.
5. Zukas, J. A., *High velocity impact dynamics*. Wiley, New York, 1990.
6. Truesdell, C. A. and Noll, W. The nonlinear field theories of mechanics. *Handbuch der Physik*, Vol. III/3, ed. S. Flügge. Springer, Berlin, 1965.
7. Rajendran, A. M. Modeling the impact behavior of AD85 ceramic under multiaxial loading. *International Journal of Impact Engineering*, 1994, **15**, 749–768.
8. Rosenberg, Z. Dynamic uniaxial stress experiments on alumina with in-material manganin gauges. *Journal of Applied Physics*, 1985, **57**, 5087.
9. Whirley, R. G., Englemann, B. E. and Hallquist, J. O. *DYNA2D, A Nonlinear, Explicit Two-dimensional Finite Element Code for Solid Mechanics. User Manual*. Lawrence Livermore National Laboratory Report, UCRL-MA-110630, 1992.
10. Stetcher, F. P. and Johnson, G. R. Lagrangian computations for projectile penetration into thick plates. In *Computers in Engineering*, Vol. 2, ed. W. A. Grover, ASME, pp. 292–299, 1984.
11. Kimsey, K. D. and Zukas, J. A. Contact surface erosion for hypervelocity problems, BRL-MR-3495, 1986.
12. Rosenberg, Z. and Dekel, E. A computational study of the relation between material properties of long rod penetrators and their ballistic performance.
13. Rosenberg, Z. and Dekel, E. A computational study of the influence of projectile strength on the performance of long-rod penetrators. *International Journal of Impact Engineering*, 1996, **6**, 671–677.
14. Littlefield, D. L., Anderson, C. E. Jr, Partom, Y. and Bless, S. J. The penetration of steel targets finite in

CAS 1849 [DJH 31/1/98]

radial extent. *International Journal of Impact Engineering*, 1997, **19**, 49–62.

15. Brar, N. S., Bless, S. J. and Rosenberg, Z. Brittle failure of ceramic rods under dynamic compression. *Journal de Physique C*, 1988, **3**, 607–612.
16. Bless, S. J., Brar, N. S. and Rosenberg, Z., Failure of ceramic and glass rods under dynamic compression. In *Shock Compression of Condensed Matter*, ed. S. C. Schmidt, J. N. Johnson and L. W. Davison, Elsevier, Oxford, pp. 939–942, 1990.
17. Alekseevskii, V. P. Penetration of a rod into target at high velocity. *Combustion, Explosions and Shock Waves*, 1966, **2**, 63.
18. Tate, A. Further results in the theory of long rod penetration. *Journal of the Mechanics and Physics of Solids*, 1969, **17**, 141.
19. Forrestal, M. J., Okajima, K. and Luk, V. K. Penetration of 6061-T651 aluminum targets with rigid long rods. *Journal of Applied Mechanics*, 1988, **55**, 755–760.
20. Ravid, M., Bodner, S. R. and Holcman, I. Analysis of very high speed impact. *International Journal of Engineering Science*, 1987, **25**, 473–482.
21. Batra, R. C. and Chen, X. An approximate analysis of steady state axisymmetric deformations of viscoplastic targets. *International Journal of Engineering Science*, 1990, **28**, 1347–1358.